

Modeling of streamer discharges near dielectrics

PROEFSCHRIFT

ter verkrijging van de graad van doctor aan de Technische Universiteit Eindhoven, op gezag van de rector magnificus, prof.dr.ir. F.P.T. Baaijens, voor een commissie aangewezen door het College voor Promoties, in het openbaar te verdedigen op donderdag 1 september 2016 om 16.00 uur

door

Anna Alexandrovna Dubinova

geboren te Frunze, Kyrgyzstan

Dit proefschrift is goedgekeurd door de promotoren en de samenstelling van de promotiecommissie is als volgt:

voorzitter: prof.dr.ir. H.J.M. Swagten
1^e promotor: prof.dr. U.M. Ebert
copromotor: dr.ir. S. Nijdam
leden: prof.dr. C. M. Franck (Eidgenössische Technische Hochschule Zürich)
prof.dr. O. Scholten (Rijksuniversiteit Groningen)
prof.dr. F. Toschi
adviseur: dr. S. Pancheshnyi (ABB Corporate Research Center, Baden-Dättwil)

Het onderzoek of ontwerp dat in dit proefschrift wordt beschreven is uitgevoerd in overeenstemming met de TU/e Gedragscode Wetenschapsbeoefening

Copyright © 2016 A. Dubinova

This research was carried out in the National Research Institute for Mathematics and Computer Science (CWI) and it was supported by the Dutch Technology Foundation STW, which is part of the Netherlands Organisation for Scientific Research (NWO). The research was partly funded by the Ministry of Economic Affairs (project number 12119) and it was partly funded by ABB Corporate Research.



A catalogue record is available from the Eindhoven University of Technology Library
ISBN: 978-90-386-4128-7

Cover image: “Oak Fractured by Lightning” (allegory on the artist’s wife death) by Maxim Vorobiev, 1842, taken from Wikimedia Commons, the free media repository.

To my father

Contents

1	Introduction	1
1.1	Streamer discharges	1
1.1.1	Streamers in industry	1
1.1.2	Streamers in nature	1
1.2	“Creeping sparks” project	2
1.3	Introduction into the physics of streamers	3
1.3.1	Townsend scaling with gas density	3
1.3.2	Positive and negative streamers	4
1.3.3	Sources of electrons for positive streamers	5
1.4	Influence of dielectrics	7
1.4.1	Field effects of a dielectric	7
1.4.2	A dielectric as a source and sink of free electrons	7
1.5	Questions addressed in the thesis	8
2	Electron emission from a dielectric surface	11
2.1	Photoemission from the dielectric rod	12
2.1.1	The physical phenomenon	12
2.1.2	Numerical implementation	13
2.1.3	The uncertainty about the photoemission yield	14
2.2	Secondary electron emission due to ion bombardment	15
2.2.1	The physical phenomenon	15
2.2.2	Numerical implementation	15
2.3	Electron emission in an external electric field (field emission)	16
2.3.1	The physical phenomenon	16
2.3.2	Numerical implementation	17
3	Numerical modeling of streamers	19
3.1	Challenges in streamer modeling	20
3.2	Overview of streamer models	20
3.2.1	Particle models	20
3.2.2	Fluid models	21
3.2.3	Hybrid models	22

3.2.4	Tree models	22
3.3	The challenge of solving the Poisson equation in streamer simulations	22
3.4	Ghost Fluid Method (GFM)	23
3.4.1	GFM for the Poisson equation with a discontinuous dielectric permittivity on a cylindrical grid	24
3.4.2	Level set representation	26
3.4.3	A remark about electrons reaching a dielectric	27
3.4.4	Example: 1D problem with a dielectric interface	27
3.5	Implementation of the flux of photons onto a dielectric rod	28
4	Pulsed positive discharges in air at moderate pressures near a dielectric rod	31
4.1	Introduction	32
4.1.1	Problem setting	32
4.1.2	Our cylindrically symmetric set-up	32
4.1.3	Positive discharges and the role of photoionization and photoemission	34
4.1.4	Order of the paper	36
4.2	Modeling and simulations	36
4.2.1	Physical model	36
4.2.2	Fluid model	36
4.2.3	Electric field	38
4.2.4	Photoionization and photoemission	39
4.2.5	Initial conditions	40
4.3	Experiments	41
4.3.1	Discharge morphology	42
4.3.2	The role of pressure	44
4.4	Comparison of simulations with experiments	46
4.5	Discussion	50
4.5.1	Field enhancement in the absence of a discharge: geometrical effect	55
4.5.2	Field enhancement in the presence of a discharge	56
4.6	Positive streamer interaction with a dielectric rod in pure nitrogen	58
4.7	Conclusions	59
5	Attraction of a positive cylindrically symmetric air streamer to a dielectric rod with an embedded anode	63
5.1	Introduction	64
5.2	New setup	64
5.3	Results	67
5.3.1	Velocity of streamers	67
5.3.2	Influence of photoemission	68
5.3.3	Influence of the diameter of the dielectric rod	69
5.4	Conclusions	72

6	Prediction of lightning inception by large ice particles and extensive air showers	73
6.1	Introduction	74
6.2	Structure of the approach	75
6.3	Requirements on hydrometeor size and shape	75
6.4	Requirement on the density of free electrons	77
6.5	Discharge inception and propagation from a hydrometeor	77
6.6	Occurrence rate of required electron density	81
6.7	Probability of coincidence of large hydrometeor and extensive air shower inside the thundercloud field	82
6.8	Summary and discussion	83
7	Streamer discharge inception in a sub-breakdown electric field from a solid boundary in air	85
7.1	Analysis of discharge inception based on the Meek number	86
7.1.1	Introduction of the Meek criterion for negative streamers in bulk gas	86
7.1.2	Density description of avalanche to streamer transition	87
7.1.3	Illustration of the multiple avalanche streamer inception in the density perspective	88
7.1.4	Time restriction for the charge growth at the tip of the dielectric	90
7.1.5	Electron avalanches developing along different field lines	92
7.2	Role of photoionization in discharge inception	93
7.2.1	Time-dependent simulations in constant field approximation	93
7.3	Influence of the dielectric permittivity on streamer inception	96
7.4	Conclusions	96
8	Propagation of a positive streamer toward a dielectric tip in pure nitrogen and in air under voltage pulses with sub-nanosecond rise time	99
8.1	Introduction	100
8.2	Modeling	100
8.3	Results	101
8.4	Conclusions	101
9	An alternative approach to calculating photoionization and photoemission	105
9.1	Introduction	106
9.2	Description of the approach	106
9.2.1	Analytical reformulation	106
9.2.2	Remarks on numerical implementation	107
9.3	Appearance of $G(\mathbf{r}, \lambda; g)$ in discharge physics	109
9.3.1	Example 1: Photoionization in $N_2:O_2$ gas mixtures	109
9.3.2	Example 2: Photon flux onto a surface	109

9.4	Comparison with other models for calculating photoionization in air and pure nitrogen	110
9.4.1	Analytical solution for a point photon source	110
9.4.2	Approximation by Bourdon et al (2007) for a point photon source	110
9.4.3	Approximation by Luque et al (2007) for a point photon source	111
9.4.4	Numerical implementation of our approach in air	111
9.4.5	Numerical implementation of our approach in high purity nitrogen (with 1 ppm oxygen).	114
9.5	A photon flux from a point source onto a flat surface	115
9.6	Conclusions	116
10	Conclusions and outlook	119
10.1	Conclusions	119
10.2	Outlook	122
	Acknowledgements	139
	Curriculum Vitae	141
	Summary	143

Chapter 1

Introduction

1.1 Streamer discharges

Streamer discharges are cold transient electric discharges with pronounced space charge. They appear as ionized filaments with a thin curved space charge layer at their head and they can penetrate into non-ionized gaseous, liquid or solid media due to the high electric field produced by the space charge layer at their tip.

Streamers typically propagate with 0.1-10 mm/ns. On such a short time scale heavy ions can usually be considered immobile and heating is negligible, because the system is far from thermodynamic equilibrium and the energy is carried only by electrons and primary excitations. The dynamics of streamers is dominated by acceleration of electrons in the electric field and by their frequent collisions with neutral molecules.

1.1.1 Streamers in industry

Streamers are powerful at activating chemical reactions without causing much heating. Due to these unique properties streamers find their applications, for example, in cleaning of polluted gas and water [1–3], where they break up the polluting molecules, or in healing of wounds without burning the skin [4, 5]. Streamers in air naturally create ozone, and ozone is widely used for cleaning swimming pools and medical equipment [6]. In aerospace engineering, streamer discharges are used to control gas flows around airplane wings [7]. The advantages of non-thermal plasma actuators based on streamer discharges include low average power consumption, the absence of moving parts and their compactness. Non-equilibrium plasma produced by streamers offers the possibility of lean ignition and combustion in engines and burners [8].

1.1.2 Streamers in nature

Streamers are the first self-propagating phase of a lightning discharge which can turn into a hot conductive filament, or the leader. When the leader connects to the ground, a very high current flows through the ionized channel to equalize the potential difference

between the thundercloud and the ground. This is called a “return stroke” and this is the most luminous part of lightning seen by naked eye and known to everyone.

Surprisingly, the most fundamental questions of lightning still remain unanswered. Even the origin of lightning is still under debate. One of the most common hypotheses states that lightning inception is associated with ice particles present in thunderclouds. Ice particles are dielectric bodies, which behave in an electric field, generally speaking, very much like insulating materials used in high voltage applications. This problem of lightning inception was one of the motivations for our research of streamers discharges near dielectrics.

In nature, streamers can be encountered in the form of sprites¹, large-scale electrical discharges above thunderclouds where the air pressure is much lower than on the ground. Sprites usually appear as huge clusters of streamers of red color that span tens of kilometers. They are much larger than streamers at STP due to scaling with pressure (discussed in detail in section 1.3.1). Sprites were predicted theoretically in the 1920s by the nobel laureate C.T.R. Wilson, but first recorded photographically in 1989. Later, other types of discharges above thunderclouds were documented, which are now collectively called transient luminous events (TLEs).

1.2 “Creeping sparks” project

Streamers can transform into hot plasma channels, in other words sparks, after they reach the other electrode, for example at high electric currents, higher pressures or due to long pulse durations. After an ionization channel connects two electrodes with large potential difference and large capacitance, the electric current increases enormously, which leads to destructive heating of everything around it. Sparks often occur in high voltage applications, where they are to be avoided, or in nature (e.g., lightning).

Conductive elements in high voltage devices are often covered with dielectric materials to prevent detrimental sparks. The problem is that streamers sometimes prefer to creep over the surface of dielectrics instead of moving straight between two parts under a high voltage, as can be seen in figure 1.1. This eventually causes a surface flashover and damages the insulation. Surface streamers are thus considered precursors to surface (or “creeping”) sparks. This is a well-known fact, but the physical mechanisms responsible for that are yet poorly understood. For this reason, the optimization of high voltage devices relies nowadays largely on empirical knowledge, rather than on physical understanding. The project “Creeping sparks” was initiated to gain insight into the physics of surface discharges by studying streamers near dielectrics.

¹named after a character in *Midsummer Night’s Dream* by W. Shakespeare [9]

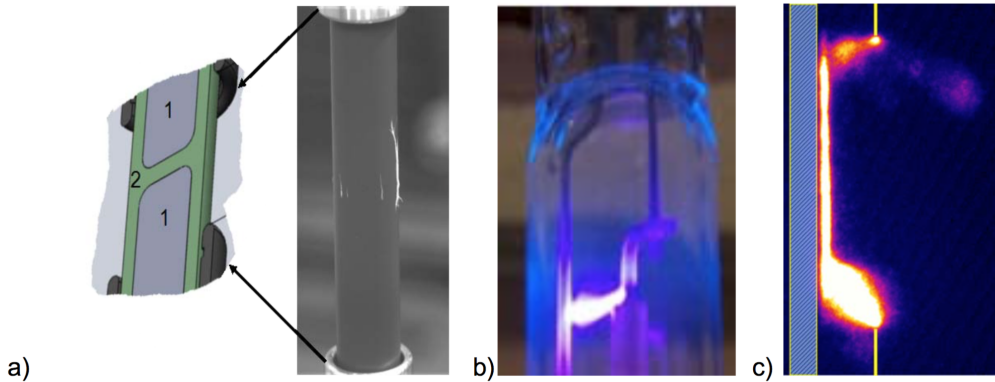


Figure 1.1: a) A discharge creeps over the surface of an insulating epoxy rod (2) in which electrodes (1) are embedded; the discharge develops on the insulator surface without contact with electrodes (ABB Corporate Research). B) A surface discharge develops in the outer tube of an HID-lamp, leading to efficiency loss, blackening of the glass, corrosion of the lamp parts and, finally, to the failure of the lamp (Philips Lighting). C) A discharge creeps over a dielectric though the two electrodes are placed 6 mm away from it [10]. Electrodes and dielectric are indicated and the photograph is presented in false color.

1.3 Introduction into the physics of streamers

When an electric field is applied to a gas, free electrons present in the gas accelerate and collide with the molecules of the gas. When the electric field is so high that electrons can gain sufficient energy between collisions, they can free electrons from those molecules. The liberated electrons will also accelerate in that electric field, producing even more electrons. Such a process is called an electron avalanche. An avalanche (or multiple avalanches [11]) can culminate in a streamer discharge when the number of electrons reaches about 10^8 - 10^9 in atmospheric air (the Meek criterion [12]). Those electrons are able to create their own electric field by forming a thin space charge layer around the head of the discharge (see figure 1.2), which will further support the electron multiplication. The continuous electron multiplication maintains the high electric field ahead of the space charge layer. In this way streamers self-propagate, and they can penetrate areas where the electric field is much below the breakdown field.

1.3.1 Townsend scaling with gas density

The first to start introducing similarity laws was J.S. Townsend [13] and since then they have been extensively studied [14]. They can be summarized as follows: streamer ionization fronts of the same gas composition at different pressures are essentially physically similar, assuming the same voltage and rescaled distances.

The dynamics of streamer discharge fronts is dominated by the collisions of elec-

trons with neutral molecules, and three-body processes can usually be neglected within the ionization front. Therefore, the electron mean free path ℓ is the basic length scale of streamers. It scales inversely proportional with the gas density or with the gas pressure, according to the ideal gas law:

$$\ell = \frac{1}{4\sigma n} = \frac{kT}{4\sigma p}, \quad (1.1)$$

where σ is average collisional cross section, n is the gas density, k is the Boltzmann constant, T is the gas temperature, and p is the pressure.

The similarity laws state that streamers are similar if their electrons gain the same energy in the electric field: $eE\ell$, where $E = |\mathbf{E}|$, e is the elementary charge. Therefore, the characteristic electric field is proportional to the gas density $E \sim \ell \sim n$.

Since the electron mobility μ_e is inversely proportional to pressure, the electron drift velocity is independent of pressure. This also means that the characteristic time scale of streamers τ is inversely proportional to pressure.

Scaling of the electron density n_e can be derived from the scaling of the dielectric relaxation time $\tau_d = \epsilon_0/(en_e\mu_e)$, where ϵ_0 is the permittivity of vacuum. Hence, the electron density scales with pressure as $n_e \sim n^2$ [15]. As the drift velocities are independent of pressure in similar streamers, the electric current densities scale with electron densities: $j \sim n$.

Scaling with pressure is an approximation for example due to multi-body processes in the streamer channel, or due to photoemission and photoionization. The shape and surface of electrodes and dielectrics cannot be, generally speaking, rescaled with pressure. However, if their role is not dominant, the approximation is reasonable.

1.3.2 Positive and negative streamers

Depending on the mechanism of their propagation streamers can be split into two categories: positive and negative. Negative streamers propagate with the electron drift or, in other words, against the electric field by accelerating their own electrons. The space charge in the head of negative streamers has a surplus of electrons. Positive streamers move with the electric field and thus against the electron drift by sucking in new incoming electrons in their head, which is positively charged. This is illustrated in figure 1.2.

The crucial difference between these mechanisms of propagation is that positive streamers need a constant supply of electrons in front of their head, whereas negative streamers need only initial seed electrons.

Positive streamers are typically easier to initiate in real life, because electrons coming to their head help the streamer to retain their shape and to maintain a high electric field at their head. Electrons accelerating in the electric field of negative streamers move outwards, which leads to the divergence of the streamer and therefore to the decrease of the electric field of the streamer [16, 17]. To counteract that effect, higher voltages are typically required for negative streamers. On the other hand, it is easier to simu-

late negative streamers as they do not need the constant (nonlocal) source of electrons, which is often costly to simulate.

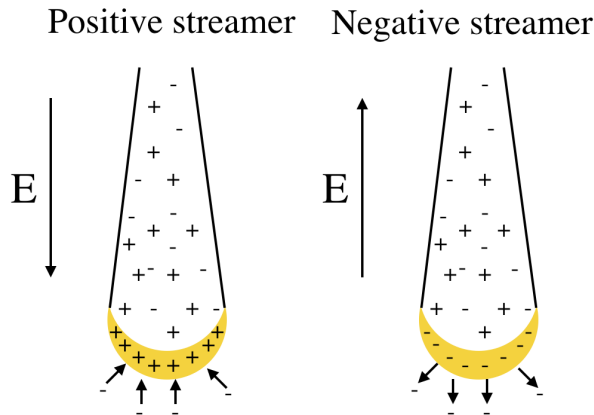


Figure 1.2: Artistic impression of a positive and a negative streamer with a thin space charge layer at their tip (shown in yellow).

1.3.3 Sources of electrons for positive streamers

In air and other $N_2:O_2$ mixtures, we identify the following sources of free electrons for positive streamers:

- Background ionization (natural ionization and remaining ionization in repetitive discharges)
- Photoionization
- Photon induced secondary electron emission (or photoemission)
- Secondary electron emission from a dielectric or conductive surface due to electron or ion bombardment
- Field induced electron emission

The main source of natural background ionization on the Earth (up to 3 km altitude) is ionizing radiation in a radioactive decay. For example, the average ionization rate due the natural presence of radon is $10 \text{ cm}^{-3}\text{s}^{-1}$, which translates to an equilibrium ionization density of 10^3 cm^{-3} [18]. However, when streamers in clean gases are studied experimentally in metallic chambers, this source is negligible, and other sources of ionization should be considered.

Natural background ionization can be caused by cosmic rays that penetrate our atmosphere and create secondary particles. Some of them are energetic enough to reach the sea level and to penetrate enclosed metallic chambers. The average source rate of this pre-ionization measured in enclosed metallic chambers is about $10 \text{ cm}^{-3}\text{s}^{-1}$ [19].

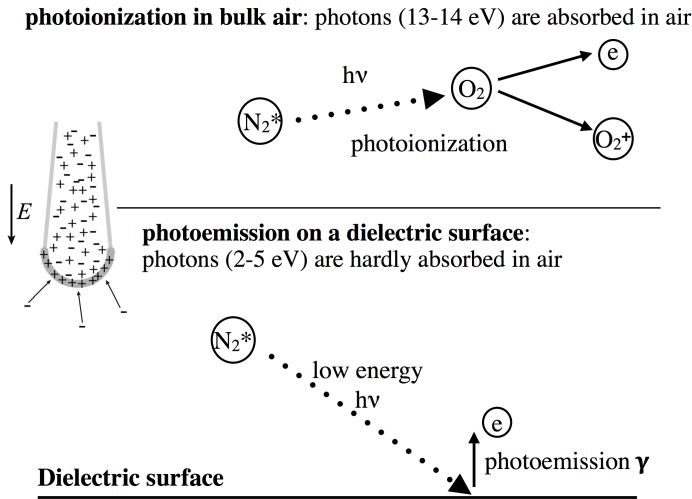


Figure 1.3: Illustration of photoionization and photoemission mechanisms in air.

Another source of background ionization appears in repetitive discharges. If the repetition frequency is sufficiently high, ionization remaining from the previous discharge does not have enough time to decay. Hence, a new discharge develops not in a virgin gas, but in a pre-ionized gas. The level of pre-ionization grows with the repetition frequency.

Photoionization and photoemission are two very important nonlocal sources of free electrons for positive discharges. Their mechanisms are very similar: an excited molecule (N_2^* in air) emits a photon that can be absorbed by another molecule (O_2 in air) or it can be absorbed by a surface (dielectric or conductive) at some distance away from its source and thus liberate an electron (see figure 1.3). The importance of these two processes, in particular for positive streamers, is explained with the fact that they are intrinsic. In other words, positive streamers can feed themselves with free electrons due to photoionization and photoemission. The difference between these two mechanisms lies in the energy of the photons and in the absorption length. In air, photoionization is initiated by photons of 13-14 eV and the photoionization length is about 1.3 mm at standard temperature and pressure (STP). Photoemission from a dielectric surface can be produced by photons of energy as low as 2-5 eV. These photons are hardly absorbed in air and they can free electrons from a surface a large distance away from the source.

Secondary electron emission from a dielectric or conductive surface due to electron or ion bombardment can also be a source of electrons. These are, however, local phenomena in contrast to photoionization. And so is the field induced electron emission, which becomes stronger with increasing electric field.

In STP air, free electrons attach to oxygen molecules mostly by three-body attachment and the negative ions O_2^- have a longer life time. Therefore, in dry air at STP the background ionization is present in form O_2^- . When an electric field is applied,

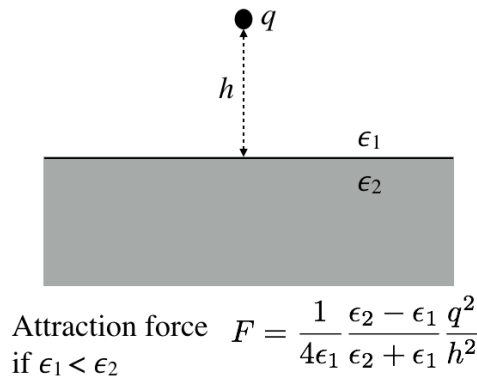


Figure 1.4: Electric charge is attracted to a dielectric due to polarization of the dielectric.

electrons detach from the negative ions and become available for an electron avalanche [20].

1.4 Influence of dielectrics

1.4.1 Field effects of a dielectric

In the presence of an electric field, the dipoles inside a dielectric orient in such a way as to screen the electric field. The ability of a dielectric to polarize is characterized by its dielectric permittivity ϵ . In the limit $\epsilon \rightarrow \infty$ a dielectric screens an electrostatic field completely like a conductor.

When a charge is placed near a dielectric with ϵ larger than that of the surrounding media, the charge is electrostatically attracted to the dielectric with a force independent of the sign of the charge (see figure 1.4). Therefore, when an electric discharge propagates near a dielectric, it experiences (among other forces) attraction to the dielectric.

1.4.2 A dielectric as a source and sink of free electrons

A dielectric can trap charges by attracting them and it can thus deprive a streamer of free charges, which can stall its propagation. The higher the dielectric permittivity, the stronger a dielectric can attract charges in a given electric field. On the other hand, a dielectric can block photoionization, which is essential for positive streamers in air. And thus some areas will be avoided by positive streamers. A dielectric surface can also emit electrons due to various emission processes already mentioned in section 1.3.3 and extensively discussed in chapter 2. Basically, there is a multitude of processes that are invoked by the presence of a dielectric. The challenge is to pinpoint the dominant mechanism.

1.5 Questions addressed in the thesis

Positive streamers are very sensitive to sources of free electrons, and a dielectric surface can be one of them. In chapter 2 we give an extensive overview of various types of electron emission from a dielectric surface and offer ways of their numerical implementation. We focus primarily on photon induced secondary electron emission. It is a nonlocal source of free electrons and it can change streamer affinity to a dielectric (an example is given in chapter 5).

In chapter 3 we discuss various streamer discharge models and their applications. The bottleneck of almost all streamer models is the Poisson solver. This problem becomes even more challenging when dielectric or conductive interfaces are present in a simulation domain. We describe an efficient method called the Ghost Fluid Method that allows to deal with this problem. This method was developed initially for a rectangular grid, but we translate it to a cylindrical grid.

In chapter 4 we focus on streamer affinity to a dielectric rod in air and in pure nitrogen. We have designed a specific cylindrically symmetric setup such that a streamer can be studied both experimentally and numerically in cylindrical geometry. With that setup we have studied how a positive streamer interacts with a dielectric rod in pin-to-plate electrode geometry and we have compared the results with the experiments performed by D. Trienekens. In the course of this work we identified the shading effect for photoionization and photoemission. We have also understood that a cylindrical streamer that moves around a dielectric rod (a “hollow” ring-like streamer) experiences two competing forces: its attraction to the dielectric rod and its self-repulsion. The latter is specific for a cylindrical geometry. Curious about this finding, we designed a different set of numerical experiments, which we discuss in chapter 5.

In chapter 5 we use a plate-to-plate electrode setup with a dielectric rod in the middle with an anode embedded into it. In this cylindrical geometry we have studied the competition of streamer attraction to the dielectric rod and its self-repulsion depending on the dielectric permittivity of the rod and its diameter. We also investigated the role that photoemission plays in changing the competition between these two factors.

In chapter 6 we report the progress that we made in understanding lightning inception in thunderclouds and we perform cylindrically symmetric simulations of lightning inception in its streamer phase. We explain how lightning can start in a sub-breakdown electric field of thunderclouds with no electrons present (on average). In our model the initial electrons are supplied by extensive air showers, and the thundercloud electric field is amplified locally by (dielectric) ice particles due to their polarization. Using ice particles as example, we also discuss the influence of the frequency dependence of the dielectric permittivity on discharge inception.

In chapter 7 we dwell on the fundamental questions of streamer discharge inception from an elongated dielectric in a sub-breakdown electric field. We analyze discharge inception based on the ionization integral and point out the reasons why the Meek criterion is not applicable in some cases. We offer a way to generalize the ionization integral. We also argue that the role of photoionization can be decisive for streamer

inception.

In chapter 8 we study propagation of a positive streamer toward a dielectric tip in a pin-to-plate geometry under voltage pulses with sub-nanosecond rise time. With our fluid streamer model, we simulated a positive streamer in air with photoionization and in pure nitrogen without photoionization. Also, in this case photoionization appears to play an important role.

Finally, in chapter 9 we present an alternative method of calculating photoionization and photoemission. The method is based on treating the photon absorption coefficient as a virtual variable. We give examples of how our method works in air and pure nitrogen and we compare the results with other methods and with analytical results.

Chapter 2

Electron emission from a dielectric surface

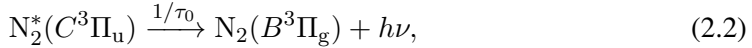
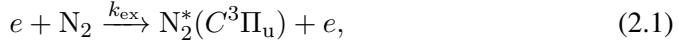
There are a multitude of processes on dielectric surfaces resulting in electron emission. Secondary electron emission due to ion or metastable atom bombardment, field electron emission and photon induced electron emission are among them. Our primary goal is to accurately calculate positive streamer propagation along a dielectric rod. In some experiments, e.g., [21–24] a positive streamer propagates faster along the dielectric rod than in the bulk gas. We expect that photon induced secondary electron emission is responsible for this effect. Due to this intrinsically nonlocal mechanism there are always electrons in front of the streamer, whereas other mechanisms mentioned above are local. However, when the electric field becomes very high, for example in the presence of a surface discharge, other processes can become important. In this chapter, we give a short summary of potentially important processes on dielectric surfaces and explain how they can be implemented into a code.

2.1 Photoemission from the dielectric rod

2.1.1 The physical phenomenon

A streamer discharge in air can be a source of visible and ultraviolet radiation with photons of energies 2.27-4.63 eV (280-440 nm) which are produced by the second positive system (SPS) of molecular nitrogen corresponding to the $N_2^*(C^3\Pi_u) \rightarrow N_2(B^3\Pi_g)$ transition. These photons are hardly absorbed in air. Radiation due to the first positive system is dominant for sprite discharges in the thin air of the terrestrial mesosphere [14, 25] but quenched at higher pressures.

In order to write the kinetic equation of balance for $N_2^*(C^3\Pi_u)$, we need to consider the reactions of impact and photoionization (2.1) and (2.2) and the competing reaction associated with the interaction of the excited nitrogen with other molecules, which leads to quenching of (2.3) and (2.4). In nitrogen-oxygen mixtures these reactions read [26]:



where e represents the electron, and $h\nu$ is energy of a photon emitted during de-excitation. Further, k_{ex} is the rate of excitation reaction (2.1), $\tau_0 = 42$ ns is the radiative lifetime, and $k_q^{N_2} = 0.13 \cdot 10^{-10}$ cm³/s and $k_q^{O_2} = 3.0 \cdot 10^{-10}$ cm³/s are the quenching rate constants on the N_2 and O_2 molecules, respectively. The dependence of the rate constant of electronic excitation on the reduced electric field $k_{\text{ex}}(E/N)$ was calculated using BOLSIG+ [27], and the lifetime and the quenching rate constants were taken from [28].

The density of $N_2^*(C^3\Pi_u)$ in reactions (2.1)-(2.4) can thus be calculated by solving the following kinetic equation [26]

$$\frac{d[N_2^*]}{dt} = k_{\text{ex}}n_e[N_2] - \frac{[N_2^*]}{\tau}. \quad (2.5)$$

Here, τ is the total lifetime of the radiating state, defined as the inverse rate of three parallel decay processes (i.e., via the sum of the three rates)

$$\frac{1}{\tau} = \frac{1}{\tau_0} + k_q^{N_2}[N_2] + k_q^{O_2}[O_2]. \quad (2.6)$$

According to equation (2.2), the production rate of the photons can be estimated as

$$P(\mathbf{r}, t) = \frac{[N_2^*]}{\tau_0}. \quad (2.7)$$

In a quasi-stationary approximation, where $d[\text{N}_2^*]/dt \equiv 0$, the production of photons can be calculated as follows

$$P(\mathbf{r}, t) = \frac{\tau}{\tau_0} Q(\mathbf{r}, t), \quad (2.8)$$

where $Q(\mathbf{r}, t) = k_{\text{ex}} n_e [\text{N}_2]$ is the excitation source term by electron impact. Making use of the fact that $[\text{N}_2]$ and $[\text{O}_2]$ are proportional to total pressure, we can write equation (2.8) in the same form as in equation (4.8) for the production of photons in photoionization in air (for plasmas with low excitation and dissociation ion densities):

$$P(\mathbf{r}, t) = \frac{p_q}{p + p_q} Q(\mathbf{r}, t), \quad (2.9)$$

where p_q essentially stands for collisional quenching. Along with photoionization, we assume that the quasi-stationary approximation is valid.

The photons produced in reaction (2.2) are considered the main source of electrons from dielectric surfaces. Since the lower energy photons creating photoemission can travel farther before being absorbed than the higher energy photons creating photoionization (see section 4.2.4 in chapter 4), it is presumed (e.g., in [29]) that an ionization wave next to a dielectric surface will travel with larger velocity than an ionization wave without a surface.

We include photoemission from the dielectric surface S_{pe} in equation (4.2). At every time step we calculate the flux of photons onto every point on the dielectric surface. The flux of photoelectrons from the dielectric surface is proportional to the flux of photons times photoemission yield γ . Thereby, the emitted electrons are put just outside of the surface and become bulk electrons; ions stay immobile on the surface.

2.1.2 Numerical implementation

The influence of photoemission on the streamer discharge propagation has previously been studied, for example, in [30, 31], where the photon source was integrated directly. We, for the first time, consider a geometry with a profound shading effect. In appendix 3.5, we describe the implementation of the photoemission that we use in our simulations.

Alternatively in [32], a direct method for the radiative transfer equation is proposed. It is based on applying the finite volume method to the radiative transfer equation in the conservative form. The authors restrict their studies to the cylindrically symmetric case and to monochromatic radiation. This method is computationally more efficient than the direct integration proposed in [33, 34]. It works well for any absorption coefficient. The authors of [32] calculate the photon distribution function. If the photons are monochromatic, the function depends on the spatial coordinates and on the photon propagation direction. In 3D, these are three spatial and two angular coordinates. So, a PDE in five dimensions has to be solved. Since the photon direction is included in that equation, the photon flux on a surface can be directly implemented. The boundary

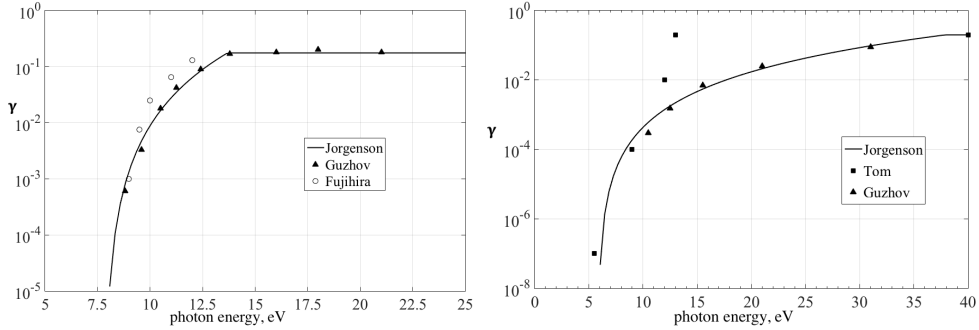


Figure 2.1: Photoemission yield γ from polyethylene (left) and teflon (right) as a function of the photon energy. The data was obtained from [29, 40, 45, 46].

needs to be treated properly. One way is to artificially introduce a very large absorption coefficient in the dielectric so that all photons have to be absorbed on the dielectric surface.

2.1.3 The uncertainty about the photoemission yield

The probability of a photon to liberate an electron is called photoelectron emission yield γ . It depends on the material of the dielectric, the properties of the dielectric surface (roughness, accumulated charge, etc), and on properties of the plasma produced by a streamer discharge in a gas.

The photoelectron emission is fairly well understood and experimentally measured for metals in vacuum [35]. In gases, and especially when a discharge develops near the emitting surface, the experimental data are scarce. It is argued that the photoemission yield can increase by even an order of magnitude [36] and reach the values from 0.1 to 1.0 for photons with wavelength less than 100 nm. The large values of γ are explained by the adsorbed atoms that contaminate the surface. They absorb the resonant radiation produced by a discharge and the resonant state is deactivated in the Auger process. These experiments have been performed in noble gases like Kr, Xe, He.

Photoemission from dielectrics in air (or nitrogen-oxygen mixtures) is less understood than photoemission from metals. The development of avalanches in the vicinity of some dielectrics (polyethylene) in pure gases or in vacuum were studied in [37–43]. For the photons of 280–440 nm (SPS N_2), the photoemission yield is estimated as $\gamma = 10^{-7}$, which is very small. The value of γ increases for photons with shorter wavelength. However, those photons are absorbed in air and cannot serve as a nonlocal source of free electrons necessary for positive streamers. There are also exotic materials such as ferroelectrics for which electron emission can be anomalously high [44], but we do not consider them for practical reasons.

We assume that the photoemission yield is in the huge range of 10^{-7} to 1, and we study the sensitivity of the discharge to its actual value.

2.2 Secondary electron emission due to ion bombardment

2.2.1 The physical phenomenon

Ions produced due to impact ionization can hit a dielectric surface and liberate an electron. When an ion approaches a dielectric surface, its electric field modifies the potential barrier on the surface. This is a local effect called the Auger neutralization. The modified barrier becomes low and an electron from the surface tunnels into the ion and neutralizes it. If the excess of energy is large enough, it can be spent on the emission of another electron. Similarly, a metastable atom can cause secondary electron emission accompanied with its de-excitation. This process is known as Auger deactivation. For low or moderate kinetic energies less than 1 keV, these processes are similar [35].

The secondary electron production rate is quantified by the electron yield γ which tells how many electrons are produced per bombarding particle (an ion or a metastable atom). The electron yield is assumed to be proportional to the maximal energy E_{\max} of an electron emitted from a dielectric surface. The work function W is the minimal energy needed to remove an electron from a dielectric surface and to place it just outside the surface with the electrostatic potential ϕ and therefore it is a property of the surface, but not of the bulk dielectric material. The Fermi-level E_f is the minimal energy needed to remove an electron from a surface to a state with zero energy. Then, we have the following relation

$$W = -e\phi - E_f. \quad (2.10)$$

For the Auger neutralization, E_{\max} can be estimated as the difference between the ionization potential E_{ion} and the work function W for electrons in the dielectric $E_{\max}^{\text{in}} = E_{\text{ion}} - W$ and out of the dielectric $E_{\max} = E_{\text{ion}} - 2W$. For the Auger deactivation, the maximal electron energy outside the dielectric can be estimated as $E_{\max} = E_{\text{met}} - W$, where E_{met} is the excitation energy of the metastable atoms [47].

2.2.2 Numerical implementation

An ion current onto the dielectric surface can be calculated, for example based on the fluid model, but on the nanosecond time scale it is negligible at low fields, because ions move very little, as can be deduced from figure 2.2.

Often the electron outflow is assumed to be 10 times smaller than the ion inflow (the secondary electron coefficient is 0.1), e.g. in [34, 48]. In fact, by using this somewhat high value of the secondary electron emission, other types of secondary electron emission such as photoemission and emission by impact of metastable atoms can be accounted for.

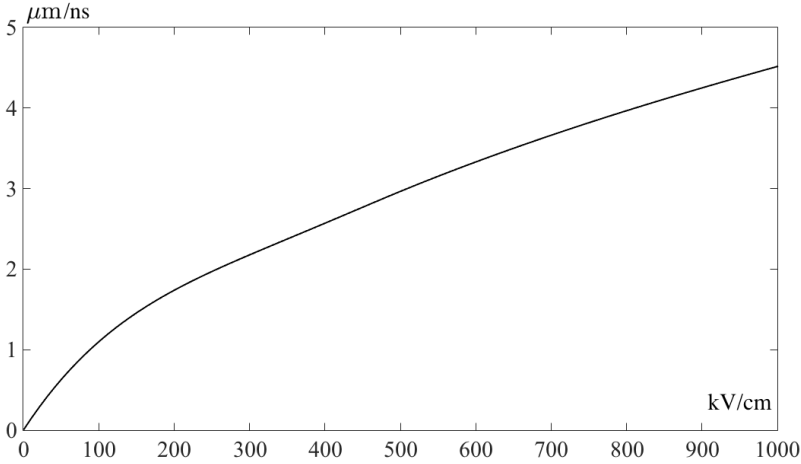


Figure 2.2: Velocity of N_2^+ in N_2 at STP as a function of the electric field, based on the cross sections from [49] and the transport data was calculated with BOLSIG+ [50].

2.3 Electron emission in an external electric field (field emission)

2.3.1 The physical phenomenon

A streamer approaching a dielectric surface can enhance the electric field on it. So, the effective potential barrier perceived by electrons on the surface will become smaller. This is known as the Schottky effect or de-trapping.

Electrons can also be trapped on a dielectric surface during a previous discharge (for example, in repetitive discharges). The typical depth of such traps is of the order of a few electronvolt [51]. These electrons can be later de-trapped by a process which should also obey the Richardson-Schottky scaling.

The effect is expected to play an important role because the enhanced streamer electric field in the vicinity of a dielectric surface can reach 150 – 200 kV/cm, and for fields higher than 100 kV/cm a considerable field emission is expected [52, 53].

This mechanism is relevant for electric fields less than about 10^3 kV/cm in vacuum. For electric fields higher than 10^3 kV/cm (or somewhat lower in air), the so-called Fowler-Nordheim tunneling can contribute to the emission of electrons. In [54], the current density j due to the tunneling generation of negative ions (electron transfer from a surface onto positive ions near the surface) is compared to the current density of the Fowler-Nordheim emission. The emission starts at lower electric fields and the current density is proportional to the gas density N :

$$j \sim \omega v_T N, \quad (2.11)$$

where v_T is thermal velocity and ω is the probability of a negative ion formation.

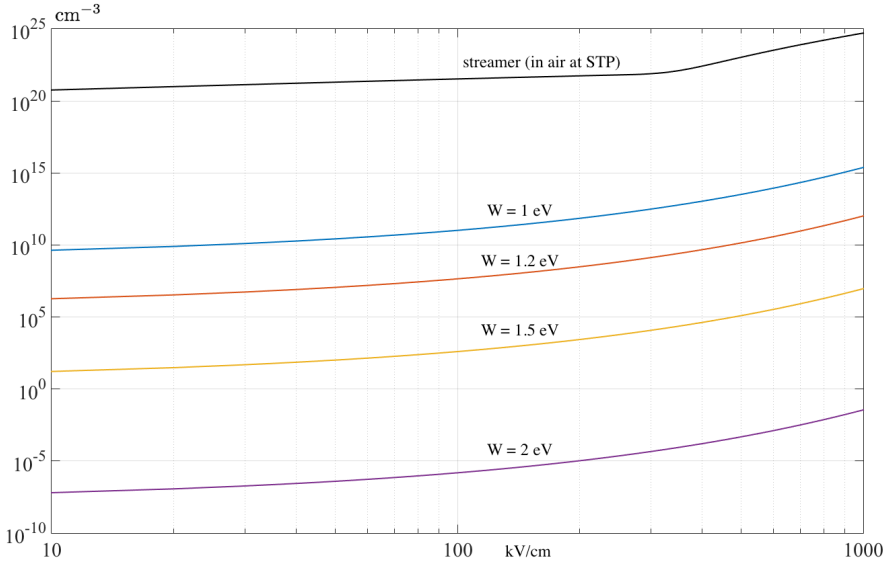


Figure 2.3: Electron current density due to field emission at 300 K as a function of electric field for the work function W of 1 eV, 1.2 eV, 1.5 eV, and 2 eV, as given by equation (2.12). The black line shows electron current density of a streamer in air at STP: $j = n_e \mu E$, assuming $n_e = 10^{14} \text{ cm}^{-3}$. For comparison, for a weakly conducting PyrexTM $W \simeq 1.2 \text{ eV}$ [51], and for polyethylene $W = 4.5 \text{ eV}$ [29].

2.3.2 Numerical implementation

Using the Richardson-Schottky law, the electron outflow can be calculated as

$$J = AT^2 \exp\left(-\frac{W - \Delta W}{kT}\right), \quad (2.12)$$

where W is the local work function (the height of the surface barrier seen by an escaping Fermi-level electron), T is temperature, k is the Boltzmann constant, the constant $A = 120 \text{ A/cm}^2/\text{K}^2$, and

$$\Delta W = \sqrt{\frac{e^3 E}{4\pi\epsilon_0}}. \quad (2.13)$$

Here E is the value of the electric field, e is the elementary charge, ϵ_0 is the electric constant. Further information can found in paper [55].

The de-trapping of the trapped electrons is described by the equation similar to equation (2.12):

$$J = \nu_0 N_{\text{dt}} \exp\left(-\frac{W - \Delta W}{kT}\right), \quad (2.14)$$

where N_{dt} is the surface density of detrappable charge carriers, $\nu_0 \sim 10^3 - 10^4 \text{ s}^{-1}$ is the fundamental phonon frequency. The former is assumed to be proportional to the

deployed surface charge q . The trapped charges are depleted by loss mechanisms such as emission, diffusion into deeper traps and other processes [51].

Chapter 3

Numerical modeling of streamers

The main advantage of numerical simulations over experiments is that in simulations it is known precisely what physical mechanisms are included. Besides, the role of the mechanisms included is often easier to track by, for example, switching off some of them completely or by intensifying them to an artificial degree. In experiments, all the possible processes are present at all times, and determining the importance of each of them can be challenging. Performing a parametric study is also usually easier in simulations than in experiments. On the other hand, simulations are always based on simplifying assumptions that can be difficult to justify a priori. In this chapter we discuss the challenges in streamer modeling that arise nonlinearity and multiscale nature. We also give a brief overview of the most common streamer models, including the fluid model, which we use in this thesis. One of the bottlenecks of almost all streamer models is calculation of the electric field, which also deserved attention in the present chapter. Here we also dwell on the Ghost Fluid Method for solving the Poisson equation in simulation domains containing dielectric or conductive interfaces. Finally, we focus on the implementation of the photoemission from a cylindrical surface with a shading effect.

3.1 Challenges in streamer modeling

Streamer simulations pose multiple numerical challenges. Firstly, the dynamics of streamers is highly nonlinear, because the electric field is coupled with the space charge layer at the streamer head. Besides, since the space charge layer has a curvature, one dimensional modeling does not suffice. Secondly, streamer discharges are spatially multiscale phenomena. The space charge layer at the head of streamer is very thin and curved and it is of the order of a few electron mean free paths, which is a few micrometers in atmospheric air. At the same time, the typical propagation length of streamers is centimeters or more. This means that a streamer model has to be able to resolve at least these two length scales separated by four orders of magnitude. Streamers are also temporally multiscale phenomena. The typical time development of streamers is usually tens of nanoseconds (at STP), whereas the smallest important time scale is a few picoseconds or even smaller. The smallest time scale is partly dependent on the numerical implementation of a streamer model. For example, in particle streamer models, in which individual electrons are tracked, the collision time is a relevant time scale, which can be as small as 10^{-13} s. In fluid streamer models, one of the most important time step restrictions is the Courant-Friedrichs-Levy criterion, which is a necessary condition for the convergence of the fluid equations. Simply put, the criterion says that electrons cannot move more than a grid cell (of the order of the electron mean free path) in one time step. This gives an upper bound estimate of 10^{-11} s for the time step. Moreover, streamers are intrinsically nonlocal phenomena, which makes it difficult to efficiently parallelize the numerical implementation. The non-locality of streamers is attributed to the non-locality of the electric field (and photoionization in air).

Simulations of streamers near dielectric and conductive interfaces complicate the numerical implementation even more. The boundary conditions on the interfaces lead to steep gradients and even discontinuities of the electric field, as well as of the charge density. Resolving the electric field on the boundary, and in particular on a curved boundary that does not follow the grid lines, is not trivial. Dedicated numerical methods are therefore required such as the Ghost Fluid Method [56, 57].

All this makes streamer simulations challenging to design and computationally costly to run.

3.2 Overview of streamer models

3.2.1 Particle models

In particle streamer models, single electrons are followed over a period of time. The electrons gain energy in an electric field or lose energy in a collision with a neutral molecule. The probabilistic nature of electron collisions is modeled with a Monte-Carlo technique. At every time step it is randomly decided whether an electron undergoes a collision and what the result of this collision is, based on the cross-section data. One of the advantages of particle models is that few simplifying assumptions are made a priori

and therefore, the microscopic physics of streamers is described in a straightforward way. Moreover, by introducing a random numerical noise particle models emulate the real particle density fluctuations. However, with the increasing number of particles, particle simulations become computationally prohibitively expensive. This makes particle models a perfect tool to describe, for example, streamer inception, when there are still few particles and the role of particle density fluctuation is important.

To reduce the computational cost of particle simulations, a number of techniques have been developed. For example, electrons with similar properties can be grouped and merged into so called super-particles, which can later be split back into single particles [58].

Due to the non-locality, calculation of the electric field created by a large number of particles interacting with each other is much easier when particles are mapped into a grid as a charge density instead of calculating electric field directly from the superposition principle. After the electric field is calculated by solving the Poisson equation, it is interpolated back to the particles.

Optimization of particle models comes with the cost of introducing an artificial stochastic noise, the influence of which it can difficult to interpret.

3.2.2 Fluid models

In fluid models, particles are described with their average density, which satisfy the continuity equations:

$$\frac{\partial n}{\partial t} = \nabla \cdot \mathbf{j}(\mathbf{E}, \mathbf{r}) + S(E, \mathbf{r}), \quad (3.1)$$

where n is the density, \mathbf{j} is the flux due to drift in a electric field and due to diffusion, and S stands for sources such as electron impact ionization, photoionization, electron emission from a surface, etc. The transport equations 3.1 in fluid models are coupled with the Poisson equation for the electric potential ϕ :

$$\nabla(\epsilon \nabla \phi) = -\frac{\rho}{\epsilon_0}, \quad (3.2)$$

$$E = -\nabla \phi, \quad (3.3)$$

where ρ is the charge density. A lot of streamer models are based on the assumption of local equilibrium, which means that the transport and reaction coefficients are functions of local parameters only. For example, in the local field approximation, this local parameter is the electric field. The coefficients as functions of the electric field can be measured or calculated using swarm simulations in a Monte-Carlo particle model.

Fluid equations can be derived in a rigorous way from the Boltzmann equation for the particle distribution function in phase space. The particle density is the zeroth order velocity moment of the distribution function, and flux is its first, and so on. This leads to an infinite chain of equations, which is truncated using closure assumptions, depending on the phenomena studied and the accuracy required. In [59, 60], it was demonstrated that sometimes in streamer simulations one has to derive equations up to

the third moment, as the energy flux is not constant and this leads to a correction of streamer velocity.

Simulations based on fluid streamer models are deterministic and unlike particle models they do not produce any stochastic noise. They are also typically faster to run, but the underlying assumptions of fluid models have a limited validity. For example, at the inception phase of a discharge, there are few particles present and averaging may lead to big numerical errors.

In all streamer simulations in this thesis, a 2D cylindrical fluid model is used.

3.2.3 Hybrid models

Hybrid models combine the efficiency of fluid models with the accuracy of particle models. In a spatially hybrid model [61] the majority of electrons inside a streamer are treated as a fluid with a density approximation, whereas electrons in regions with lower electron densities and high field are treated with a full particle model. This hybrid model [62], for example, can predict runaway electrons from streamers, besides correctly tracing the high electron energies in space and both electron density fluctuations and electron energy fluctuations.

3.2.4 Tree models

The filamentary structure of streamers can also be studied on a macroscopic level with a tree model, in which the filaments of a branched discharge are approximated with a growing network of conducting cylindrical channels. The model was first proposed in [63] to describe the fractal discharge pattern of dielectric breakdown on a plane. In [64], the authors extended the model to 3D and elaborated on the charge conservation and the charge transport within the discharge tree. The tree models largely rely on model reductions for streamer channels, which are still to be established.

3.3 The challenge of solving the Poisson equation in streamer simulations

In streamer simulations the electric field is computed in the electrostatic approximation at each time step by solving the Poisson equation for the electric potential and calculating its gradient. Solving the Poisson equation (3.3) accurately and fast is one of the bottlenecks of all streamer models. One big difficulty stems from the non-locality of the Poisson equation. Basically, the information from all the sources has to be passed everywhere in a simulation domain and thus the problem size grows as N^2 , if N is the number of grid points.

All the methods for solving the Poisson equation can be split in two groups: direct and iterative. In direct methods, the Poisson equation is discretized on a mesh, and the discretization matrix is inverted with machine precision. The discretization matrix of

the Poisson equation is sparse, symmetric and positive definite which allows to optimize the solver. Besides, if the mesh is static, the inversion can be done only once at the beginning of a simulation and stored in some convenient pre-factorized way, such as in MUMPS [65]. Hence, computing the solution would take only a linear time. In direct methods, the computational error is determined by the accuracy of the discretization matrix. On the other hand, direct methods become prohibitively expensive in 3D, when the size of the problem reaches more than 10^7 grid points.

In iterative methods, the solution is first guessed or taken from the previous time step. Then, it is plugged into the Poisson equation and the correction is calculated to improve the solution until it satisfies the Poisson equation with a given accuracy. How fast the initial guess converges to the solution depends, for example, on the initial guess, on the source distribution, etc. Iterative methods require less memory and they can be very efficient when the solution is smooth, but in simulation domains with internal dielectric or conductive boundaries (in general not coinciding with the mesh) they converge slowly, because on those boundaries the solution has sharp gradients or even discontinuities. Iterative methods can be combined with direct methods as pre-conditioners (e.g., GMRES [66]), which solve the Poisson equation on a rough mesh to improve the initial guess.

To reduce the number of grid points in a problem adaptive meshes are proposed. With time such meshes change their level of refinement and/or the area of the simulation domain that they cover, depending, for example, on where the streamer head with high electric field is moving. Three-dimensional streamer simulations are hardly imaginable without any sort of adaptive meshes. However, resolving the solution of the Poisson equation in a domain with conductive or dielectric interfaces becomes very cumbersome as the precise location of each boundary cell with respect to all neighboring cells has to be accounted for every new mesh.

3.4 Ghost Fluid Method (GFM)

The accurate calculation of the electric field at every time step even at the thin space charge layer around the streamer head is an essential and computationally expensive part in the vast majority of streamer models. The calculation is based on solving the Poisson equation by calling an external package (e.g., FISHPACK [67]). But the presence of a dielectric or a conductive interface in a simulation domain makes it complicated because discontinuous boundary conditions have to be imposed inside the domain in an accurate way, and the CPU time must be kept short. There is a variety of numerical recipes offering different ways of dealing with contact discontinuities. In our simulations a generalized Ghost Fluid Method was chosen due to its multiple advantages.

Originally, GFM was developed to capture discontinuities in the inviscid Euler equations [68], but later it was generalized to treat shocks, detonations, and compressible viscous flows. A similar idea was also applied to the Poisson equation with variable and discontinuous dielectric permittivity [56] on a Cartesian grid. The idea was later

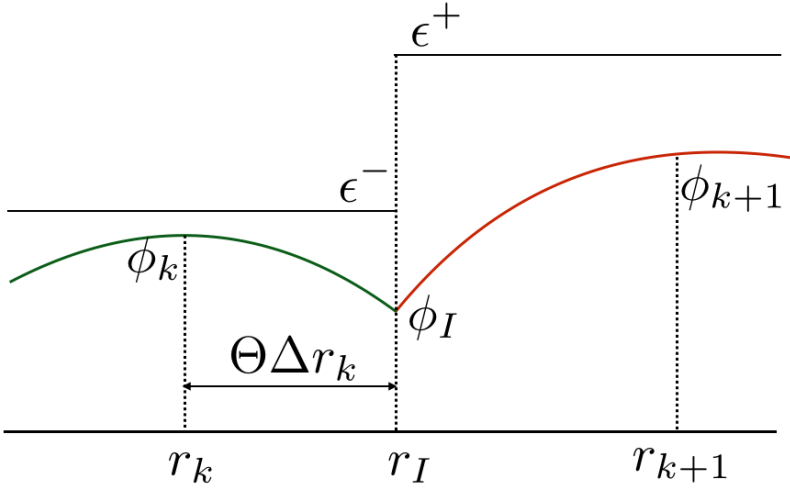


Figure 3.1: Subcell interface discretization.

generalized for the Poisson equation describing the electric potential in a cylindrically symmetric domain with a curved electrode [57] and was used to simulate a streamer discharge in a point-to-point geometry.

The generalized GFM for the Poisson equation offers a number of benefits. Firstly, the solution is not smeared out on the interface, unlike in the immersed boundary method [69]. Secondly, the implementation is relatively simple and allows extension to multi-dimensions. Thirdly, the discretization matrix for the Poisson equation remains sparse, which can speed up the matrix inversion. Moreover, the method can treat any shape of the interface. The downside of the method is that it is only first order accurate on the interface. Another issue for consideration is compatibility with adaptive mesh refinement, often used in streamer simulations. Both these issues were solved, e.g., in [70], however that complicated the method.

In what follows we adapt the Ghost Fluid Method from [56] developed on a Cartesian grid to a cylindrical grid ¹.

3.4.1 GFM for the Poisson equation with a discontinuous dielectric permittivity on a cylindrical grid

Let us consider, for the sake of clarity, a one-dimensional Poisson equation in a cylindrical geometry (the method can be extended to 2D or 3D):

$$\frac{1}{r} \frac{\partial}{\partial r} \left(\epsilon r \frac{\partial \phi}{\partial r} \right) = f(r), \quad (3.4)$$

¹A direct Poisson solver for a cylindrical geometry with the GFM included was developed and used in all streamer simulations in this thesis.

where ϕ is the (electric) potential, ϵ is the dielectric permittivity that undergoes a jump at an interface point $r = r_I$, $f(r)$ is the source term. We assume that the potential at $r = r_I$ is continuous, but the electric field $\partial\phi/\partial r$ is discontinuous and the change of the electric displacement field $\epsilon\partial\phi/\partial r$ equals to the surface charge σ

$$\left[\epsilon \frac{\partial\phi}{\partial r} \right]_{r_I} = \sigma_I, \quad (3.5)$$

as shown in figure 3.1).

A standard second order discretization of the Poisson equation as given for *any* grid point i by equation (3.4) reads

$$\frac{1}{0.5(r_{i+1} - r_{i-1})r_i} \left[(\epsilon r)_{i+1/2} \left(\frac{\phi_{i+1} - \phi_i}{r_{i+1} - r_i} \right) - (\epsilon r)_{i-1/2} \left(\frac{\phi_i - \phi_{i-1}}{r_i - r_{i-1}} \right) \right] = f(r_i). \quad (3.6)$$

Depending on the grid resolution, r_I can be located within a grid cell. If its subcell location is not taken into account, that the interface jump condition will be smeared out over the cell containing the interface. In some applications, such as streamer simulations near dielectrics, it is important to know the accurate value of the electric field at the surface. Therefore, let us discretize the interface condition in equation (3.5) taking the subcell resolution into account. We assume that the interface lies between two *special* grid point k and $k + 1$. Then,

$$\epsilon^+ \left(\frac{\phi_{k+1} - \phi_I}{(1 - \Theta)\Delta r_k} \right) - \epsilon^- \left(\frac{\phi_I - \phi_k}{\Theta\Delta r_k} \right) = \sigma_I, \quad (3.7)$$

where $\Delta r_k = r_{k+1} - r_k$, ϵ^\pm is the dielectric permittivity on the two sides from the r_I , and Θ is used to estimate the subcell interface location. For example, Θ can be defined as

$$\Theta = \frac{r_I - r_k}{\Delta r_k}. \quad (3.8)$$

From equation (3.7) we can linearly approximate the potential on the interface

$$\phi_I = \frac{\epsilon^+ \phi_{k+1} \Theta + \epsilon^- \phi_k (1 - \Theta) - \sigma_I \Theta (1 - \Theta) \Delta r_k}{\epsilon^+ \Theta + \epsilon^- (1 - \Theta)} \quad (3.9)$$

Thus, the approximations for the derivatives on the left and the right sides of the dielectric interface can be written as

$$\begin{aligned} \epsilon^- \left(\frac{\phi_I - \phi_k}{\Theta\Delta r_k} \right) &= \hat{\epsilon} \left(\frac{\phi_{k+1} - \phi_k}{\Delta r_k} \right) - \frac{\hat{\epsilon}\sigma_I(1 - \Theta)}{\epsilon^+}, \\ \epsilon^+ \left(\frac{\phi_{k+1} - \phi_I}{(1 - \Theta)\Delta r_k} \right) &= \hat{\epsilon} \left(\frac{\phi_{k+1} - \phi_k}{\Delta r_k} \right) + \frac{\hat{\epsilon}\sigma_I\Theta}{\epsilon^-}, \end{aligned} \quad (3.10)$$

where

$$\hat{\epsilon} = \frac{\epsilon^+ \epsilon^-}{\epsilon^+ \Theta + \epsilon^- (1 - \Theta)}. \quad (3.11)$$

And a pair of equations containing $\phi_{k+1} - \phi_k$ of the discretization stencil should be corrected as

$$\begin{aligned} & \frac{1}{0.5(r_{k+1} - r_{k-1})r_k} \left[\hat{\epsilon}r_{k+1/2} \left(\frac{\phi_{k+1} - \phi_k}{r_{k+1} - r_k} \right) - (\epsilon r)_{k-1/2} \left(\frac{\phi_k - \phi_{k-1}}{r_k - r_{k-1}} \right) \right] \\ &= f(r_k) + \frac{\hat{\epsilon}\sigma_I(1 - \Theta)}{0.5(r_{k+1} - r_{k-1})\epsilon^+}, \\ & \frac{1}{0.5(r_{k+2} - r_k)r_{k+1}} \left[\hat{\epsilon}r_{k+3/2} \left(\frac{\phi_{k+2} - \phi_{k+1}}{r_{k+2} - r_{k+1}} \right) - (\epsilon r)_{k+1/2} \left(\frac{\phi_{k+1} - \phi_k}{r_{k+1} - r_k} \right) \right] \\ &= f(r_{k+1}) + \frac{\hat{\epsilon}\sigma_I\Theta}{0.5(r_{k+1} - r_{k-1})\epsilon^-}. \end{aligned} \quad (3.12)$$

The method, clearly, does not change the structure of the stencil, but only corrects some of its values. The same approach is used for discretization in the z direction. In this case, for a uniform grid spacing Δz in equations (3.12) read

$$\begin{aligned} \frac{1}{\Delta z^2} \left[\hat{\epsilon}_{k+1/2} (\phi_{k+1} - \phi_k) - \epsilon_{k-1/2} (\phi_k - \phi_{k-1}) \right] &= f(r_k) + \frac{\hat{\epsilon}\sigma_I(1 - \Theta)}{\Delta z \epsilon^+}, \\ \frac{1}{\Delta z^2} \left[\hat{\epsilon}_{k+3/2} (\phi_{k+2} - \phi_{k+1}) - \epsilon_{k+1/2} (\phi_{k+1} - \phi_k) \right] &= f(r_{k+1}) + \frac{\hat{\epsilon}\sigma_I\Theta}{\Delta z \epsilon^-}. \end{aligned} \quad (3.13)$$

In our streamer simulations, the stencil is factorized at the beginning of a simulation and stored in a factorized way. Every time step when the electric field is to be calculated, a direct solver (e.g., MUMPS [65]) is called and it takes only a linear time to compute the solution, which proved to perform sufficiently fast for our 2D cylindrical simulations.

3.4.2 Level set representation

If there are multiple interfaces in the simulation domain, it is convenient to introduce a level set function for a pair of (neighboring) grid points, which is, for example, negative when there is an interface between those points and positive otherwise. This idea makes it easier to keep track of the interface points and it was extensively used in for simulations in chapter 4.

Consider the following example. Let the interface be a sphere of radius R which can be parameterized as $r^2 + z^2 = R^2$ in cylindrical coordinates. Then, the level set function f_{lsf} can be defined as

$$f_{\text{lsf}}(r_i, z_j; r_{i+1}, z_j) = (r_i^2 + z_j^2 - R^2)(r_{i+1}^2 + z_j^2 - R^2). \quad (3.14)$$

If this f_{lsf} is negative for two points (r_i, z_j) and (r_{i+1}, z_j) , then there is an interface point r_I between r_i and r_{i+1} at z_j , and the stencil equations containing $r_{i+1} - r_i$ have to be corrected according to equation (3.12).

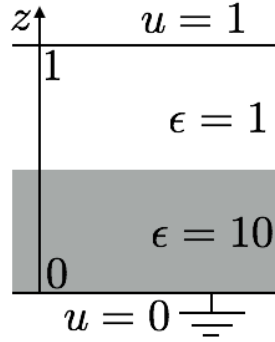


Figure 3.2: Geometry for equation (3.15).

3.4.3 A remark about electrons reaching a dielectric

In streamer discharge simulations near dielectrics, electrons of the bulk plasma move due to drift and diffusion and some of them can reach a dielectric surface. We also assume that once electrons reach a dielectric surface, they stop moving, but still contribute to the electric field. Conceptually, the electrons that reached a dielectric can be treated as surface charge sitting precisely in a mathematically defined interface, essentially σ_1 , or they can be still regarded as electrons of the bulk $f(r)$ that do not move. We choose the latter for the sake of simplicity of implementation.

3.4.4 Example: 1D problem with a dielectric interface

To demonstrate how the Ghost Fluid Method works, let us consider the following one-dimensional example. We solve the Laplace equation

$$\frac{d}{dz} \epsilon \frac{du}{dz} = 0, \quad (3.15)$$

where $u(0) = 0$ and $u(1) = 1$, the parameter ϵ is given by a step function

$$\epsilon = \begin{cases} 10, & 0 \leq z \leq 0.5, \\ 1, & 0.5 \leq z \leq 1. \end{cases} \quad (3.16)$$

At the interface point $z = 0.5$ we assume that u and u_z are continuous on the interface: $[u]_I = 0$ and $[\epsilon u_z]_I = 0$. This example essentially emulates two infinitely wide dielectric layers placed into a voltage gap, as can be seen in figure 3.2. The solution of this problem can be calculated analytically and it is a piecewise linear function

$$u = \begin{cases} \frac{2}{11}z, & 0 \leq z \leq 0.5, \\ \frac{20}{11}z - \frac{9}{11}, & 0.5 \leq z \leq 1. \end{cases} \quad (3.17)$$

Depending on the grid, the interface point may or may not coincide with a grid point. If it does not coincide with any grid points, then the standard second order discretization

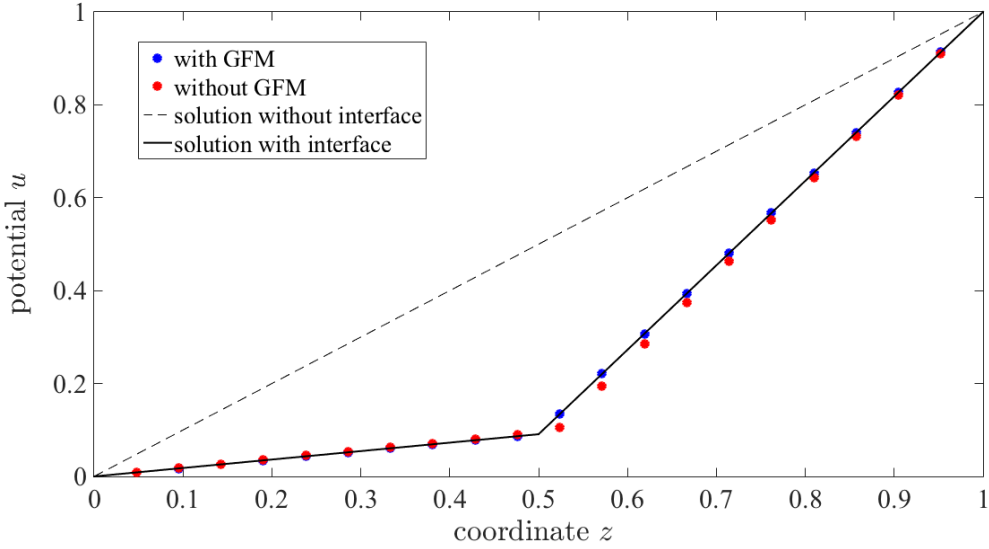


Figure 3.3: Solution u of equation (3.15). The dashed line indicates the solution u , when $\epsilon \equiv 1$. The black solid line shows the exact solution u when ϵ is given by equation (3.16). The red circles show the numerical solution with the standard second order discretization given by equation (3.6). The blue circles show the numerical solution with the standard second order discretization with the Ghost Fluid Method applied. For both numerical solutions we took 20 uniformly spread grid points.

will lead to numerical errors near the interface point, because the first derivative of the u has a jump at $z = z_1$. The special treatment of the discretization at the interface with the Ghost Fluid Method allows to avoid that error. This is clearly illustrated in figure 3.3, where the exact solution of equation (3.15) is shown next to the numerical solution obtained using the standard second order discretization scheme with and without the Ghost Fluid Method.

3.5 Implementation of the flux of photons onto a dielectric rod

The source of photons at any point is assumed proportional to the ionization rate. The photon flux F onto a surface point \mathbf{r} can be obtained by integrating $P(\mathbf{r}')$ in equation 2.8 over the whole volume [71, 72]:

$$F(\mathbf{r}) = \int \frac{P(\mathbf{r}')}{4\pi|\mathbf{r} - \mathbf{r}'|^2} \frac{\mathbf{n} \cdot (\mathbf{r} - \mathbf{r}')}{|\mathbf{r} - \mathbf{r}'|} d^3\mathbf{r}', \quad (3.18)$$

where the second factor under the integral sign in equation (3.18) stands for the cosine of the incidence angle between the vector $\mathbf{r} - \mathbf{r}'$ and the vector \mathbf{n} normal the surface at point \mathbf{r} .

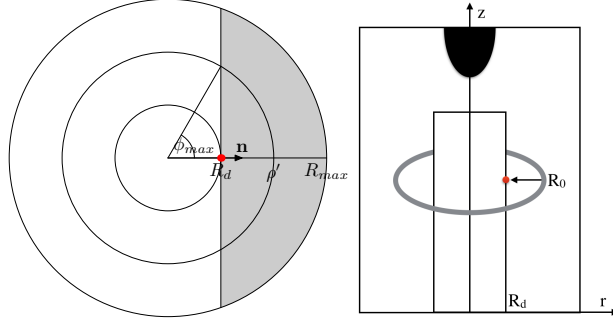


Figure 3.4: Transverse (left) and axial (right) cross-sections of a cylindrical domain with a cylindrical dielectric rod in the middle. Red color indicates the point of observation on the dielectric cylinder. Grey color indicates the area where a source contributes to the emission from the point of observation.

The integral (3.18) can be calculated directly. The direct methods are used in references [33, 34]. The direct integration can be computationally costly. Moreover, due to the shading effect by the dielectric rod (which is assumed opaque for those photons), the number of photons reaching a point on the surface is smaller than it would be in the absence of the rod. The shading effect is geometry dependent and makes the integral in equation (3.18) non-trivial to calculate. Now let us consider a cylindrically symmetric domain with a cylindrical dielectric rod located on the domain axis. Then we have

$$\mathbf{r} = \rho \cos \phi \mathbf{e}_x + \rho \sin \phi \mathbf{e}_y + z \mathbf{e}_z, \quad (3.19)$$

where \mathbf{e}_x , \mathbf{e}_y and \mathbf{e}_z are unit vectors in x , y and z directions, respectively. Due to the cylindrical symmetry we can take the point of observation at $\phi = 0$. The normal vector of dielectric cylinder is given by $\mathbf{n} = \mathbf{e}_x$. Then, the integral (3.18) for a photon flux onto the side of a cylinder can be rewritten as

$$F(R_d, z) = \int_0^{z_{\max}} F_{\text{temp}} dz', \quad (3.20)$$

$$F_{\text{temp}} = \int_{R_d}^{R_{\max}} P(\rho', z') G(\rho', \delta z') \rho' d\rho', \quad (3.21)$$

where z_{\max} and R_{\max} stand for the size of the simulation domain, R_d is the radius of the dielectric cylinder, $\delta z' = z - z'$, and $G(\rho', \delta z')$ is defined as

$$G(\rho', \delta z') = \frac{1}{2\pi} \times \int_0^{\phi_{\max}} \frac{(\rho' \cos \phi' - R_d) d\phi'}{[R_d^2 + \rho'^2 - 2R_d \rho' \cos \phi' + \delta z'^2]^{\frac{3}{2}}}. \quad (3.22)$$

Some computational speedup can be achieved by precalculating the inner integral with respect to ϕ , storing the matrix, and performing summation only for the points on the dielectric cylinder, as done for example in [30].

The maximal angle $\phi_{\max} = \arccos(R_d/\rho')$ accounts for the shading effect. As it can be seen in figure 3.4, only photons from the grey area can reach the point (in red) on the surface.

Chapter 4

Pulsed positive discharges in air at moderate pressures near a dielectric rod

We study pulsed positive discharges in air in a cylindrically symmetric setup with an electrode needle close (ca. 1 mm) above the top of a dielectric cylindrical rod of 4 mm in diameter mounted at its bottom on a grounded plate electrode. We present ICCD pictures and evaluations of experiments as well as simulations with a fluid discharge model; the simulations use cylindrical symmetry. In the experiments, a cylindrically symmetric inception cloud phase is followed by a streamer phase, with the symmetry broken. At 75-150 mbar, discharges with cylindrical symmetry are not attracted to the dielectric rod, but move away from it. The dielectric rod plays the sole role of an obstacle that shades (in the context of photoionization) a cone-shaped part of the inception cloud; the cone size is determined by the geometry of the setup. The material properties of the dielectric rod do not have a noticeable effect. This is due to the abundance of photoionization in air, which supplies a positive discharge with free electrons and allows it to propagate along the electric field lines. Using some simple field calculations, we show that field enhancement due to dielectric polarization does not play a significant role in our geometry as long as the discharge maintains its cylindrical symmetry. At higher pressures or for larger gaps between the needle and the dielectric rod, the inception cloud reaches its maximal radius within the gap between needle and rod and destabilizes there. In those cases, streamer channels are more likely to turn into a surface streamer.

This chapter is based on [A. Dubinova, et al., revised for *Plasma Sources Sci. Technol.*]. The experiments described in this chapter were performed by D. Trienekens at the Eindhoven University of Technology.

4.1 Introduction

4.1.1 Problem setting

The dynamics of a corona discharge near a dielectric is still poorly understood and lacks quantitative prediction despite multiple experimental and theoretical studies [10, 21, 51, 73]. Empirically, it is well known that discharges developing near dielectric materials are often precursors to surface discharges that damage the insulation and eventually lead to dielectric breakdown. This detrimental effect is one of the limiting factors in high voltage technology [74, 75], which necessitates improved understanding of discharges near dielectrics.

In several experiments, streamer discharges were observed to have an affinity to propagate along dielectric surfaces rather than through the background gas only [10, 22, 29, 76, 77]. This affinity for a dielectric surface was reported to depend on gas composition [29, 78–80], pressure [81], discharge gap geometry [21] and the properties of the dielectric [51, 76, 77]. It is a challenge to understand the physics of discharge interaction with dielectrics due to the interplay and competition of a large number of mechanisms and parameters. Another challenge stems from the intrinsically three-dimensional dynamics of streamer discharges near a dielectric surface, which can rarely be described with a two-dimensional model.

Setups similar to ours have been studied before, for example in [76, 77], where two types of streamers in the discharge are identified. One propagates along the surface of a dielectric rod — the surface streamer, and the other streamer propagates in the surrounding bulk air. These two streamers of the discharge exhibit different properties. The streamer in the bulk air propagates slightly slower than it does in the absence of the rod. Besides, its velocity in the presence of the rod is almost independent of the dielectric properties of the rod. The surface streamer propagates significantly faster than the streamer in air, and its velocity depends on the dielectric permittivity of the rod and the surface properties. In general, higher velocities are reported for surface discharges also in other setups [21–24].

4.1.2 Our cylindrically symmetric set-up

In the present study, we designed a cylindrically symmetric setup that can be realized both in experiments and in simulations [82]. In this manner, the cylindrically symmetric simulation can be compared quantitatively with the experiment, as long as the actual experimental discharge does not break the cylindrical symmetry.

The geometry of our setup is shown in figure 4.1. A cylindrically symmetric electrode needle with a sharp tip is placed at a short distance right above a long cylindrical dielectric rod. The rod touches or is embedded into a grounded electrode (for simulations or experiments, respectively). Experiment or simulations are performed in a large cylindrically symmetric conducting vessel that is at ground potential as well.

A positive voltage pulse (see figure 4.2) is applied to the needle electrode, and a

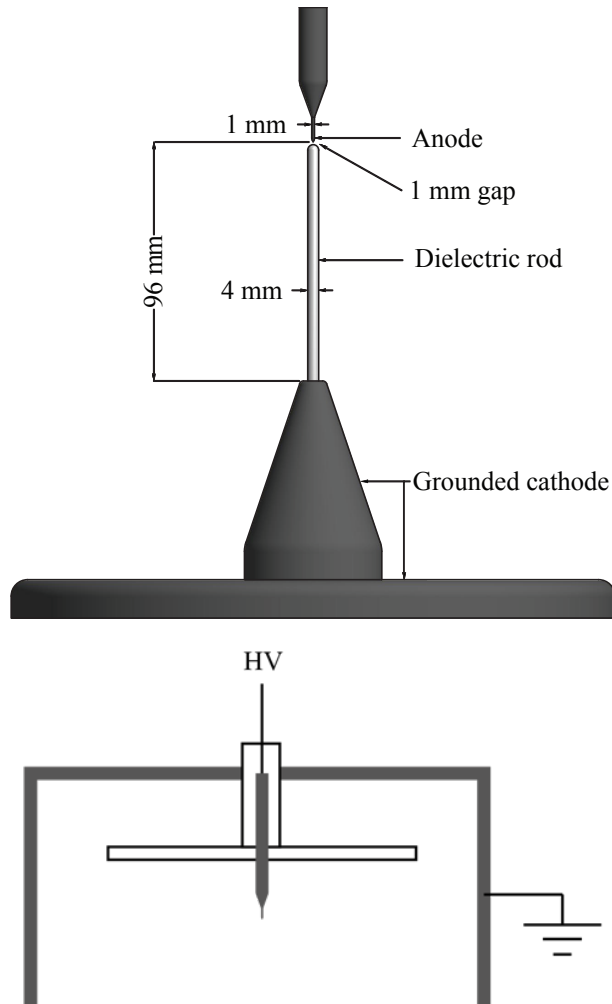


Figure 4.1: Top figure: schematic drawing of the experimental setup placed inside a grounded vessel. The dielectric rod is placed directly under the needle. Bottom figure: the top half of the vessel, with the high voltage vacuum feedthrough used in the experiments. The white parts indicate insulating material.

positive discharge emerges from the needle tip. Such a discharge in air without the dielectric rod evolves in two stages. First a cylindrically symmetric inception cloud is formed that, due to a space charge layer at its expanding surface, can grow up to a maximal radius

$$R_{\max} = U/E_k, \quad (4.1)$$

where U is the applied potential and E_k is the breakdown field, which roughly scales with inverse pressure. This cylindrically symmetric inception cloud then can destabilize and break up into separate streamer filaments that then obviously break the cylindrical symmetry. The concept of inception cloud and its breaking into streamers is described in [83, 84].

In our study, we added a dielectric rod at the axis closely below the electrode needle. We expected that the dielectric surface would attract the discharge and maintain the cylindrical symmetry. In order to achieve this goal, we made use of the Townsend scaling of the discharge size with pressure [14]. We thus chose the air pressure so low that the size of the discharge was larger than the diameter of the rod (4 mm in our setup) [16, 85]. That means that the pressure had to be lower than about 150 mbar. (However, we expect [14] that our theory would equally apply at 1 bar for a dielectric rod of 0.6 mm in diameter up to corrections from photoionization quenching. Unfortunately, such a thin rod was not available.)

When the streamer diameter was much smaller than the rod diameter (at higher air pressure), we expected beforehand, that the symmetry would be broken and the streamer would propagate only at one side of the rod, and this happened indeed. However, when the streamer diameter was much larger than the rod diameter (at lower air pressure), it did not propagate over the rod either, neither in a symmetric nor in an asymmetric way.

In this paper, we report and evaluate these experiments and the simulations with cylindrical symmetry, and offer our interpretation.

4.1.3 Positive discharges and the role of photoionization and photoemission

In our work, we study positive discharges exclusively, because they are more easily producible and controllable in experiments and they are more critical for applications. However, they are more sensitive to sources of free electrons. Positive streamers need free electrons some distance ahead in order to propagate. Among the sources of free electrons are photoionization in air and photon induced secondary electron emission from a dielectric surface (henceforth referred to as photoemission). These sources can be considered nonlocal on the timescales of interest.

Photoemission induced by low energy photons has long been considered a candidate that facilitates streamer propagation along dielectric surfaces and (ultimately) causes a breakdown [29, 86]. The nonlocal nature of photoemission plays an important role here. The required photon energy for this process is low compared to the energy needed for photoionization: typically <10 eV [29, 45, 87, 88] compared to 12 eV for

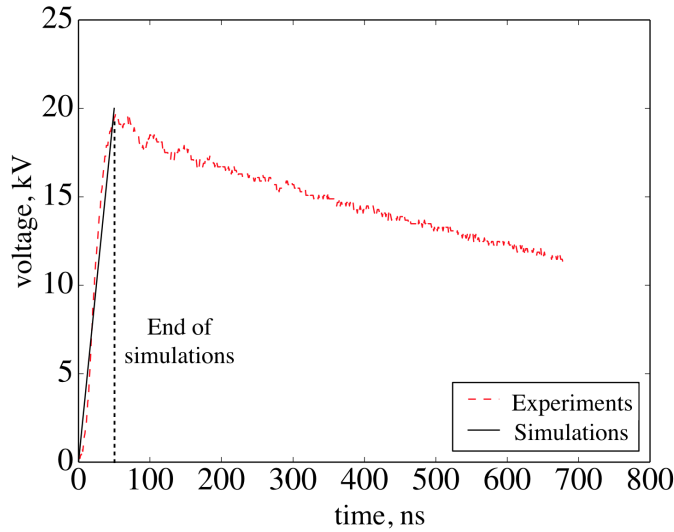


Figure 4.2: Voltage pulse. The red curve indicates the voltage pulse used in experiments. The black line shows the voltage pulse used in simulations. Discharges are simulated only on the rising slope of the voltage pulse.

photoionization. As a result, the photons are absorbed less in air and can travel larger distances, hitting and liberating electrons from a dielectric surface far away from the head of streamer discharge. A large part of our work is dedicated to studying the influence of photoemission. Other types of secondary electron emission by ion, electron or metastable atom bombardment are local phenomena within the discharge and thus of secondary importance.

Photoemission from the dielectric surface is a competitor to photoionization in air, where photons produced by excited nitrogen molecules hit oxygen molecules and liberate electrons. In pure gases like nitrogen, photoionization is suppressed, and photoemission can be the dominant source of free electrons. In the absence of photoionization, discharges are more localized in space and almost always filamentary, and our 2D cylindrical approximation is no longer justified. Therefore, in this paper we restrict ourselves to discussing discharges in air only.

Even when the 2D cylindrical approximation is valid, the setup is still complex due to the interaction of the parameters at play. As mentioned above, the pressure defines the size of the discharge both in the inception cloud phase and in the streamer phase. The photoionization length also scales inversely proportional with pressure. At the same time, the parameters of our geometry do not scale with pressure. They include the diameter of the rod and the gap between the dielectric rod and the electrode. Besides, there are properties of the dielectric rod that matter. They are the dielectric permittivity and the photoemission efficiency. All the named parameters together influence the dynamics of discharge. And each of the parameters controls a few mechanisms that compete or reinforce each other. Therefore, the task of predicting the outcome of an

experiment is challenging.

4.1.4 Order of the paper

In section 4.2 we discuss the key concepts underlying the physics of a discharge near a dielectric surface and describe the model that we developed in order to simulate discharges in the same geometry as in the experiments. Then, in section 4.3, we describe the experimental setup in detail as well as the experimental results. Section 4.4 is dedicated to the comparison of our simulations with the experiments. Section 4.5 is about the interpretation of the results, in which we try to understand how some of the parameters of the setup affect the behavior of a discharge in the presence of a dielectric rod. Finally, in section 4.7, we draw the conclusions.

4.2 Modeling and simulations

4.2.1 Physical model

We study positive streamer discharges in artificial air (80% N₂ and 20% O₂) at 75-150 mbar and 300 K by reproducing the experimental setup in cylindrical needle-to-plate geometry (see figure 4.3). A needle electrode of fixed potential and a dielectric rod are included into the simulation domain. The dielectric permittivity of the rod was set to 4 and 8 in accordance with the experiments in section 4.3. The boundaries of the domain are sufficiently far away from the area of streamer propagation and the electric field on the boundaries does not influence streamer behavior.

In the simulations we consider a single voltage pulse from the repetitive discharges of the experiments. The voltage rises from zero to 20 kV within 50 ns and then slowly decreases as shown in figure 4.2. The repetition frequency of the pulses is 1 Hz. In simulations, we study streamer development only on the rising part of the voltage pulse.

4.2.2 Fluid model

We simulate discharges with the diffusion-drift-reaction model of streamer discharges in local field approximation with cylindrical symmetry and with photoionization included. For a review of fluid models for streamer discharges, see, e.g., [89].

The equations are discretized on a static nonuniform grid. The grid is refined in the area where a discharge is expected to propagate. The size of the finest grid cells is 9 μm. Away from the area of streamer propagation grid cells quadratically increase in size up to 0.5 mm on the top and side boundaries, and 5 mm on the bottom boundary of the domain.

The transport and reactions of electrons are governed by the continuity equation for the electron density n_e

$$\frac{\partial n_e}{\partial t} = \nabla \cdot (n_e \mu_e(E) \mathbf{E} + D_e(E) \nabla n_e) + S_i + S_{ph} + S_{pe}, \quad (4.2)$$

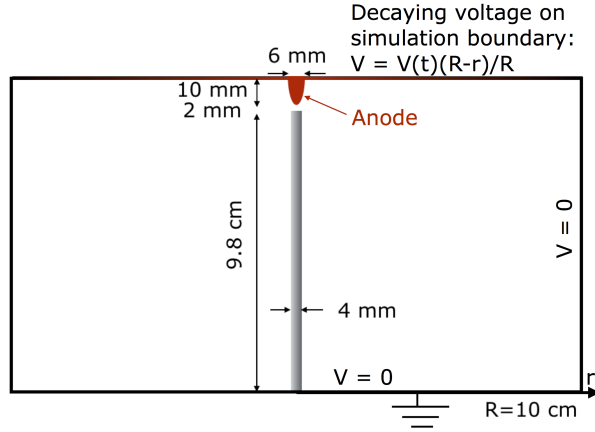


Figure 4.3: The setup of cylindrically symmetric simulation domain for the needle-to-plate setup with a dielectric rod placed directly under the needle. The color gradient on the anode illustrates that the voltage linearly drops from an applied voltage on the needle to zero on the walls.

where \mathbf{E} is the electric field and $E = |\mathbf{E}|$, S_i is the effective impact ionization source term (including 2- and 3-body attachment), S_{ph} is photoionization in air, and S_{pe} is photon induced secondary electron emission from the dielectric rod; $D_e(E)$ and $\mu_e(E)$ are field dependent electron diffusion coefficient and mobility. All transport and reaction coefficients are calculated with BOLSIG+ solver [27] using Phelps database, retrieved on July 31, 2014. To all outer boundaries Neumann boundary conditions are applied. Under the assumption that ions are immobile (they would move 0.1 mm or 1 grid cell) on the timescale of streamer development (the first 20 ns), a similar equation for positive and negative ion densities N_i^\pm is given by

$$\frac{\partial(n_i^+ - n_i^-)}{\partial t} = S_i + S_{ph} + S_{pe}. \quad (4.3)$$

We assume for simplicity that electrons, when reaching the dielectric rod, attach to the surface. In general, their attachment probability should be considered [90], but for thermal electrons it is close to 1. The electrons accumulated on the dielectric surface are treated as charge density sitting in the surface layer which is one cell wide; react. Conceptually, this approach is different from treating the surface charge as a surface boundary condition, but in practice for a fine enough grid the difference is negligible.

4.2.3 Electric field

The electric field distribution \mathbf{E} is calculated by solving Poisson's equation for the electric potential ψ :

$$\nabla(\epsilon_0\epsilon\nabla\phi) = e(n_e - n_i^+ + n_i^-), \quad (4.4)$$

$$\mathbf{E} = -\nabla\psi, \quad (4.5)$$

where ϵ_0 is the permittivity of free space, ϵ is the relative dielectric permittivity of the dielectric rod, and e is the elementary charge.

The Ghost Fluid Method was used to accurately capture the boundary conditions on the electrode and dielectric curved interfaces based on [56, 57]. Conceptually, any shape of an electrode and a dielectric can be rendered with this method. For example, the rod is parameterized as a cylinder with a flat top. The needle electrode in our simulations was parameterized as an ellipsoid of revolution with a given radius of curvature and a length. Although, the shape of the needle electrode differs from the one used in experiments, it essentially does not influence the discharge propagation. The only purpose of the needle in our experiments is to launch a discharge in an inhomogeneous field, but once the discharge has started, its plasma screens the electrode shape and creates its own self-consistent electric field enhancement at its surface. Therefore, we chose the ellipsoidal shape for the sake of simplicity.

Dirichlet boundary conditions are used in the radial direction and on the sides of the simulation domain. The bottom and the sides of the simulation domain are grounded. Away from the needle in the radial direction the voltage decreases linearly and reaches zero on the sides of the simulation domain (see figure 4.3). This inhomogeneous Dirichlet boundary condition with the artificial linear voltage drop at the top of the vessel turns out to be convenient in simulations, and the exact shape of the radial drop has not significant influence on the streamer discharge, because the needle tip is far away from the top of the vessel.

In our model, the transport equations and the Poisson equation were discretized using a method of finite volumes. The spatial discretization is based on an upwind-biased scheme with the flux limited by the Koren limiter function [91]. This conserves mass and guarantees monotone solutions. The resulting sparse matrix for the Poisson equation was inverted with the numerical package MUMPS [65].

In the coupling of the Poisson equation with the transport equations, the electric field is updated at every time step and its values are passed to the transport equations. We solve the system of the coupled partial differential equations with an explicit time integration scheme, namely a two-stage Runge-Kutta method, which is second-order accurate. This is in line with the accuracy of the spatial discretization.

The time step δt varies and it is restricted by the Courant-Friedrichs-Levy (CFL) criterion, dielectric relaxation and ionization time scales. The time step is chosen in

The implementation of the spatial discretization of the transport equations and their coupling to the Poisson equation were granted by W. Hundsdorfer.

accordance with [92]. The CFL condition with the advection and diffusion parts combined is necessary for convergence of the equation 4.3, which we solve numerically by the method of finite volumes. It reads

$$\delta t \leq 0.5 \times \min \left[\frac{\mu_e E_r}{h_r} + \frac{\mu_e E_z}{h_z} + \frac{D_e}{h_r^2} + \frac{D_e}{h_z^2} \right]^{-1}, \quad (4.6)$$

where $E_{r,z}$ are the radial and the axial components of the electric field, $h_{r,z}$ are the sizes of the radial and axial grid cells. The dielectric relaxation time restriction

$$\delta t \leq 0.5 \frac{\epsilon_0}{e \mu_e \max(n_e)} \quad (4.7)$$

guarantees that the change of the electric field due to the electric current at every time step is no larger than the electric field. Finally, the ionization time step restriction $\delta t < 0.1/\max(\alpha \mu_e E)$ is used to accurately resolve the growth of the electron density, in particular in the streamer head. In the simulations the time step varied from about 10^{-13} s to 10^{-12} s.

4.2.4 Photoionization and photoemission

Positive streamer-like discharges need a source of free electrons ahead of them in order to propagate. In the bulk gas this source can be photoionization S_{ph} in equations (4.2) and (4.3) or background ionization (see figure 4.4). In our experiments, the effect of the background ionization is negligible (see section 4.2.5). The photoionization in air is possible due to the photons produced in air by molecular nitrogen. They are VUV photons of the 13-14 eV energy range (98-102.5 nm). Oxygen molecules absorb this radiation and produce free electrons [93].

We use the photoionization model developed for air in [94]. In that model, the photoionization source term S_{ph} is approximated with a weighted sum of the solutions to elliptic equations, as follows

$$S_{\text{ph}} = \frac{p_q}{p + p_q} (A_1 S_{\text{ph},1} + A_2 S_{\text{ph},2}), \quad (4.8)$$

$$(\nabla^2 - \lambda_{1,2}^2) S_{\text{ph},1,2} = -|S_i|, \quad (4.9)$$

where S_i is impact ionization source term from equation (4.2), $\lambda_{1,2}$ and $A_{1,2}$ are coefficients chosen to fit the experimental data and taken from [94]. With the print errors corrected, the coefficients read $A_1 = 6 \cdot 10^{-5} \text{ Torr}^{-2} \text{ cm}^{-2}$, $A_2 = 3.55 \cdot 10^{-6} \text{ Torr}^{-2} \text{ cm}^{-2}$, $\lambda_1 = 0.059 \text{ Torr}^{-1} \text{ cm}^{-1}$ and $\lambda_2 = 0.01 \text{ Torr}^{-1} \text{ cm}^{-1}$. The factor $p_q/(p + p_q)$ represents the effect of collisional quenching, where p and $p_q = 60 \text{ Torr}$ are pressure and the quenching pressure, respectively. The parameters $\lambda_{1,2}$ (proportional to the oxygen content and pressure) define the characteristic length scale of photoionization or photoionization length. In ambient air the photoionization length is about 1.3 mm, and at pressures 75-150 mbar, it ranges from 8.7 mm to 17.3 mm.

In our model, photons and electrons produced by photoionization can be created only outside the dielectric rod and the electrode. After equations (4.9) are solved everywhere inside the simulation domain, the solutions are set to zero inside the dielectric and inside the electrode. This means that photoionization in some areas is suppressed by shading.

We include photoemission from the dielectric surface S_{pe} in equation (4.2). At every time step we calculate the flux of photons onto every point on the dielectric surface as described in section 3.5 of chapter 3. The flux of photoelectrons from the dielectric surface is equal to the flux of photons multiplied by the photoemission yield γ . We assume that the photoemission yield is in the range of 0 to 1, and we study the sensitivity of the discharge to its actual value. The emitted electrons are placed just outside the surface. Essentially, they become bulk electrons; the positive ions stay immobile on the surface.

4.2.5 Initial conditions

When working with pulsed discharges of a certain repetition frequency, it is important to estimate the density of free electrons (and in general other species) remaining from the previous discharges, as they can influence the propagation of positive streamers. Approximating the weakly curved front by a planar front and assuming that the electric field in the non-ionized region just ahead of the discharge region does not change in time, in zero-dimensional configuration we can estimate the level of the ionization remaining in the repetitive discharge, like in [95]. We set the maximal electric field in the simulated positive discharge to 20 kV/cm at 150 mbar (which would correspond to 133 kV/cm at 1 bar according to the similarity laws). The electron density where the electric field is maximal scales to $9 \times 10^{11} \text{ cm}^{-3}$ at 150 mbar [85], and we used this value as the initial condition for our zero-dimensional analysis in the same manner as in [95]. We initialize the densities of the positive ions N_2^+ and O_2^+ such that the plasma is electrically neutral $n_e(0) = n_{\text{N}_2^+}(0) + n_{\text{O}_2^+}(0)$. We keep the initial ratio as $n_{\text{N}_2^+}(0) : n_{\text{O}_2^+}(0) = n_{\text{N}_2}(0) : n_{\text{O}_2}(0)$. The initial densities of all other ions, excited species and ground-state neutrals (except N_2 and O_2) are assumed to be zero. We performed the estimations with ZDPlasKin software [96]. Figure 4.4 shows the results, and we conclude that the residual electron density in air discharges at 150 mbar with repetition frequency of 1 Hz is negligible.

We launch a discharge by placing an electrically neutral plasma seed on the axis of the domain at the electrode tip. The maximal electron (and ion) density is 10^7 cm^{-3} . The decay length of the Gaussian seed is 1 mm, which is smaller than the typical discharge width at 75-150 mbar but comparable with the gap size. The centre of the seed coincides with the electrode tip. This seed was chosen to facilitate the start of the streamer propagation and the chosen parameters do not influence the discharge development. Taking into account the voltage rise time (see figure 4.2), the seed electrons create a conductive patch around the electrode tip before the voltage becomes high enough and a discharge incepts. After its inception the discharge propagates predomi-

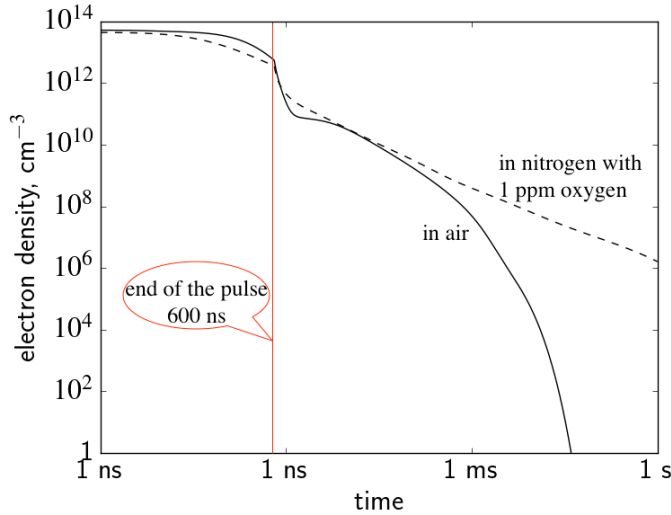


Figure 4.4: The electron density calculated in air and in nitrogen with 1 ppm oxygen as a function of time at 150 mbar (on the logarithmic scale). The pulse duration is 600 ns, the initial electron density is $9 \times 10^{11} \text{ cm}^{-3}$, the maximum electric field at the streamer tip is 20 kV/cm, and the electric field in the streamer channel is 0.75 kV/cm.

nantly due to photoionization.

4.3 Experiments

The stainless steel vessel in our setup is filled with ambient air at pressures between 75-150 mbar. Inside the vessel, the needle anode is placed approximately 18 cm above a grounded cathode plane. The (grounded) conical holder containing the dielectric rod is placed in the discharge gap, effectively reducing the gap size to 96 mm. The rod is placed directly under the needle, with a gap of approximately 1 mm between the needle and the (rounded) top of the dielectric rod (see figure 4.1). The rods used in the experiments were 4 mm in diameter and protrude approximately 95 mm from the holder. We used two different rods with a (relative) dielectric permittivity ϵ of ~ 4 (unfilled epoxy resin) and ~ 8 (epoxy resin with TiO_2 filler).

We apply a +19 kV pulse at a repetition frequency of 1 Hz to the needle in order to generate streamers. Streamer discharges are imaged using a LaVision PicoStar HR12 stroboscopic ICCD camera, which allows stroboscopic gating at 50 MHz. This means multiple intensifier gates, 20 ns apart, can be achieved within a single exposure (and thus a single discharge). By supplying a train of pulses at 50 MHz timed to coincide with the start of the discharge to the intensifier, we can study streamer propagation, through stroboscopic imaging, both temporally as well as spatially resolved. This technique is based on the fact that the streamer head (in air) only emits light for a very short time, i.e. effectively only the streamer head emits light [16, 97, 98]. This method was

explained in more detail before [99]. Figure 4.5a shows an example of a stroboscopic image at 150 mbar with the epoxy resin rod in the discharge gap. Due to the stroboscopic gating of the intensifier, the image shows maxima and minima in intensity. A semi-transparent white region indicates the area over which this intensity (shown in figure 4.5b) is measured. The measured intensity is filtered using a low pass filter and maxima and minima are detected automatically using a script. From the positions of the maxima and minima the velocity is determined. The result is shown in figure 4.5c. We typically distinguish between three distinctive phases. Initially, the inception cloud rapidly expands (1), until it reaches its maximum size and stagnates (2). After this, the inception cloud breaks up into separate streamer channels that propagate at a rather steady velocity (3). This discharge behavior is similar to the behavior observed by Chen et al. [84] for experiments in nitrogen with a 20% admixture of oxygen. It should be noted that the stagnation of the inception cloud may cause maxima and minima in the measured intensity to overlap partially or fully, making their identification impossible. Therefore, the presented velocity in the stagnation phase may in fact be even lower.

4.3.1 Discharge morphology

Experiments were performed at 75 and 150 mbar ambient air. Figure 4.6 shows an overview of the typical discharge morphologies observed in these experiments. No surface discharges were observed under these conditions. Discharges at 75 mbar (see figures 4.6a-c) all showed a similar behavior. Initially, the discharge rapidly expands before eventually stagnating. In all of our experiments at 75 mbar a negative streamer propagating upwards from the grounded holder connects with the inception cloud before the inception cloud breaks up into separate channels. The inception cloud was observed to grow to ~ 55 -60 mm in all cases at 75 mbar. This is somewhat lower than the theoretical maximum value of 83 mm, calculated using equation (4.1) [84].

No differences were observed between the discharge around the unfilled epoxy resin rod (figure 4.6a: $\epsilon = 4$) and around the TiO_2 filled rod (figure 4.6b: $\epsilon = 8$). Comparing these cases with the case without the rod, we observe that the rod partially blocks the inception cloud. The rod appears to block a roughly conical section of the inception cloud, which is also observed in simulations (see figure 4.10). The discharge avoids this conical region and consequently has to travel further before it can reach the cathode. Most likely, this longer path causes the discharges to bridge the discharge gap more slowly when a rod is present.

For 150 mbar (figure 4.6d-f) we also observe a rapidly expanding inception cloud that eventually stagnates for both with and without a rod. The radius of the inception cloud is roughly halved to ~ 25 -30 mm (compared to 75 mbar). This value is again somewhat lower than the theoretical maximum (see equation (4.1)), and the scaling with pressure is maintained [84]. After stagnating, the inception cloud breaks up into separate channels. No differences were observed between the discharges around the two rods. However, without the rod the streamer channels emerging from the inception cloud are significantly thinner and less numerous. It was also observed that these

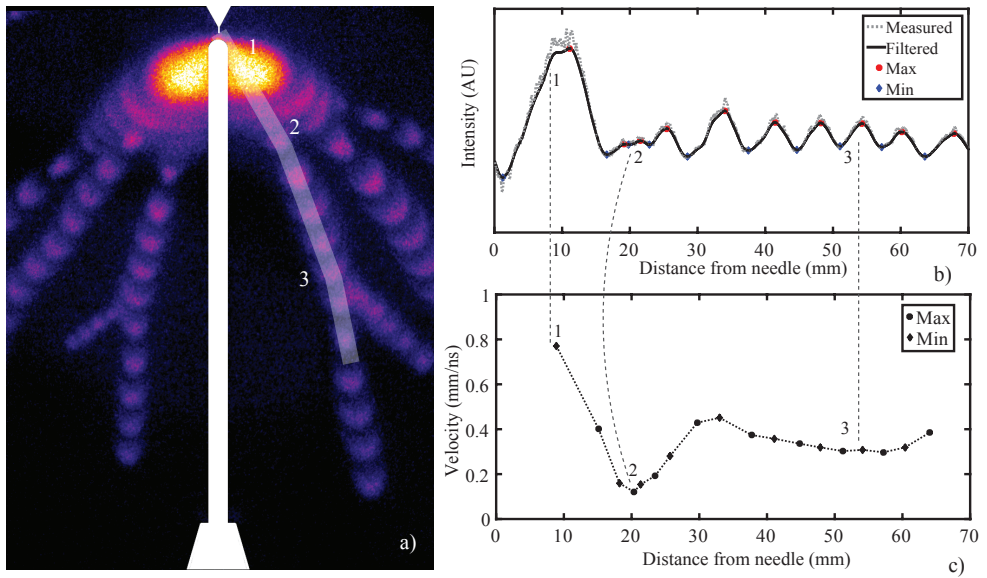


Figure 4.5: Stroboscopic image of a discharge at 150 mbar with the epoxy resin rod in the discharge gap (a) and the resulting intensity profile (b) and velocity (c). The semi-transparent white region in the stroboscopic image indicates the region where the intensity profile is measured. From this profile, the velocity is calculated. Three distinctive phases can be distinguished: rapid expansion of the inception cloud (1), stagnation of the inception cloud (2), and streamer propagation at steady velocity (3).

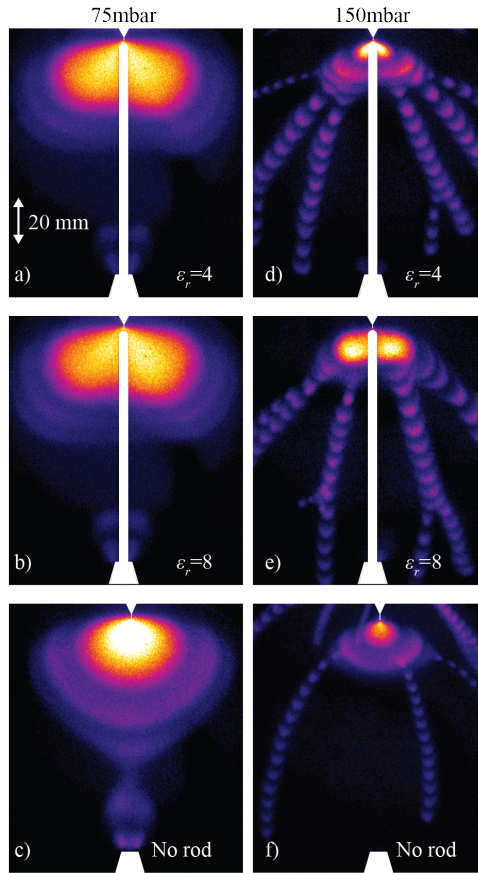


Figure 4.6: Typical stroboscopic images obtained at 75 mbar a)-c) and 150 mbar d)-f) with the epoxy resin rod ($\epsilon = 4$), the TiO₂ filled rod ($\epsilon = 8$), and without rod.

streamer channels often emerge later or not at all. The absence of a dielectric rod could cause the inception cloud to maintain its spherical shape and prevent the emerge of streamers while the rod breaks the semispherical symmetry. Some streamer channels can be observed that originate from the high voltage feedthrough above the needle position (see upper part of figure 4.6f). It could be possible that these channels trigger the breaking up of the inception cloud. To the best of our knowledge, the propagation velocity of the channels is not influenced by the channels originating from the HV feedthrough. Note that the filaments emerging from the inception cloud cannot be simulated using our 2D model.

4.3.2 The role of pressure

To investigate the role of pressure, we repeated the experiment for a pressure of 600 mbar and otherwise identical conditions. Due to the increased pressure at unchanged voltage, inception of the discharge was not always observed. For the cases where inception was

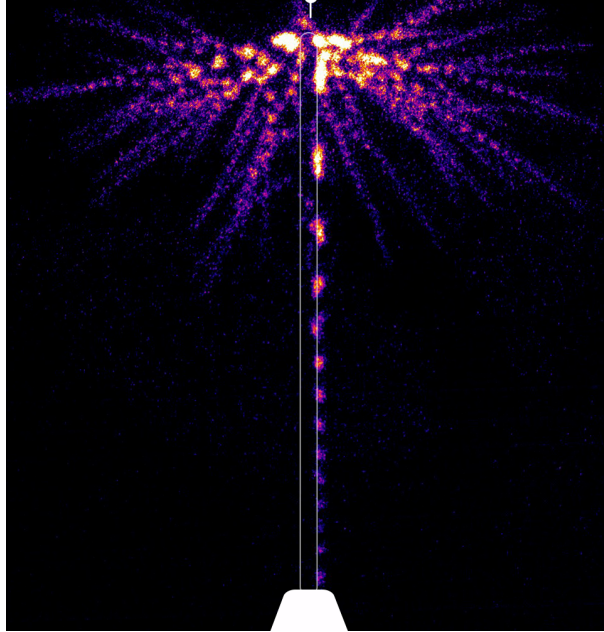


Figure 4.7: Typical stroboscopic image of a discharge at 600 mbar in air for the rod with TiO_2 filler, $\epsilon = 8$. A positive surface streamer can be observed and its velocity is clearly much larger than the velocity of the bulk streamers.

observed, we always observed a surface streamer. Figure 4.7 shows a typical stroboscopic image from this experiment. A positive surface streamer can clearly be distinguished here. Moreover, a clear inception cloud cannot be observed in this image, possibly due to its reduced size. The close proximity of many discharge filaments also makes it hard to identify the inception cloud in the initial stage of the discharge. As the inception cloud now fits into the gap between the electrode and the rod, the discharge breaks up into filaments within the gap, and streamers can reach the rod surface, see figure 4.7. We will elaborate on this in section 4.5.

The close proximity of many discharge filaments also makes it hard to identify the inception cloud in the initial stage of the discharge. As the inception cloud now fits into the gap between the electrode and the rod, the discharge breaks up into filaments within the gap, and streamers can reach the rod surface, see figure 4.7. We will elaborate on this in section 4.5. As can be seen in figure 4.7, the velocity of the surface streamers is clearly larger than that of the bulk gas streamers. This finding in similar setups has been observed before [22, 24, 76, 77]. The discussion on this is beyond the scope of this paper as we focus on the affinity of discharges for dielectric surfaces.

4.4 Comparison of simulations with experiments

Simulations in section 4.2 and experiments in section 4.3 are compared in figures 4.8 and 4.8c where we show the stroboscopically integrated light emission of a positive discharge.

In simulations, we assume that light emission is proportional to impact ionization $n_e \alpha$ (α is impact ionization coefficient) and we integrate it over time intervals of 10 ns taking the exponential quenching into account for the stroboscopic effect and we also integrate it in the viewing direction across the area of the display. The quenching rates were taken from [97, 100, 101]. The limited number of grid cells ultimately restricts how long we can simulate discharge propagation, and therefore the elapsed time is only about one stroboscopic period.

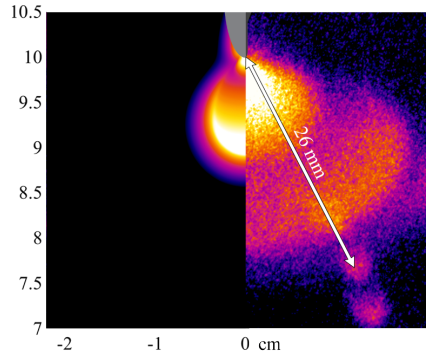
First, we compare the results without the dielectric rod to have a reference case. Then we compare the results with a dielectric rod in air at 150 and 75 mbar. In all the cases at 75-150 mbar no surface streamers were observed. Both in experiments and simulations, no difference has been observed when the rod with a relative permittivity of 4 was replaced with the rod with a relative permittivity of 8. It seems that the relative permittivity, at least in this range, does not play a significant role in determining the discharge morphology. We will discuss the role of field enhancement in more detail in subsection 4.5.1

Figure 4.9 shows the calculated and measured inception cloud discharge velocity as a function of distance from the needle. Experimental values were obtained using the method described by figure 4.5. In simulations, the velocities were calculated by taking the time derivative of the position of the maximum of the electric field.

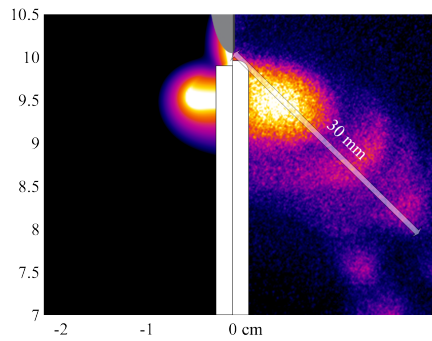
Experimentally, no differences were observed between the velocities measured with the unfilled epoxy resin rod ($\epsilon = 4$), the TiO_2 -filled rod ($\epsilon = 8$) and without a dielectric rod. For 75 mbar, inception cloud velocities of up to ~ 2 mm/ns were found for all cases. This velocity decreases to ~ 0.5 mm/ns when the inception cloud stagnates. As was mentioned in section 4.3.1 a negative streamer, originating from the grounded holder, causes the discharge to bridge the gap before the inception cloud breaks up into separate streamer channels.

For 150 mbar, a similar trend was observed, albeit with a smaller inception cloud and lower velocities. Indeed, for the same applied voltage and the same gap, we get a lower E/N ratio which translates into smaller velocities. Figure 4.5 shows that the differences between the three cases are again very small. Our results show a typical velocity for the inception cloud expansion of ~ 1 mm/ns. This velocity decreases to ~ 0.2 mm/ns before the inception cloud breaks up and the streamers propagate at ~ 0.4 mm/ns. Note that this part is omitted from figure 4.9 because we focus on the cylindrically symmetric part of the discharge here.

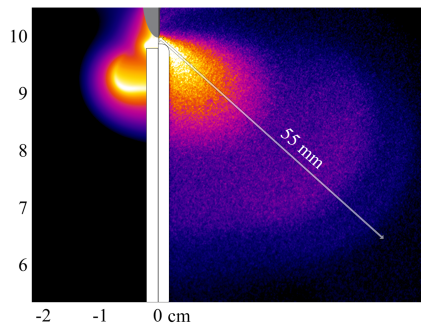
One would expect the velocity of the streamers emerging from the inception cloud without a rod to be lower than those reported for both rods, as we observed these streamers to be significantly thinner (see figures 4.6d-f), but we do not observe such a difference.



(a)



(b)



(c)

Figure 4.8: Light emission of a positive streamer discharge in air simulated (the left half) and observed experimentally with the stroboscopic effect (the right half). We show three cases: (a) at 150 mbar in the absence of the dielectric rod, (b) at 150 mbar with the dielectric rod, (c) at 75 mbar with the dielectric rod. The arrow indicates the observed inception cloud size. The distance between the maxima of the light emission corresponds to 10 ns of the simulated discharge propagation, and 20 ns of discharge propagation in the experiments (the stroboscopic ICCD camera operates at 50 MHz with a 10 ns on and 10 ns off time). In the simulations, the elapsed time is about one stroboscopic period. The measured and calculated velocities of the discharge are given in figure 4.9.

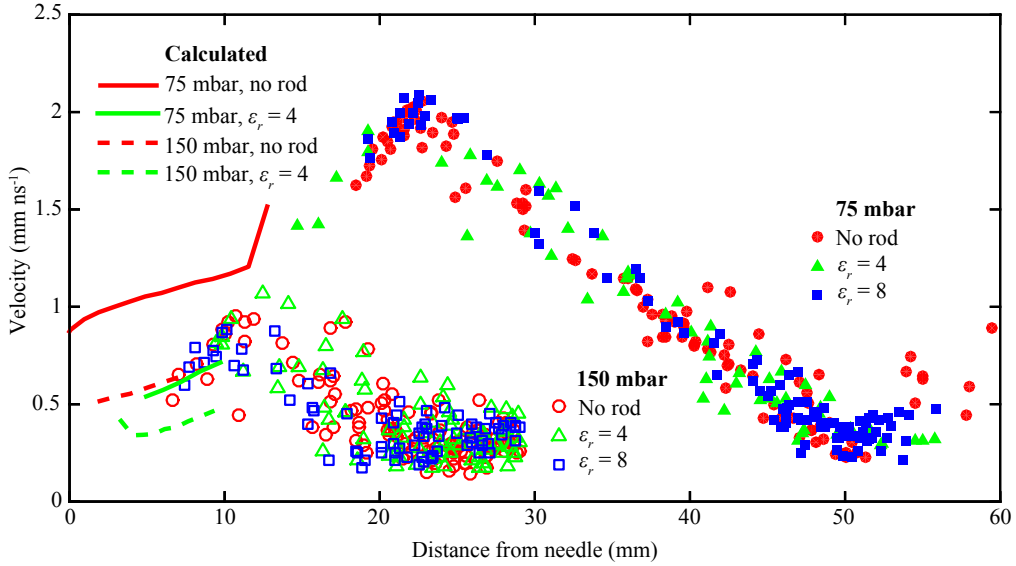


Figure 4.9: Velocity of the discharge before destabilization into filaments (i.e. in the inception cloud phase) as a function of distance from the needle anode for 75 and 150 mbar, for two different rods and without a rod. Numerically calculated values are also shown. The theoretical maximal radii of the inception cloud are 42 mm at 150 mbar and 84 mm at 75 mbar, according to equation (4.1).

The velocities we find here are similar to those reported by Chen et al. [84]. They measured velocities for 100 mbar, 20 kV in a point-plane gap in otherwise similar conditions. Initially, they observed a relatively high velocity (~ 1 mm/ns) and stagnation of this inception cloud (~ 0.09 mm/ns) before it breaks up into separate streamer channels and the velocity increases again (~ 0.36 mm/ns). These velocities are comparable to the velocities we find. It should be noted however that the velocity decrease in [84] is more severe (down to ~ 0.09 mm/ns). Possibly, the stagnation of the inception cloud is more severe in our case as well, but the close proximity of the maxima in intensity in the stroboscopic image do not allow us to resolve this.

Numerically, we get similar results. For 75 mbar and an $\epsilon = 4$ dielectric rod, the velocity was found to increase from 0.5 to 0.7 mm/ns in the first 10 mm of the discharge. Although somewhat lower than the experimentally determined velocity, the positive trend in the velocity suggests that our simulations are consistent with our experiments. For 150 mbar and an $\epsilon = 4$ dielectric rod, the velocity increases from 0.3 to 0.5 mm/ns in the same stage. These results are in accordance with the experiments in the inception phase of the discharge and with the observations of the bulk discharge in air in [76, 77]. The velocities slightly increase as the discharge propagates due to the rising voltage.

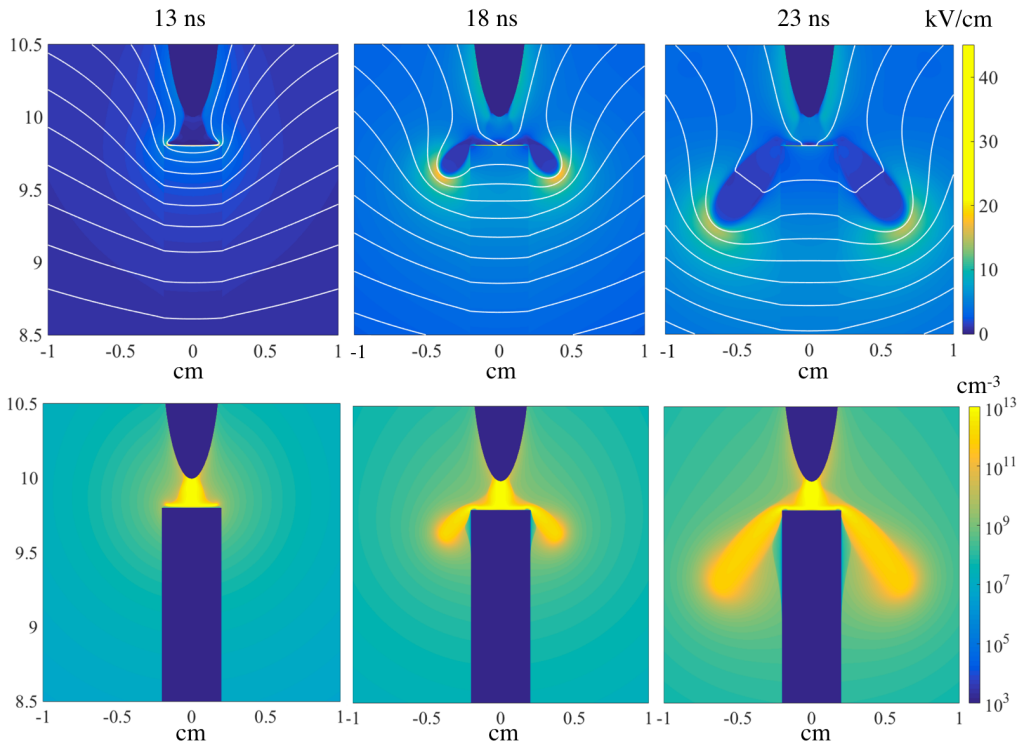


Figure 4.10: Simulation results zoomed-in into the area of discharge development (see figure 4.3) in 150 mbar air after 13 ns, 18 ns, and 23 ns from the start of a pulse for $\epsilon = 4$ and $\gamma = 1$. Despite the large value of the photoelectron yield to maximize the attraction to the rod, but it is still not seen. Upper panel: the absolute value of the electric field in the discharge and the equipotential lines. Lower panel: the electron density on a logarithmic scale.

4.5 Discussion

Contrary to our expectations, we have not observed cylindrically symmetric positive discharges propagating on the surface of a dielectric, neither experimentally nor numerically. Figures 4.6 and 4.10 clearly show that the inception cloud avoids the area near the rod. In the simulations, we varied the photoemission yield γ from 10^{-7} to 1 in order to increase the effect of the dielectric surface. We expected that by supplying more free electrons from the dielectric surface we would be able to increase the affinity of the discharge for the surface. However, the increase of the photoemission yield by seven orders of magnitude was still not enough to make the discharge propagate along the dielectric rod.

We attribute this behavior to the abundance of photoionization in air. In the inception cloud phase, photoionization in air will provide the discharge with an abundance of free electrons. The dielectric rod partially blocks the expansion of the inception cloud because it blocks photoionization, but it hardly influences its propagation otherwise. As was discussed in 4.3.1, a conical region of the (semi)spherical expanding shell is blocked. Despite the altered shape of the inception cloud, our experimental results suggest that the breaking up of the inception cloud into separate channels takes place at roughly the same distance from the needle as would be the case without the dielectric rod (see figure 4.6). Any additional free electrons generated by photoemission will not cause the discharge to deviate from its spherical shape. Equation (4.1) gives a theoretical maximum radius of the inception cloud by assuming the inception cloud to be an ideally conducting sphere [84]. Using $U = 20$ kV as the applied voltage, we find that the experimentally measured inception cloud size is about $\sim 60 - 70\%$ of its theoretical maximum both for 75 mbar and 150 mbar, when the Townsend scaling of the breakdown field E_k with pressure is used. In the work by Chen et al. an actual size of $\sim 90\%$ of the theoretical maximum size was found. Therefore, this equation provides an upper bound and a good estimate for the inception cloud size.

We expect the rod to roughly block a conical region with a solid angle of $\Omega = 2\pi(1 - \cos 2\theta)$, where θ is the angle between the line from the electrode tip to the tangent to the rod and the vertical axis if the inception cloud is bigger than the gap between the electrode and the rod. This is depicted in figure 4.11a. The presence of the shaded conical region can be explained first by the fact that the dielectric is opaque for the photons providing photoionization. However, the region is larger than what is occupied by the dielectric rod. This can be explained by the electrons produced due to photoionization just outside of the dielectric rod have hardly any space to multiply and create an avalanche that could contribute to the streamer formation. Those electrons are more likely to attach to the surface than to end up in the streamer head (see figure 4.10 for the potential lines).

As the pressure is increased while the voltage is kept, the inception cloud decreases. If it is still bigger than the rod, the horizontal distance between the inner edge of the cone and the rod will decrease. Additionally, the distance to the grounded cathode will increase. Figure 4.11b and c show a schematic representation of this process for

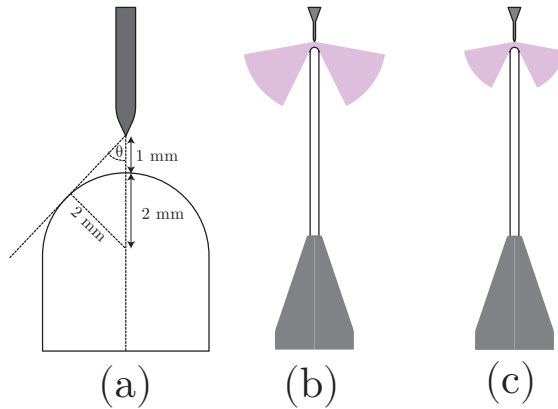


Figure 4.11: Schematic drawing showing the geometrical angle θ between the inception cloud and the vertical axis (a), and the point where the inception cloud breaks up for low (b) and high (c) pressure.

lower and higher pressure, respectively. Figure 4.12 shows theoretical values for the maximal inception cloud radius, the horizontal distance of the inner cone edge to the rod and its vertical distance to the cathode. This figure demonstrates that the reduced size of the inception cloud at higher pressure will cause filaments to emerge from the inception cloud closer to the rod and further away from the cathode. This could make it easier for surface discharges to appear, as the proximity of the filaments to the rod may cause them to encounter it. Filaments have been observed to propagate along dielectric surfaces upon encountering them before [10, 21, 22, 29, 76, 77, 81].

To test the hypothesis that a dielectric surface will simply block part of the inception cloud, we compare two PMMA ($\epsilon \approx 3.6$) rods with diameters of 6 and 10 mm that were placed at varying distances from the needle. The rods had a flat top and were placed in a grounded holder at a constant distance of approximately 100 mm from the needle. The same voltage pulse shape (see figure 4.2) was used. We measured the geometrical angle θ indicated in figure 4.11a and compared this to the angle φ the discharge makes with the vertical axis. Experiments were performed at 75 mbar. An example of such a measurement is shown in figure 4.13. Here, the green line determines the geometrical angle θ and the black line determines φ . We define φ as the angle between the line from the electrode tip to the center of curvature of the discharge front and the vertical axis. Because we image the discharge stroboscopically, we generally have a few reference points to draw this line, as can be seen in figure 4.13. Although φ is determined from a 2D-projection of emission from a 3D phenomenon, we expect that the error using this method is still within reasonable bounds. Nevertheless, it should be taken into account that φ could be consequently underestimated using this method. Both rods were placed at three different distances from the needle in order to compare six different values for θ . Figure 4.14 shows the observed discharge angle φ as a function of the geometrical angle θ . As can be seen, φ clearly increases with θ , as was expected. We find that the

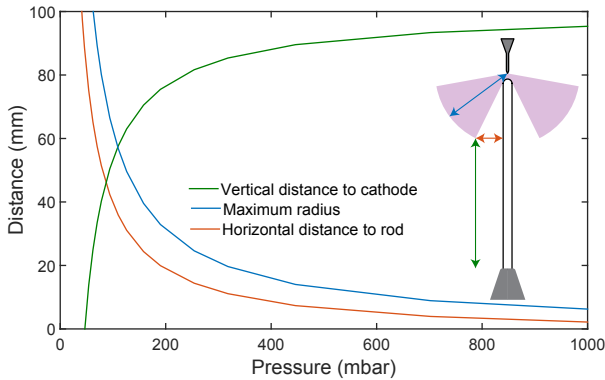


Figure 4.12: The theoretical size of the inception cloud according to equation 4.1 (blue), and the radial distance of the cloud cone to the rod (red) and the axial distance of the cloud cone to the cathode (green) at the point where the inception cloud breaks up.

discharge propagates at an angle that is somewhat larger than θ , except for large values of θ .

To analyze this behavior, we investigated the inception cloud size at the moment it reaches the top of the rod. The dielectric rod will cause a field enhancement between the discharge and the rod. This field enhancement causes the inception cloud to deviate slightly from its spherical shape (see figure 4.15a). Due to the deviation in the inception cloud shape, it is possible that the discharge will propagate at a slightly larger angle φ . The deviation in inception cloud shape is shown in figure 4.15b. For radii much larger than the rod radius, we expect the discharge to propagate at $\varphi < \theta$ because the background electric field points mostly downwards (towards the cathode), rather than radially outwards.

As was mentioned before, we expect to observe more surface discharges when the inception cloud breaks up close to the rod. As figure 4.12 shows, high pressure is expected to increase the likeliness of surface discharges. The vertical position of the rod with respect to the needle was expected to be important as well, as placing the rod further from the needle decreases the geometrical angle θ .

As a result, the inception cloud will break up closer to the rod, and the discharge is more likely to propagate along the dielectric surface. Our results suggest that this hypothesis is correct: we only observe surface discharges for relatively high pressure and small θ . Figure 4.16 shows an example of such a surface discharge at 400 mbar. It is hard to distinguish an inception cloud in this case. Equation 4.1 predicts a maximum radius of ~ 1.5 mm and we have observed actual radii up to $\sim 0.7R_{\max}$ before. This is smaller than the gap (~ 20 mm) in this case, meaning that the inception cloud breaks up before the discharge reaches the rod. It is important to note that the broken symmetry implies that our 2D cylindrical simulation model cannot be used to study these surface discharges.

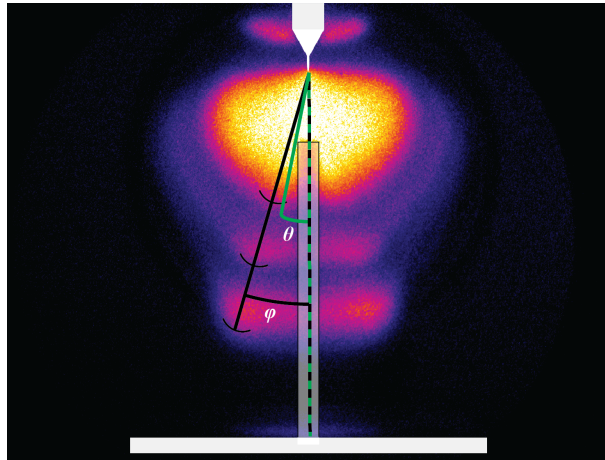


Figure 4.13: Stroboscopic image of the discharge at 75 mbar with the 6 mm rod, indicating how the geometrical angle θ (green) and the discharge angle φ (black) are determined.

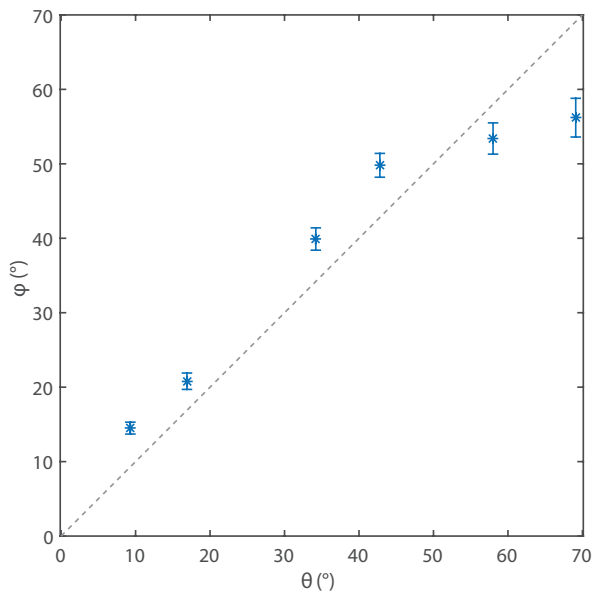


Figure 4.14: Discharge angle φ as a function of the geometrical angle θ . The dotted line shows $\varphi = \theta$, which would be the case if discharge propagation would be governed by the geometrical angle only.

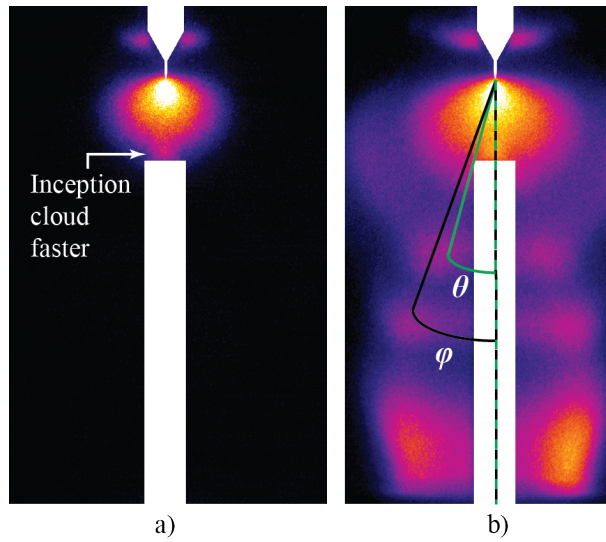


Figure 4.15: When the rod is placed further from the needle, the inception cloud shape deviates from its spherical shape due to the field enhancement caused by the dielectric (a), only for this larger gap. As a result, the discharge propagates at an angle larger than θ (b).

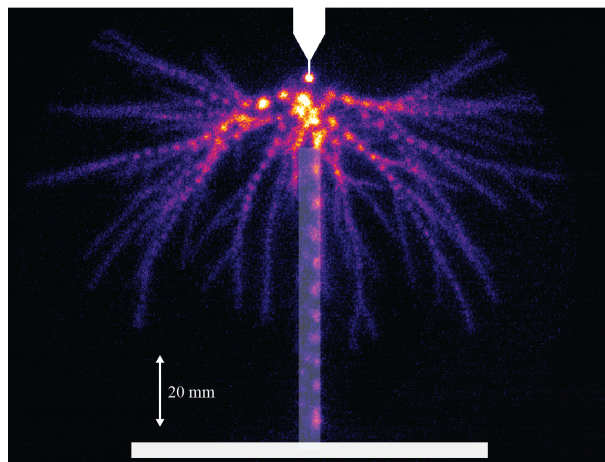


Figure 4.16: Example of a surface discharge at 400 mbar with the 6 mm PMMA rod placed in the discharge gap.

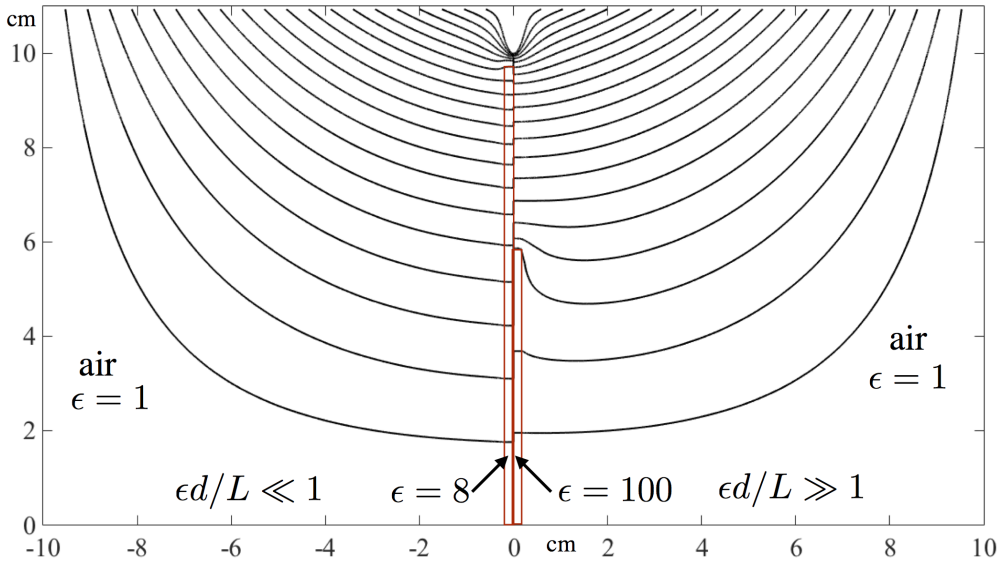


Figure 4.17: Equipotential lines in the setup for two cases $\epsilon d/L \ll 1$ and $\epsilon d/L \gg 1$. In the left half of the figure, $\epsilon = 8$, $d = 2$ mm, and $L = 98$ mm, as used in our experiments and simulations. In the right half of the figure, $\epsilon = 100$, $d = 42$ mm, and $L = 58$ mm. Clearly, in the latter case a discharge is more predisposed to be attracted by the dielectric rod.

4.5.1 Field enhancement in the absence of a discharge: geometrical effect

Commonly discharges follow the electric fields lines, and therefore let us study the equipotential lines in our setup. In figure 4.17, we compare the case with $\epsilon = 8$, the gap between the dielectric rod and the electrode $d = 2$ mm, the length of the rod $L = 98$ mm, and the case with $\epsilon = 100$, $d = 42$ mm, and $L = 58$ mm. It is clear that the potential lines look drastically different. In the latter case a discharge will be more predisposed to be attracted to the dielectric rod as the electric field points to the sides of the rod.

To understand the role that the geometric parameters play in modifying the background field, let us consider a simple model. In a plate-to-plate electrode geometry with a potential difference ΔV a part of the gap of length L is filled by a dielectric with the dielectric constant ϵ and the other part is an air gap of distance d . The electric field inside the dielectric E_ϵ can be easily calculated and is given by

$$E_\epsilon = \frac{\Delta V}{L} \frac{1}{1 + \epsilon d/L}. \quad (4.10)$$

If $\epsilon d/L \ll 1$, the field inside the dielectric is essentially independent of ϵ . If $\epsilon d/L \gg 1$, then E_ϵ is small and the potential drop is compressed in the air gap and the electric field

there is large. Based on this simple model, we take the ratio $\epsilon d/L \ll 1$ as an indicator of the electric field around the dielectric.

When $\epsilon d/L \ll 1$, the dielectric hardly modifies the background electric field, which is true for the case on the left side of figure 4.17, whereas when $\epsilon d/L \gg 1$, the electric field is severely perturbed. Essentially, in our parameter regime when a dielectric rod fills almost all the gap between the needle and the cathode and the dielectric constant of the rod is not very high, the field enhancement next to the dielectric rod is initially negligible.

4.5.2 Field enhancement in the presence of a discharge

In the presence of a discharge, the local electric field is modified by the space charge in the streamer. To understand the forces acting on the cylindrical streamer let us introduce a simple approximation. We approximate a cylindrical streamer head with its net electric charge as a perfectly conductive ring at a fixed potential $U \neq 0$. We assume that the distance between the streamer head and the rod (that fills all the gap) is d , and D is the size of the streamer head. The walls around the streamer are grounded (the rod touches them) and set far away so that the boundary conditions on the walls do not influence the field around the streamer head. The setup is shown in figure 4.18.

Using the modeling toolkit Plasimo³ [102] we numerically calculate the electric field in setup in figure 4.18. We compare the radial component of the field on the inside of the streamer ring E_{in} with the radial component of the field on the outside of this ring E_{out} . We vary the thickness D of this ring (defined as the outer radius minus the inner radius), the distance to the dielectric rod r and the relative permittivity ϵ of the dielectric rod. The geometry and the results of our simulations are presented in figure 4.19. We find that for every set of parameters there exists a threshold dielectric constant ϵ_{th} for which $E_{\text{in}} > E_{\text{out}}$. That means that the electrostatic attraction of the conductive ring to the dielectric rod dominates the electrostatic self-repulsion of the ring. The actual number of ϵ_{th} that we obtain in these simple calculations may differ from ϵ_{th} in real experiments and full time-dependent simulations. The existence of ϵ_{th} clearly illustrates however the competition of two important electrostatic effects. In our cylindrically symmetric simulations (and corresponding experiments), the dielectric permittivity of the rod is obviously not sufficiently large to counteract the self-repulsion of the cylindrical streamer.

In full 3D after the destabilization into filaments, the electrostatic self-repulsion is absent and therefore a streamer is attracted to the dielectric rod, as seen at high pressures (figure 4.16).

³The field calculations with Plasimo were done by D. Trienekens.

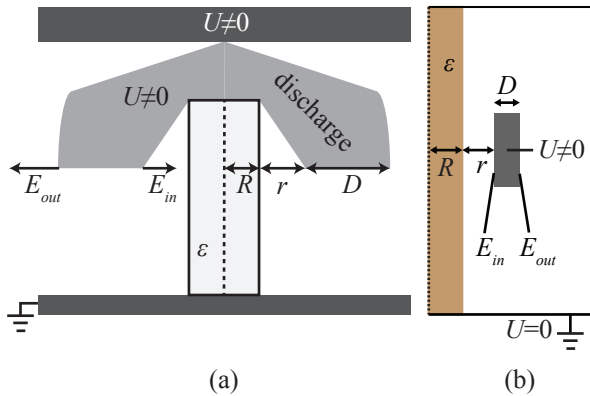


Figure 4.18: Schematic drawing showing the relevant parameters at play when discussing field enhancement in the presence of a discharge. A streamer discharge as depicted in the left figure is approximated as a perfectly conducting ring under a fixed potential as shown in the right figure.

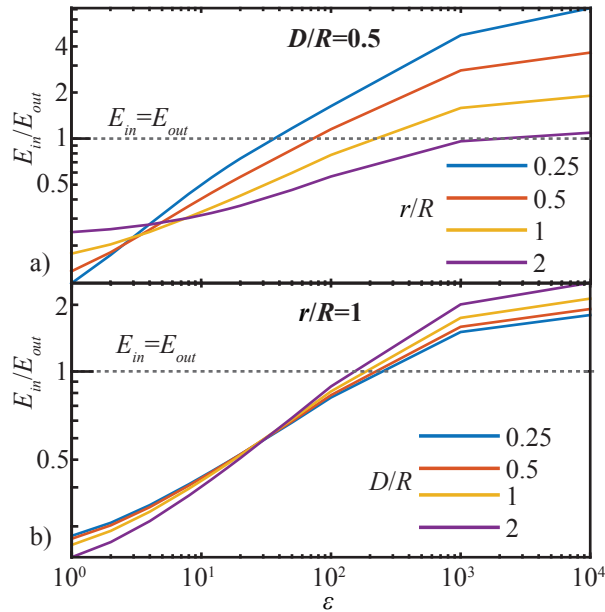


Figure 4.19: Ratio between the radial field on the inside of a conducting ring at fixed potential E_{in} and the field on the outside of the ring E_{out} as a function of relative permittivity of the dielectric rod ϵ for varying distance to the rod r/R a) and for varying ring thickness D/R b). The rod thickness R was kept constant in all simulations. The dotted line shows the conditions when $E_{in} = E_{out}$. There exists a threshold ϵ_{th} such, that for $\epsilon > \epsilon_{th}$, $E_{in} > E_{out}$ meaning that the electrostatic attraction of the conductive ring to the dielectric rod dominates its self-repulsion.

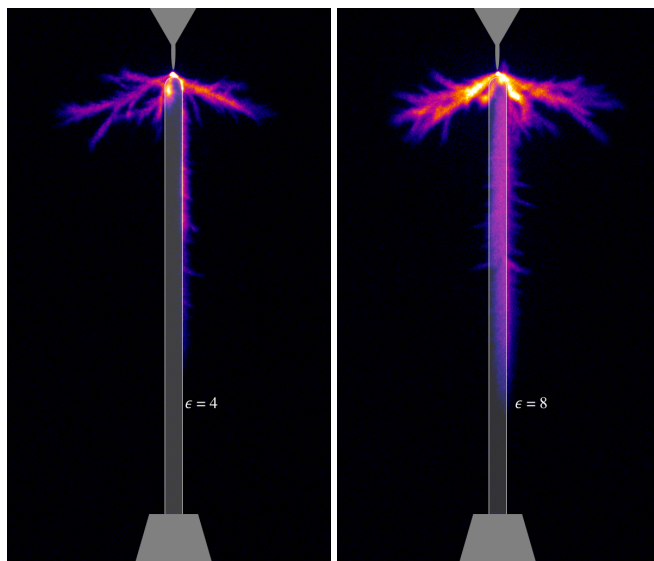


Figure 4.20: Surface discharges observed in 99.9999% pure nitrogen. These images were made by Dirk Trienekens and they were used with his permission.

4.6 Positive streamer interaction with a dielectric rod in pure nitrogen

In pure nitrogen, photoionization is suppressed, and photoemission can be the dominant source of free electrons guides a streamer along a dielectric rod. In our simulations, we switched off photoionization completely to test the hypothesis, though in reality are always impurities and some photoionization is present even in pure nitrogen with 1 ppm oxygen [103]. As shown in figure 4.22, in 100% pure nitrogen, when photoionization is not included, a discharge is pressed to the the dielectric rod (here $\epsilon = 2$) and the space charge becomes very thin, even though the initial background ionization was fairly high, namely 10^6 cm^{-3} . Our hypothesis is also confirmed by experiments (see figure 4.20). However, the direct comparison of our simulated surface streamers with those observed in experiments in pure nitrogen is not, generally speaking, valid. In experiments, a surface discharge is never cylindrically symmetric, whereas our model always gives a cylindrically symmetric solution.

With the increased initial background ionization from 10^6 cm^{-3} to 10^{10} cm^{-3} , a positive discharge does not become a surface discharge. In this case, the initial background ionization replaces the role of photoionization. In the abundance of free electrons in the bulk, a positive discharge does not have to follow the surface. Initial background ionization can be increased in repetitive discharges, in which ionization from the previous discharge does not have enough time to recombine.

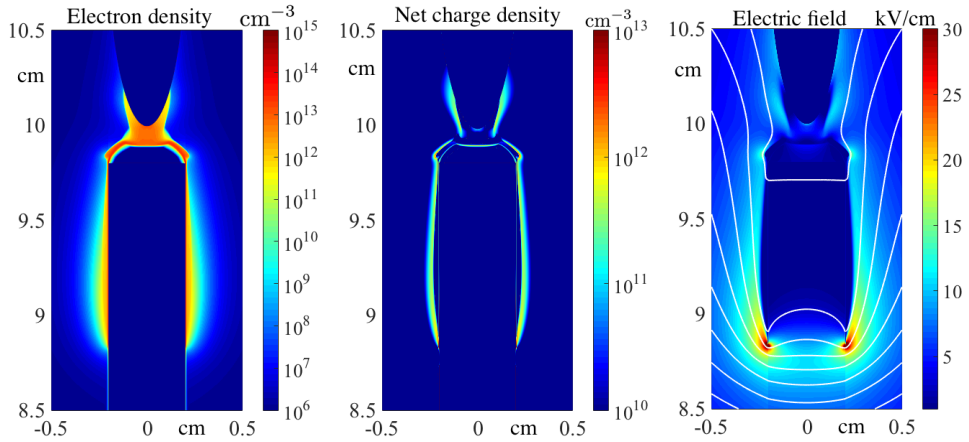


Figure 4.21: A cylindrically symmetric surface discharge in 100% pure nitrogen: its electron density, space charge density, and the electric field with the equipotential lines. The initial background ionization is 10^6 cm^{-3} .

4.7 Conclusions

We have studied interaction of a pulsed positive discharge with a dielectric rod in air in a setup with cylindrical symmetry. Both in experiments and in simulations, no surface discharges have been observed as long as the cylindrical symmetry was preserved, i.e., in the inception cloud phase of the discharge. To our surprise, a positive discharge with cylindrical symmetry tends to move away from the dielectric rod creating a shaded conical region in the centre.

As discussed in section 4.5.1, for small dielectric permittivities and thin rods, next to the dielectric rod the background electric field is hardly perturbed (see left half of figure 4.17). Therefore, in our geometry there is initially little attraction to the side of the dielectric rod.

When a positive inception cloud emerges that is larger than the gap between the electrode and the rod, it extends beyond the rod edge. This leads to a shading effect with an approximately conical shape. If the inception cloud is smaller than the gap (for example at higher pressures or in larger gaps), the cloud breaks up within the gap, breaking the cylindrical symmetry and streamer filaments are formed already in the gap. The interaction of the inception cloud with the rod is different from the interaction of one of the streamer filaments of the discharge with the rod. As elaborated in section 4.5.2, for a cylindrically symmetric discharge with a diameter sufficiently larger than the rod diameter, the electric self-repulsion of the discharge tip acts against the electric attraction towards the rod, whereas for non-symmetrical streamer filaments such self-repulsion is absent.

In general, pulsed positive discharge propagation is governed by two dominant mechanisms: free electron supply and electrostatic field effects. Since in air photoion-

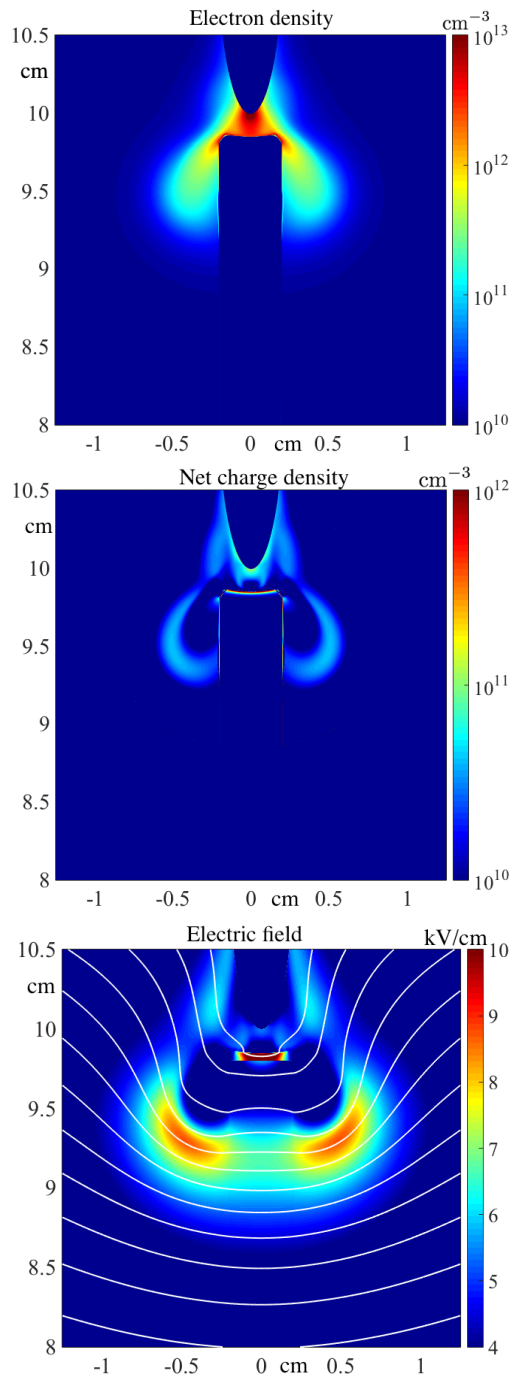


Figure 4.22: A cylindrically symmetric surface discharge in 100% pure nitrogen: its electron density, space charge density, and the electric field with the equipotential lines. The initial background ionization is 10^{10} cm^{-3} .

ization is abundant, electrostatic field effects largely determine discharge propagation. Furthermore, electron supply to the streamer head near the rod is partly suppressed, since no electron avalanches can approach the streamer head from the rod interior. This effect might be counteracted by photoemission from the dielectric surface. The influence of the photoionization, abundant in air, appears to be very strong and dominates the photoemission. Variation of the photoemission yield by seven orders of magnitude from 10^{-7} to the unrealistically large value of 1 in our model does not change the discharge behavior. In pure gases like nitrogen, photoionization is suppressed due to the lack of oxygen. Therefore, the dielectric surface becomes the dominant source of free electrons, forcing positive streamers to propagate on the surface, even if they have to deviate from the electric field lines.

Finally, we expect that all our experiments and simulations, which were performed at moderate pressures (75 to 600 mbar), will give the same results at other pressures assuming that all the lengths scales in the setup (including the size of the dielectric rod) are rescaled according to the Townsend scaling of the discharge. The fact that the quenching factor for photoionization and photoemission do not scale with pressure will hardly change the results.

Chapter 5

Attraction of a positive cylindrically symmetric air streamer to a dielectric rod with an embedded anode

Motivated by the field calculations in section 4.5.1 of chapter 4, we designed a new setup in order to simulate the time-dependent competition between the self-repulsion of a cylindrically symmetric positive streamer and its electrostatic attraction to a dielectric rod. For that setup we found a threshold dielectric permittivity ϵ_{th} such that for a dielectric permittivity higher than ϵ_{th} the electrostatic attraction to the dielectric rod dominates. For $\epsilon > \epsilon_{th}$, the maximum of the electric field in a cylindrical positive streamer is at the surface of the rod. We also studied how the morphology of a cylindrical surface streamer depends on ϵ , and we analyzed how other surface effects can influence that morphology.

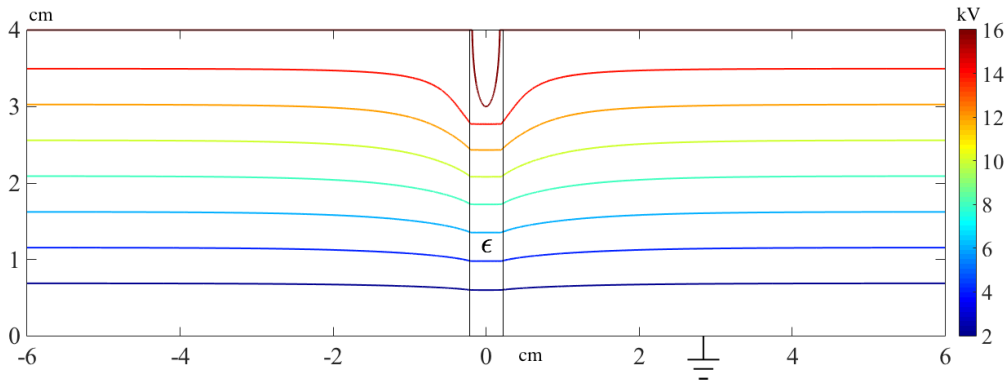


Figure 5.1: Equipotential lines in the simulation domain at the beginning of the simulations. An ellipsoidal anode is embedded into a dielectric cylinder (here $\epsilon = 100$) of 4 mm in diameter. All simulations in this chapter are performed in air at 150 mbar.

5.1 Introduction

In chapter 4, we extensively discussed the interaction of a cylindrical streamer launched from a needle anode with a dielectric rod that was placed very close to the needle. In the parameter regime that was explored there, a cylindrically symmetric positive streamer would always move away from the dielectric rod in air. With very simplistic field calculations in section 4.5.1 we concluded that in our setup the self-repulsion of the cylindrical streamer prevails over its attraction to the dielectric rod. Our field calculations allow the opposite to be true for a sufficiently large dielectric permittivity of the rod or for a larger rod diameter (see figure 4.19). Due to practical reasons, wider rods and rods with the dielectric permittivity ϵ higher than 8 were not available for our experiments, and the field calculations could not be verified. Neither was it possible in the simulations in that setup, because for high ϵ the electric field in the small gap between the needle electrode and the dielectric rod was too high to resolve. This motivated us to redesign the setup in such a way that the needle electrode is now embedded into the dielectric rod and the only surface available for a streamer is the outer surface of the dielectric rod. We kept the rod diameter at 4 mm, as in chapter 4.

5.2 New setup

We study the interaction of a cylindrical positive streamer with a solid dielectric rod. The electrodes are planar at the upper and the lower edge of the rod, and the upper electrode protrudes into the interior of the rod as shown in figure 5.1. We operate at 150 mbar in artificial air. The lower plate is grounded and the upper electrode is at 16 kV over a 4 cm gap. Essentially, the gap is slightly undervolted (the breakdown field in air at 150 mbar is about 4.5 kV/cm), except for the small area around the tip of the anode.

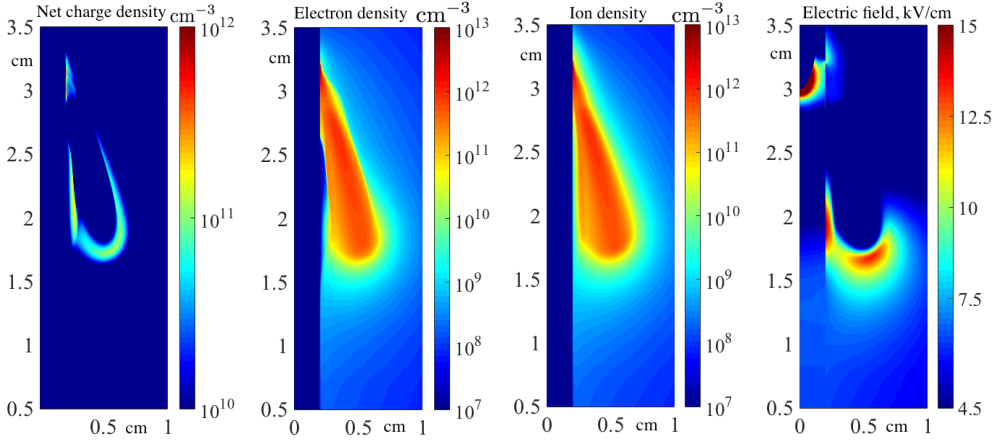


Figure 5.2: Net charge density, electron density, ion density and the absolute electric field of a positive cylindrically symmetric streamer for $\epsilon = 20$ after 67 ns.

The numerical model we use here to simulate a cylindrical streamer discharge is identical to the model used in chapter 4. As initial condition we take the electron and positive ion density of 10^7 cm^{-3} homogeneously spread all over the simulation domain. This initial condition was chosen to facilitate discharge inception in such a way that it does not influence the electrostatic interaction of the streamer with the rod. For the electron transport on all outer boundaries we use Neumann boundary conditions, which means that the boundaries are permeable for electrons. Ions are considered immobile. For simplicity, we first assume no photon induced secondary electron emission, but later we include it to show what difference it can make.

In our simulations we varied ϵ from 15 to 100 and monitored the morphology of the streamers by noting the maximal electric field on the surface of the dielectric rod and outside the surface as a function of time. We define that if the maximum of the electric field in a discharge is on the surface, then the discharge has a surface component.

Our simulation results demonstrate that there indeed exists a transition between two modes of positive cylindrically symmetric streamer discharges: with and without a surface component. Already for $\epsilon = 20$, the maximum of the electric field in the streamer is on the surface and remains there (see figure 5.2), whereas for $\epsilon = 15$, the maximum of the electric field is not on the surface and moves away from it. The comparison of these two scenarios is shown in figure 5.3.

The competition between the surface and the bulk components of the discharge at high ϵ is also illustrated in figure 5.4, where we show the (local) maximal electric field in the discharge on the surface and in the bulk (outside the dielectric cylinder) as a function of time for $\epsilon = 15$, 20 and 50. For $\epsilon = 15$ and $\epsilon = 20$, the difference between the electric field on the surface and in the bulk is fairly small, which suggests that the transition between a discharge with a surface component and a purely bulk discharge is smooth. For the very high value $\epsilon = 50$ of the dielectric permittivity the electric field

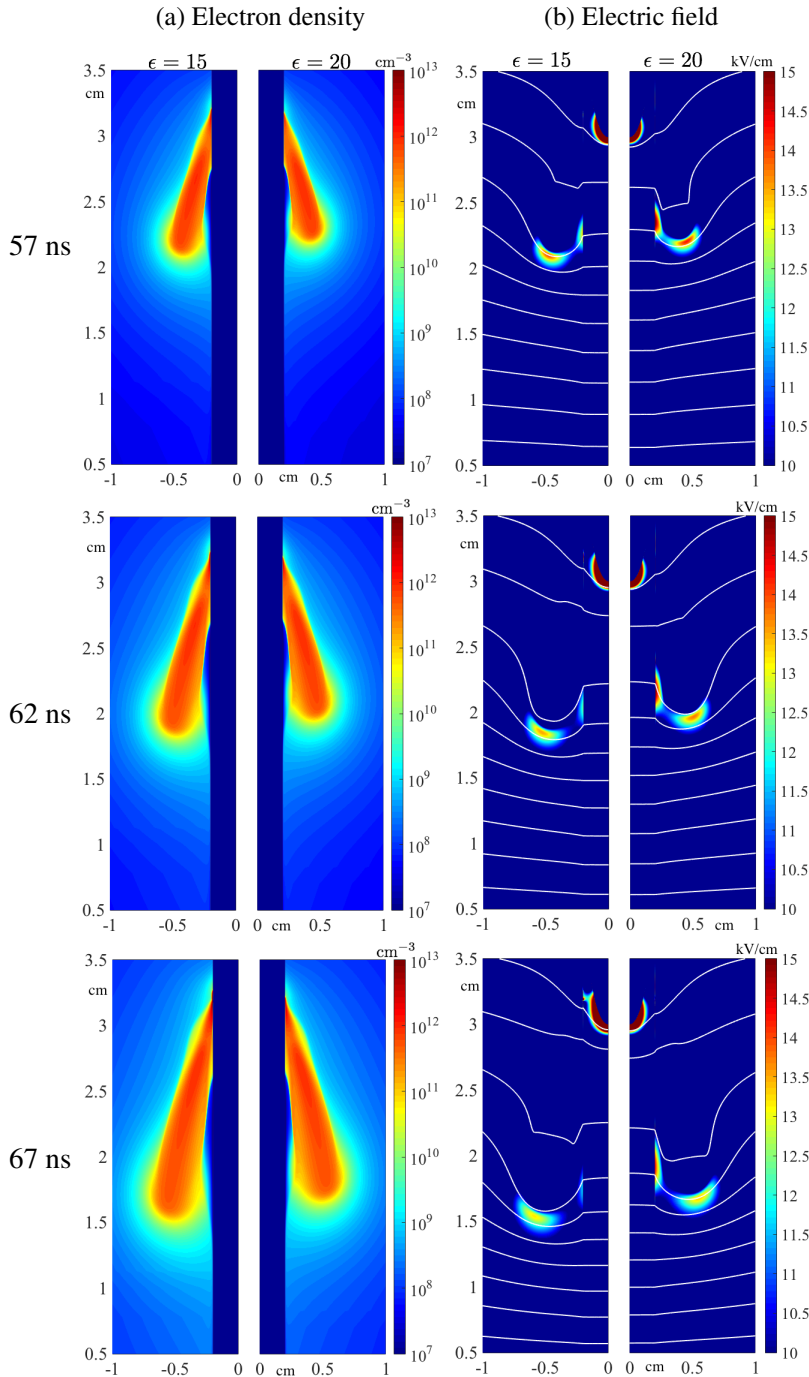


Figure 5.3: The electron density and the absolute electric field with the equipotential lines of a positive cylindrical symmetric streamer after 57, 62, and 67 ns for $\epsilon = 15$ (left half) and $\epsilon = 20$ (right half of each of the six panels). For $\epsilon = 15$, the maximal electric field is in the bulk and the discharge moves away from the surface. For $\epsilon = 20$, the electric field of the discharge has two local maxima: on the surface and in the bulk. The one on the surface is the global maximum.

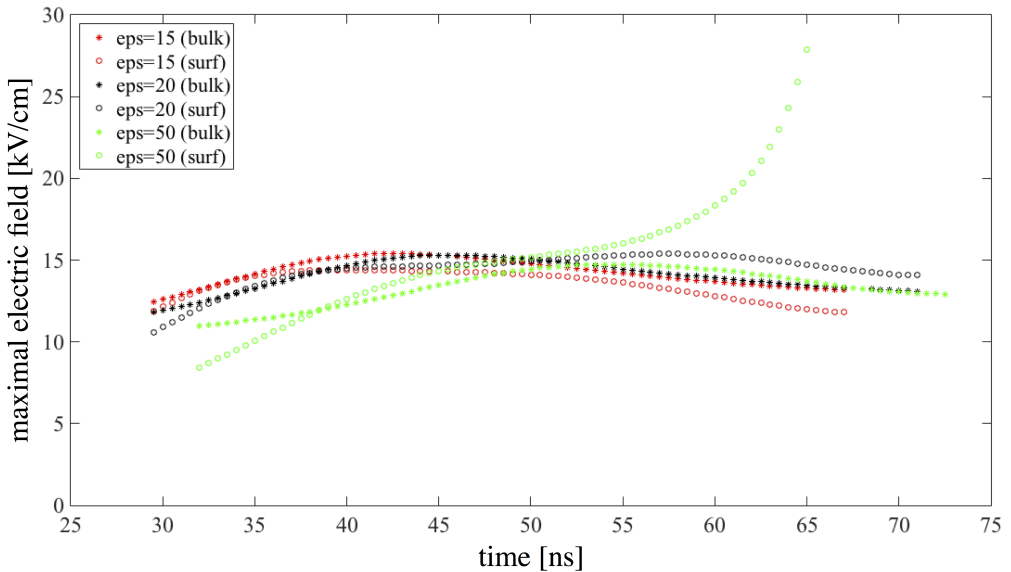


Figure 5.4: The maximal electric field in the discharge on the surface (circles) and in the bulk (asterisks) as a function of time for $\epsilon = 15$ (red), 20 (black) and 50 (green).

on the surface grows rapidly and reaches very high values such that the current physical model may no longer be applicable. At such high fields other surface processes, e.g., field induced electron emission or ion motion, may also become important. In what follows we discuss the potential influence of those other surface processes and give estimations.

5.3 Results

5.3.1 Velocity of streamers

Interestingly, the velocity of the surface and the bulk components differ (see figure 5.5). The velocity of the surface component for all considered ϵ is slightly smaller than the velocity of the bulk component. This is probably due to the fact the outer ring-like component of the discharge hinders the development of the “inner” surface component by electrical shielding and sucking in free electrons into its head. The same line of reasoning is given in [77], where surface and bulk components of streamers were identified in a setup similar to ours. These observations, however, disagree with those reported in [21–24], where higher velocities are measured for surface discharges, also in other setups. The disagreement can be explained with the specific cylindrical geometry, when we have both the surface and the bulk component propagating at the same time and one hinders the other. When the symmetry is broken, there is hardly any shielding, because the components would repel each other and move independently.

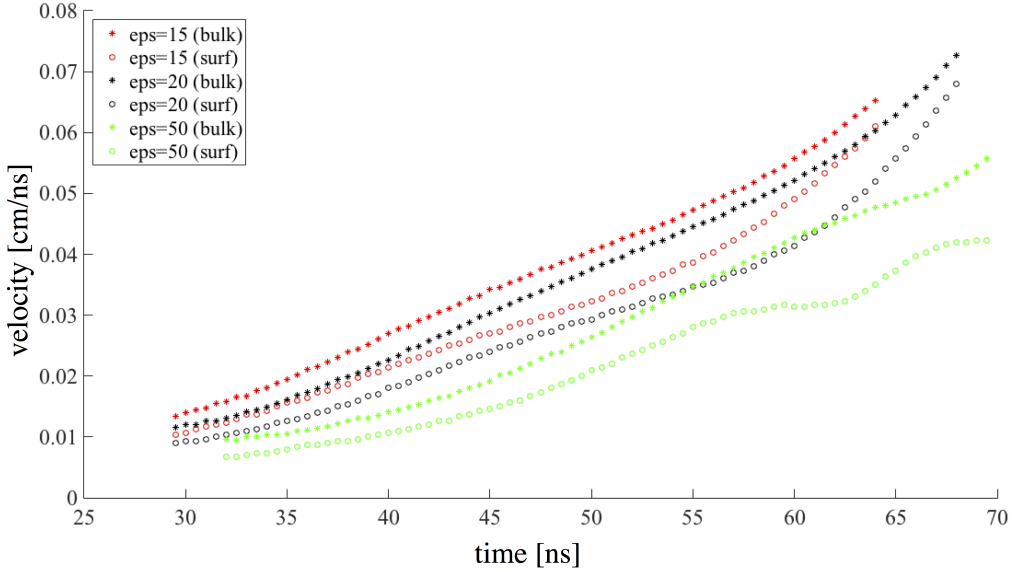


Figure 5.5: The velocity of the maximum of the electric field in a discharge on the surface (circles) and in the bulk (asterisks) as a function of time for $\epsilon = 15$ (red), 20 (black) and 50 (green).

The velocities of both bulk and surface components decrease with increasing ϵ . As ϵ increases, more charge can be accumulated on the dielectric surface. This will essentially deprive positive streamers of free electrons which are necessary for their propagation.

5.3.2 Influence of photoemission

As we already mentioned, positive streamers are sensitive to nonlocal sources of free electrons and photoemission is one of them. Therefore, we included photoemission in our numerical model to see how it influences discharge development in our setup. The photoemission yield was set to the large value of 1 to test the hypothesis.

As was expected, due to photoemission the surface supplies a positive discharge with free electrons and thereby the discharge affinity to the surface increases. This is demonstrated in figure 5.7, where a discharge for $\epsilon = 15$ has no surface component without photoemission, whereas when photoemission is included the discharge has a surface component. However, later on the bulk component of the discharge dominates, as seen in figure 5.6, because the additional electron flux from the surface helps to resolve the charge separation next to the surface, which eventually leads to the decrease of the electric field.

As the electric field simulated in this case is much lower than 100 kV/cm, necessary for sufficient field emission as mentioned in chapter 2, the influence of the field induced

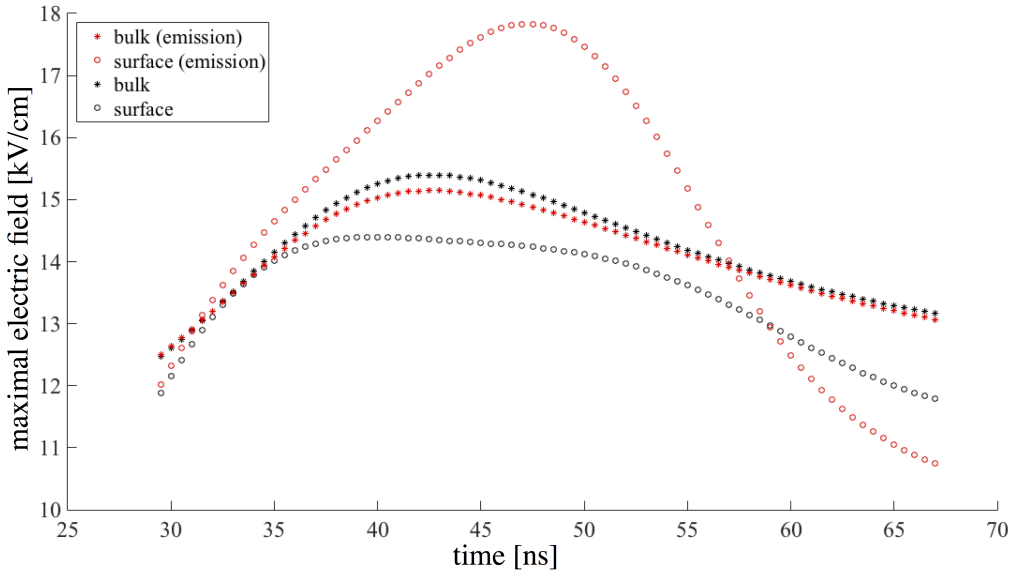


Figure 5.6: The maximal electric field in the discharge on the surface (circles) and in the bulk (asterisks) as a function of time with photoemission included (red) and without it (black). In these simulations $\epsilon = 15$.

electron emission is negligible, but it can play a role in air at 1 bar, when fields as high as 100 kV/cm would be easily reached, according to the Townsend scaling laws.

The potential influence of ion induced secondary electron emission can be estimated using the following line of reasoning. The drift velocity of N_2^+ ions in N_2 as a function of electric field at 150 mbar is calculated with BOLSIG+ [27] and it is shown in figure 5.8. The values are in the range of 0.1 – 0.6 $\mu\text{m/ns}$. The charge layer next to the dielectric surface is about 1 mm (see figure 5.2). On the other hand, the velocities of the simulated streamer with a surface component, as shown in figure 5.5, are in the range of 100 – 700 $\mu\text{m/ns}$. This allows us to conclude that the ion motion is not able to modify the charge layer next to the dielectric surface significantly.

5.3.3 Influence of the diameter of the dielectric rod

With increasing diameter of the dielectric rod and as a consequence the increasing diameter of the cylindrical streamer, the electrostatic self-repulsion of the streamer decreases and the attraction to the rod increases. In other words, the electrostatic self-interaction of the cylindrically symmetric streamer weakens as its diameter grows. In full 3D, when a streamer is not cylindrically symmetrical, the self-repulsion is absent. This can also be emulated by making the dielectric infinitely wide. This hypothesis is illustrated with the help of field calculations in figure 4.19 in chapter 4, where for a wider diameter of the streamer ring, the threshold dielectric permittivity is smaller.

In our simulations, we decided to test the hypothesis. For a rod 4 mm wide and

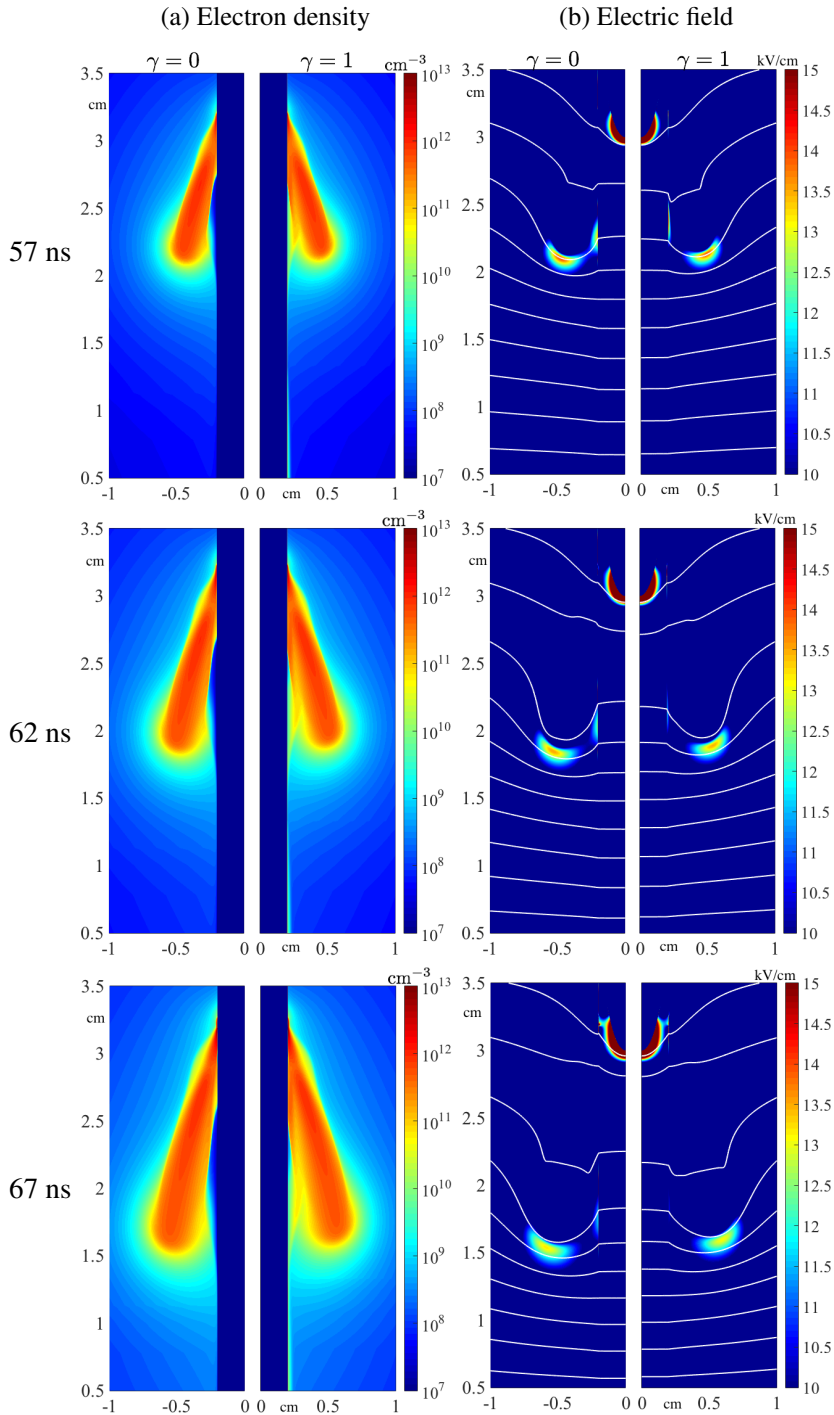


Figure 5.7: The electron density and the electric field with the equipotential lines of a streamer for $\epsilon = 15$ with photoemission included with yield $\gamma = 1$ and without photoemission ($\gamma = 0$). There is a surface component in the discharge when the photoemission is included but after about 58 ns disappears as can be seen in figure 5.6.

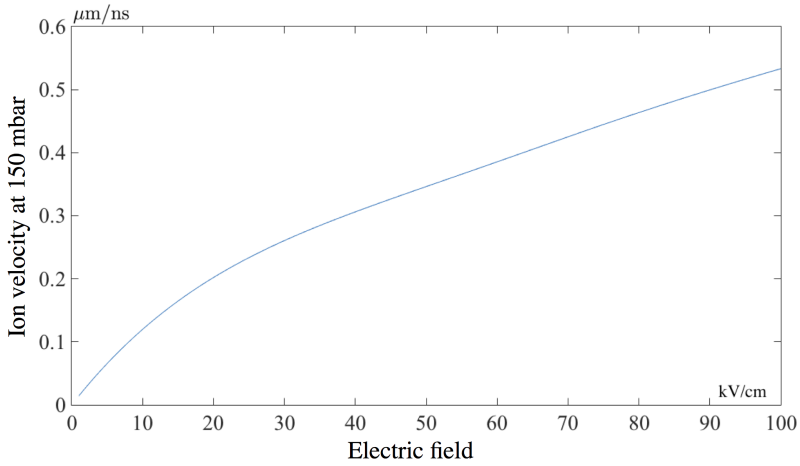


Figure 5.8: The drift velocity of N_2^+ ions in N_2 as a function of electric field at 150 mbar.

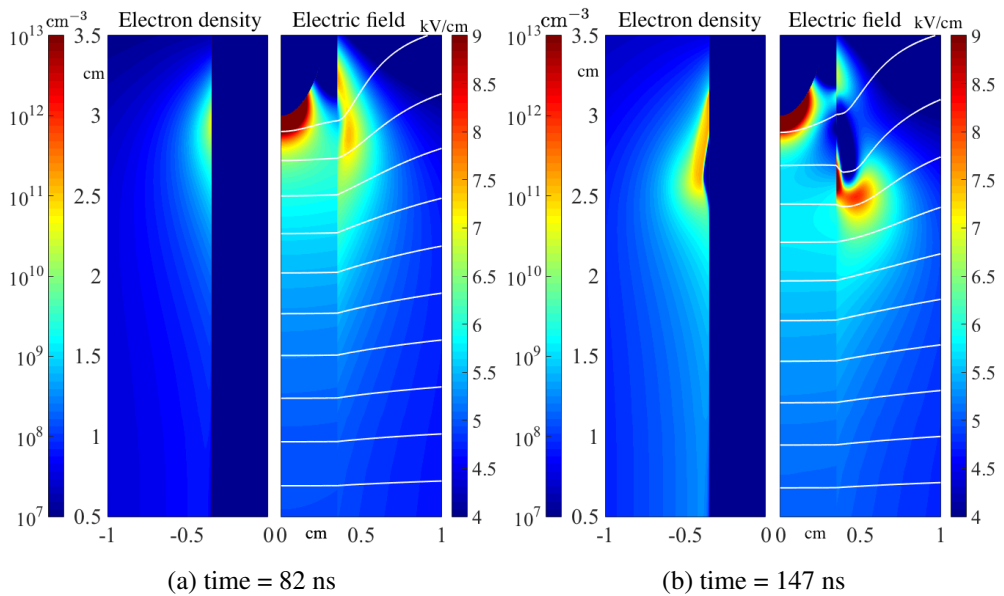


Figure 5.9: The electron density and the electric field with the equipotential lines of a streamer for $\epsilon = 15$ and the rod diameter of 7 mm after 82 ns and 147 ns. The development of the streamer along a wider rod is slower.

with the dielectric permittivity of 15, there is no surface component in the discharge. We increased the diameter of the rod to 7 mm (the diameter of the embedded electrode was increased to 6.6 mm and its length remained 1 cm) and the surface component appeared, as can be seen in figure 5.9. This suggests that electrostatic attraction to the dielectric rod dominates its self-repulsion, and thus supports the hypothesis.

Instead of increasing the diameter of the rod, we could as well increase the air pressure. According to the Townsend scaling laws, as the pressure increases, the streamer becomes smaller, which leads to the increased affinity of the streamer to the dielectric rod.

5.4 Conclusions

In cylindrical geometry, a streamer moving along a dielectric rod experiences the competition of two electrostatic effects: its self-repulsion and its attraction to the dielectric rod. There exists a threshold dielectric permittivity, for which the attraction to the rod is dominant. Photoemission, higher pressure and wider rods can shift this threshold to a smaller value.

Chapter 6

Prediction of lightning inception by large ice particles and extensive air showers

We derive that lightning can start if the electric field is 15% of the breakdown field, which is in accordance with the balloon measurements in [104], and if elongated ice particles of 6 cm length and 100 free electrons per cm^3 are present. This is one particular example set from a parameter range that we discuss as well. Our simulations include the permittivity $\epsilon(\omega)$ of ice. 100 free electrons per cm^3 exist at 5.5 km altitude in air showers created by cosmic particles of at least 5×10^{15} eV. If the electric field zone is 3 m high and 0.2 km^2 in the horizontal direction, at least one discharge per minute can be triggered. The size distribution of the ice particles is crucial for our argument; more detailed measurements would be desirable.

This chapter is based on [A. Dubinova, C. Rutjes, et al., *Phys. Rev. Lett.* 115(1), 015002 (2015)] and [A. Dubinova, C. Rutjes, U. Ebert. *Proceedings of Annual Gaseous Electronics Conference 2015 (ICRP-9/GEC-68/SPP-33)*, Honolulu, HI, USA , 1-2, 2015.]

6.1 Introduction

Lightning inception is the first out of the "top ten questions in lightning research" according to a recent review [105]. How can lightning start when the electric fields in thunderclouds are well below the classical breakdown field E_k [104] that is required for electron multiplication and ionization growth? And when the height of the high electric field zone is typically smaller than a kilometer?

It has been suggested already a few decades ago that a discharge could start in a lower electric field due to the relativistic run-away electron breakdown: cosmic particles could create ionization avalanches of relativistic particles when the electric field exceeds the threshold field $E_{RREA} \approx E_k/10$ for the formation of a relativistic run-away electron avalanche (RREA). However, as the RREA length is of the order of 300 m for a field of 2.8 kV/cm (at standard temperature and pressure) [106], the electric field needs to exceed E_{RREA} over heights of several km.

Another suggestion is that hydrometeors, i.e., airborne particles consisting of liquid or frozen water (droplets, snowflakes, graupel, hail etc.) could enhance the electric field locally in their neighborhood due to their high permittivity [107]. Experiments show how air discharges start from ice particles [108, 109]; however, the background electric fields are here as large as $0.3 E_k$, and the free electrons needed to start the discharge are created through a radioactive source. In [110] an ice particle is modeled as an ionized patch of air. This model demonstrates the field enhancement around a real hydrometeor and the emergence of a discharge, but the electrons are trivially available from the ionized patch while a lack of free electrons is an essential issue in a thundercloud.

Free electrons in the high field region are needed to start a discharge. They are generated up to a few km altitude by the decay of radioactive elements emitted from the ground, and furthermore by solar energetic particles and by cosmic rays. However, within the troposphere these free electrons attach within tens of nanoseconds to oxygen molecules and form roughly 10^3 positive and negative ions per cm^3 . In dry air, the electrons can detach again and start a discharge when the electric field exceeds E_k [111, 112]. But in humid air, the O_2^- ions attract water molecules within microseconds [113]. The electron detachment time from such ion-water clusters is of the order of micro- or even milliseconds [114], and it is negligible on the nanosecond time scale of the primary discharge evolution. Gurevich and Karashtin [115] suggested that the free electrons near a hydrometeor could be supplied by RREAs in air showers created by cosmic particles with energies between 10^{11} and 10^{12} eV. However, they do not elaborate whether a discharge would actually start — according to our analysis below it wouldn't — and their frequency of cosmic particles is 2 or 3 orders of magnitude smaller than in the Review of Particle Physics 2014 [116]. Furthermore, the frequency dependence of the dielectric permittivity $\epsilon(\omega)$ of ice has to be taken into account when calculating the field enhancement near a frozen hydrometeor — it is 93 for static electric fields, but only 3 for fields changing on a nanosecond time scale.

6.2 Structure of the approach

Whether lightning can be started by an extensive air shower hitting a hydrometeor, depends (i) on the distributions of hydrometeor sizes and shapes, (ii) on the distribution of electric fields in the thundercloud, and (iii) on the distribution and properties of extensive air showers created by high energy particles penetrating the atmosphere. Here we determine one set of parameters in this high-dimensional space that is likely to start lightning.

We start with analyzing the requirements on hydrometeor sizes and shapes, on background electron density and on background electric field to start a discharge, and we perform simulations showing that and how the discharge actually starts under these conditions. Then we analyze the energy of the galactic cosmic particles required to create the necessary density of free electrons. Finally we investigate the probability that the requirements on hydrometeors, electric fields and cosmic particles coincide.

The altitude for our calculations is 5.5 km, a typical altitude for lightning inception [117]. According to the International Standard Atmosphere, we assume $T = 250$ K, $p = 500$ mbar, and hence an air density $n = 0.6n_0$, where n_0 is at ground level. The transport and reaction coefficients (electron mobility and diffusion and effective Townsend coefficient including 2- and 3-body attachment) for an air discharge are calculated with BOLSIG+ [27] with Phelps' database [49].

6.3 Requirements on hydrometeor size and shape

A frozen hydrometeor moving in a thundercloud electric field that changes on a millisecond time scale or more slowly will locally enhance the field due to its high dielectric permittivity $\epsilon = 93$. To start a self propagating streamer discharge, a free electron needs sufficiently many ionization lengths in this high field region. This ionization length as a function of the local electric field E is given by the inverse of the effective Townsend coefficient $\alpha_{\text{eff}}(E)$, which is basically the balance of electron impact ionization and electron attachment (hence $\alpha_{\text{eff}}(E_k) = 0$ defines the breakdown field E_k). The electron avalanche multiplication factor e^M along a given path is given by the Meek number $M = \int \alpha_{\text{eff}}(E) dz$ that is widely used in electrical engineering. In our simulations, a Meek number of 10 was sufficient, and we take that number as a benchmark.

Hydrometeors appear in a large variety of shapes, yet their shape in the direction perpendicular to the thundercloud field does not contribute much to the field enhancement at their tip. Essentially the length of a hydrometeor ℓ and its radius of curvature R at the tip parallel to the field determine the electric field enhancement near the tip. Therefore, we approximate the hydrometeor as a prolate ellipsoid of revolution with length ℓ and radius of curvature R . (In this case the pre-discharge field can be calculated analytically [118].) For a Meek number of $M_0 = 10$, the hydrometeor length ℓ required to start a discharge is a function F of the reduced background electric field

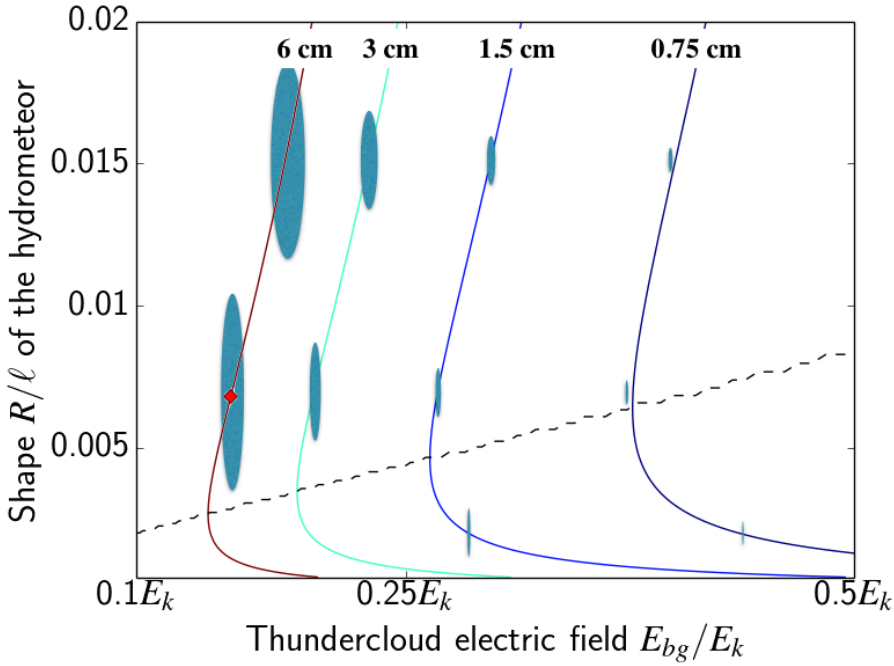


Figure 6.1: Conditions of discharge inception at 5.5 km altitude. The lines of constant hydrometeor length ℓ show when a discharge can start. The axes show the reduced thundercloud field E_{bg}/E_k and the shape parameter R/ℓ . The red diamond indicates the case in figure 6.5. The dashed curve indicates the optimal R/ℓ ratio for given E_{bg}/E_k . The ellipsoids are drawn to scale to illustrate the hydrometeor shape and length.

E_{bg}/E_k and the R/ℓ ratio, and is given by $\ell = M_0 n_0 / n F(R/\ell, E_{bg}/E_k)$. The Meek number is calculated on the symmetry axis where the field is above the breakdown value E_k . Figure 6.1 shows as a result the conditions for a discharge to start at 5.5 km altitude. The contour lines indicate the lines of constant hydrometeor length ℓ as a function of shape parameter R/ℓ and the reduced thundercloud field E_{bg}/E_k . The lines are altitude dependent, and only the length ℓ has to be rescaled. At 0 km, the lines are from left to right 3.4 cm, 1.7 cm, 0.85 cm and 0.43 cm. At 8 km, they are 7 cm, 3.6 cm, 1.8 cm and 0.95 cm, respectively. Lightning inception is possible either for large hydrometeors (the left part in figure 6.1) or for high electric fields (the right part). In other words, to create a sufficiently large number of electron multiplications, a hydrometeor in a given thundercloud field not only has to be sufficiently sharp to significantly enhance the field, but also sufficiently long to enhance it in a large region. The optimal aspect ratio R/ℓ for given E_{bg}/E_k is indicated by the dashed curve. For a given length ℓ , hydrometeors sharper than optimal are less likely to initiate a discharge, even though they have a higher electric field directly at the tip.

Below we present the full analysis for one case indicated by the red diamond in

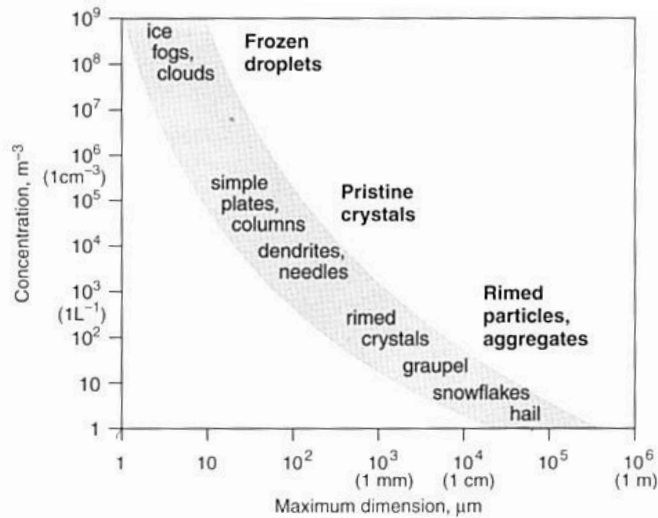


Figure 6.2: Approximate distribution of ice particles depending on their size. Image taken from [119].

figure 6.1. In our simulations, we chose the parameters to minimize the electric field within the parameter space, and therefore the size of the HM had to be on the extreme side in a thundercloud. Yet, such hydrometeors are observed with a density of roughly 0.1 m^{-3} [119], as can be seen in figure 6.2.

6.4 Requirement on the density of free electrons

The Meek number analysis can be applied if there is at least one free electron ahead of the positive end of the hydrometeor at such a distance that it can drift toward it within its life-time (before it attaches to an oxygen molecule). For an air density of $n = 0.6n_0$, the effective electron life time (based on attachment and impact ionization times) is approximately 30 ns. By tracing the electron drift from the hydrometeor surface backward in time for half the life time, we found that they came from a volume with 1.5 mm radius and length, i.e., from a volume of 10 mm^3 . This means that with a homogeneous density of 100 free electrons per cm^3 , on average one electron will be available within the relevant volume to start the discharge

6.5 Discharge inception and propagation from a hydrometeor

The discussion above suggests that a positive streamer (developing subsequently into a lightning leader) can start from an hydrometeor with a radius of curvature of $R =$

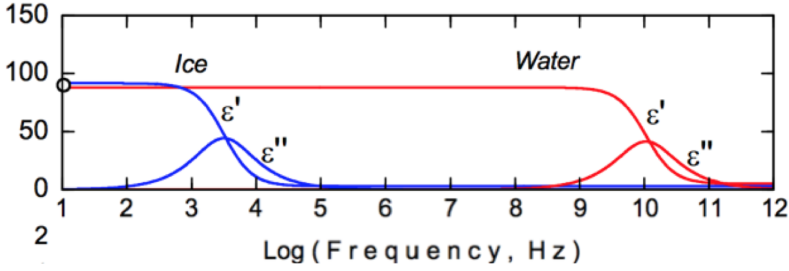


Figure 6.3: The dielectric permittivity of water and ice $\epsilon(\omega) = \epsilon' + i\epsilon''$ [120] as a function of frequency of the electric field.

0.4 mm and 6 cm length in a thundercloud field of 2.7 kV/cm at 5.5 km altitude when the density of free electrons is initially at least 100 cm^{-3} . We now take these parameters as an input for our 3D cylindrically symmetric discharge model and investigate whether a streamer discharge actually forms and propagates.

The discharge is modeled with the classical diffusion-drift-reaction model of [103] with space charge effects, and with photoionization included as in [94].

The hydrometeor is modeled as a dielectric; the dielectric function $\epsilon(\omega)$ of ice depends on frequency ω , it is 93 for slow responses and 3 on the nanosecond time scale [120] or, in other words, on GHz frequencies (see figure 6.3). Unlike ice, the dielectric permittivity of water changes on sub-nanosecond time scale which can be important, for example, for discharges developing in water in electric fields with sub-nanosecond rise-time. The imaginary part of the dielectric permittivity has to be also, generally speaking, taken into account, as it determines the losses due to the non-zero conductivity of the dielectric. However, for water and ice the imaginary part of the dielectric permittivity is small and even minimal (for ice) for fields changing on the nanosecond timescale [121].

We assume that electrons, when reaching the hydrometeor, attach to the surface. No transport, reactions or secondary electron emission are assumed on its surface.

The length of the simulation domain is 8.5 cm and its diameter is 4 cm, sufficiently much larger than the hydrometeor so that the background field can be fixed by appropriate Dirichlet boundary conditions for the electric potential on the boundary. Together with the hydrometeor with dielectric constant 93, this fixes the stationary field.

The discharge plasma develops its own electric field, which changes on the time scale of nanoseconds and the icy dielectric cannot adjust to the changes. Due to the superposition principle, the total electric field is the superposition of the rapidly changing electric field and the stationary electric field. Each of the fields is to be calculated separately with different dielectric permittivities, as illustrated in figure 6.4, where V is the electric potential, and V_0 is the applied potential that generates the static external field.

The equations are discretized on a static nonuniform grid. The grid is refined in the area where a streamer is expected to propagate. The size of the finest grid cells is $1 \mu\text{m}$.

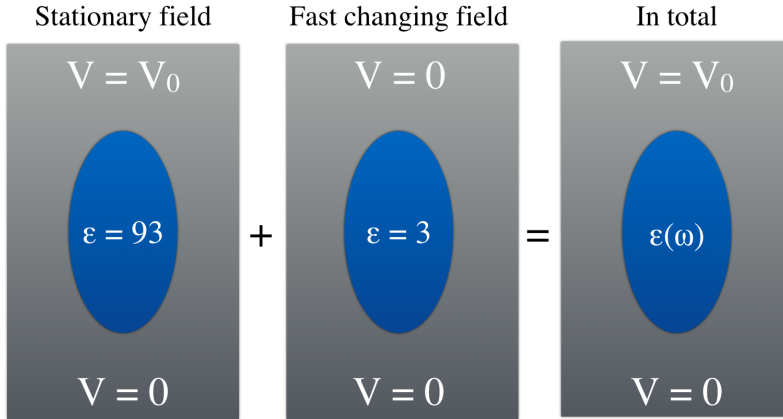


Figure 6.4: The total electric field experienced by the plasma in a discharge is the sum of the fast changing electric field and the static background field. When the latter is calculated, the dielectric constant is set to 93, and when the former it is set to 3.

Away from the area of streamer propagation grid cells quadratically increase in size up to 0.2 mm on the boundaries.

The result of our simulations is shown in figure 6.5, where we show the electron density and the electric field after 46 ns. Clearly a streamer discharge with its strong field enhancement ahead of the tip has formed below the hydrometeor. The streamer incepts after about 25 ns, leaves the area of enhanced electric field and propagates due to its self-generated field enhancement into a region where the field is below the breakdown field. The average streamer velocity is about 10^5 m/s. In figure 6.5, we also compare simulations with the dielectric permittivity of ice set to 93 with simulations with the correct dielectric function $\epsilon(\omega)$ as described above and illustrated in figure 6.4. In both cases we are able to initiate a discharge. In the case of the correct frequency dependent permittivity, the streamer discharge develops with only half of the velocity and stays much thinner. Figure 6.5 also shows that the electric field penetrates deeper into the dielectric, when $\epsilon(\omega)$ of ice is taken into account. Therefore, it is erroneous to take $\epsilon = 93$ for ice on all time scales.

In our simulations we also studied sensitivity of positive streamer inception to the back ground electric field. In figure 6.6 we show the ion density at the tip of the hydrometeor as a function of time² in a constant field approximation for a few values of the background electric field. The results show that there is a distinct threshold value E_{th} for the background electric field E_{bg} . For an electric field as high as 95% of E_{th} , the growth of the ion density is very slow, whereas for the threshold electric field E_{th} the growth becomes exponential. This suggests that for the ellipsoidal hydrometeor that we chose here, a positive streamer discharge can start only when the background

²The ion density defines the space charge buildup at the tip of the hydrometeor, whereas electrons attach to its surface.

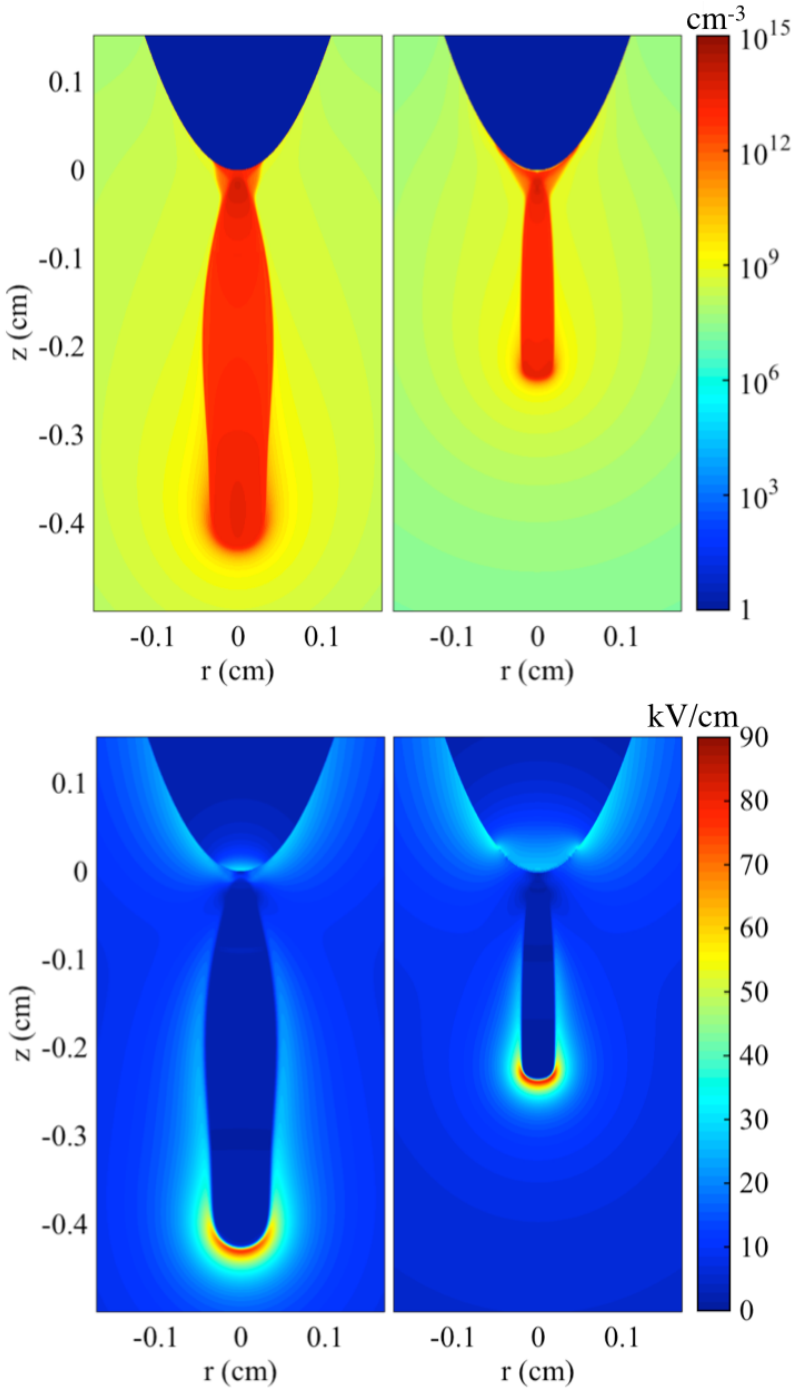


Figure 6.5: Streamer below an icy hydrometeor of length $\ell = 6$ cm and curvature radius $R = 0.4$ mm in a background field of $E_{\text{bg}} = 0.15 E_k$ at 5.5 km altitude. The electron density (upper panel) and electric field (lower panel) of a positive streamer after 46 ns simulated with constant dielectric permittivity 93 (left), and with the dielectric function of ice $\epsilon(\omega)$ [120] (right). Both figures zoom into $r \leq 2$ mm and $-0.35 \text{ cm} \leq z \leq 0.15 \text{ cm}$ after 46 ns of simulation.

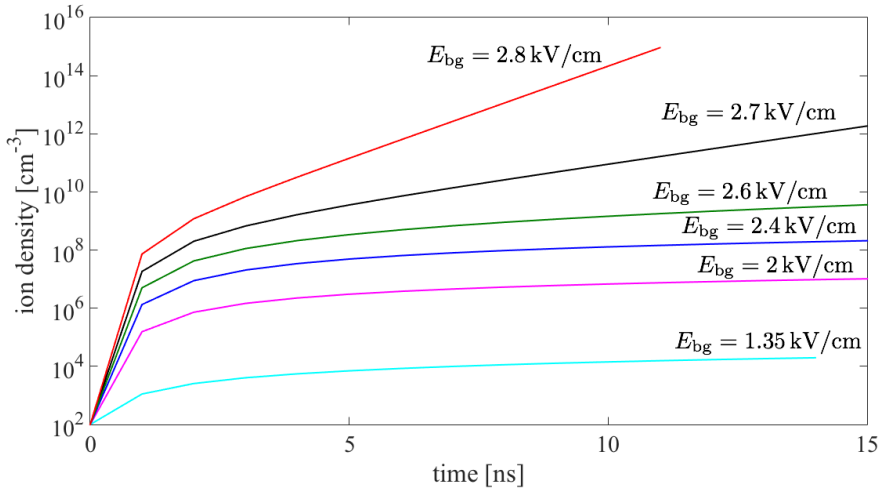


Figure 6.6: Density of positive ions at the tip of the hydrometeor in the avalanche phase as a function of time for different values of the background electric field E_{bg} . These simulations were performed under the assumption that the electric field does not change in the avalanche phase of the discharge.

electric field is at least 2.7 kV/cm under our conditions (with 5% accuracy).

6.6 Occurrence rate of required electron density³

Without assuming a sufficiently high thunderstorm electric field of sufficient extension to form relativistic runaway electron avalanches as in [115, 122], energetic cosmic particles are able to produce enough free electrons in so called extensive air showers [116]. We will now calculate the occurrence rate of such events based on models developed for cosmic ray physics.

We focus our analysis on protons with energies between 5×10^{15} and 5×10^{16} eV. Our calculations described below show that below 5×10^{15} eV it is very unlikely that the core of an extensive air shower reaches a density of 100 thermal electrons per cm^3 at 5.5 km altitude, while above 5×10^{16} eV the electron density is always sufficient, but the occurrence rate decreases with the energy E of the cosmic particle as E^{-2} .

Cosmic protons with energies between 5×10^{15} and 5×10^{16} eV first interact with an air molecule at about 15 to 25 km altitude, which marks the begin of the shower. The number of secondary particles in the shower then increases until it reaches a maximum between 4 and 8 km altitude, depending on the energy of the primary particle, on the inclination of the particle trajectory with respect to the vertical axis and on the altitude of first interaction. The shower develops downward with nearly the speed of light, and resembles a disc of high energetic particles that leaves a trail of non-relativistic particles

³In section 6.6, the calculations were performed by C. Rutjes.

behind. The shower has a narrow core with a very high particle concentration.

Extensive air showers can be simulated by the Monte Carlo program CORSIKA [123] that follows particle movement and interactions explicitly down to an user defined energy threshold of at least 50 keV. However, we need the density of free electrons in the eV range that could start the discharge shown in figure 6.5. So we need to follow the particle generation and motion below CORSIKA's energy threshold. As the cross sections for impact ionization by electrons and positrons are four orders of magnitude larger than for photo-ionization, while the photon number is only a factor 20 larger, we only calculate the lower energy electrons generated by electrons and positrons. The particle density above this threshold is calculated using the restricted collisional stopping power [124] divided by the net cost per ionization of about 30 eV, this strategy is in line with [122]. This combination of approaches determines the thermalized free electron density within the core of each shower.

We have simulated 297 showers with primary proton energies between 5×10^{15} and 5×10^{16} eV and with random inclinations, and we have determined the flux of electrons and positrons with energy above 1 MeV in the shower core at 5.5 km altitude. A typical output are 10 to 40 million particles with roughly 90 % photons, 4 % electrons and 4 % positrons. From these we determined the density of electrons with eV energy within the core of 1 meter radius according to the prescription above. Taking the measured differential cosmic ray flux [116] into account, the density of 100 thermal electrons per cm^3 in the core is reached with a frequency of at least $5 \text{ km}^{-2} \text{ min}^{-1}$ within our sample.

6.7 Probability of coincidence of large hydrometeor and extensive air shower inside the thundercloud field

As sketched in figure 6.7, we require three phenomena to coincide in space and time: a thunderstorm electric field, a hydrometeor that is large and elongated enough, and an extensive air shower creating a sufficient density of thermal electrons.

First, at least one hydrometeor of sufficient size and shape has to be inside the core of the air shower. For a core radius of 100 cm and a hydrometeor density of 10^{-7} cm^{-3} , a height of $h \approx 3 \text{ m}$ is sufficient. This limits the spatial height where the electric field has to exceed 2.7 kV cm^{-1} to 3 m as well.

Second, the air shower has to hit the horizontal area in the cloud where the electric field exceeds 2.7 kV cm^{-1} . With at least 5 sufficiently energetic showers per km^2 and per minute, we find at least one shower per second, if the horizontal high field area A is 12 km^2 , or equivalently 1 shower per minute, if the area is 0.2 km^2 .

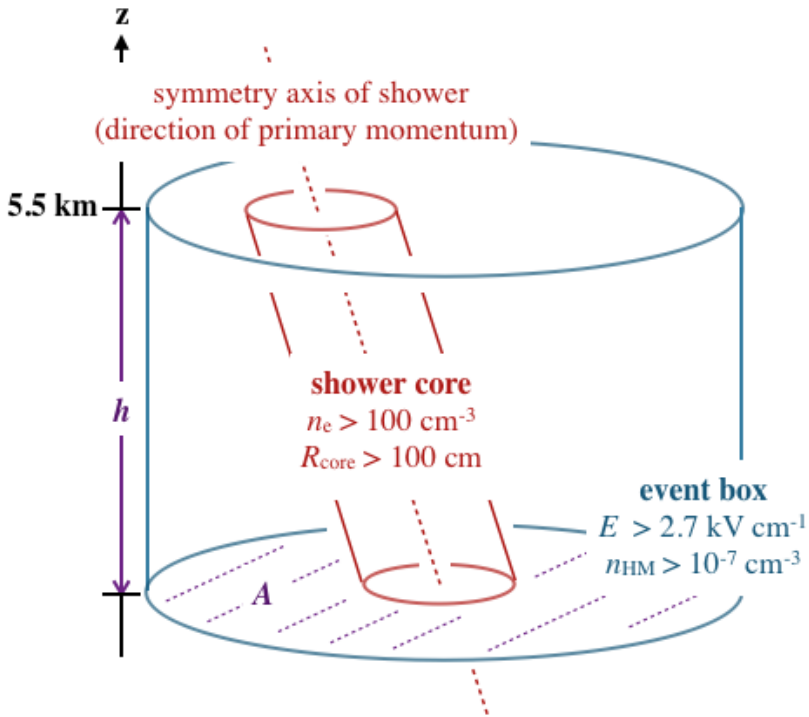


Figure 6.7: Sketch of the model ingredients; not to scale. In the event box (blue) at an altitude of 5.5 km we assume an electric field $E \geq 2.7 \text{ kV cm}^{-1}$, a density $n_{\text{HM}} \geq 10^{-7} \text{ cm}^{-3}$ of hydrometeors of correct shape and size, and at least one extensive air shower creating a thermalized free electron density $n_e \geq 100 \text{ cm}^{-3}$ in a core (red) of radius $\geq 100 \text{ cm}$. The height h and horizontal area A of the event box are determined by shower distribution and inception frequency.

6.8 Summary and discussion

We have found that elongated hydrometeors of centimeter size are required to start a discharge at 5.5 km altitude, if the background field is as low as 0.15 times the classical breakdown field, and our simulations with a realistic permittivity $\epsilon(\omega)$ of ice showed that a streamer discharge actually can emerge, if 100 free electrons per cm^3 are present. But due to electron attachment to oxygen and the formation of water clusters around these ions, free electrons are typically too rare for a discharge to start. However, a cosmic proton with energy above $5 \times 10^{15} \text{ eV}$ can create an extensive air shower whose core can provide the necessary electron density. These air showers appear with a frequency of 1 per 0.2 km^2 per minute, and hence can explain how lightning discharges can start in an undervolted region. According to this argument, lightning inception at higher altitudes – say 12 km – is less likely as the hydrometeor has to be larger and as the electron density in the extensive air shower is lower at these altitudes.

Our simulations also demonstrated how important the dependence of the dielectric permittivity on frequency can be for positive streamer development. The dielectric permittivity of ice drops from 93 to 3 on already at a sub-millisecond time scale. A typical streamer discharge in STP air typically develops on a nanosecond time scale. Therefore, the dipoles inside an ice particle cannot follow the changes produced by the space charge field in a streamer. That significantly influences streamer dynamics in the vicinity of a hydrometeor.

The strongest constraint in our analysis comes from the sizes of the hydrometeors which are little investigated within thunderclouds. Mason [125] suggested already in 1953 a correlation between graupel size and lightning inception — which should be studied further.

The height of the zone where the electric field has to exceed the runaway threshold is only of the size of meters, rather than of more than a kilometer as required for a relativistic runaway avalanche, and relativistic avalanching in an external electric field is not required in our model. Rather all free electrons are generated by the energy of the primary cosmic particle. The required height of the electric field zone is inversely proportional to the density distribution of large hydrometeors.

Finally, in our rare event analysis for the electron density in the shower core, we have focussed on a core radius of 1 m. Future analysis might reveal even more favorable core radii and related primary particle energies.

Chapter 7

Streamer discharge inception in a sub-breakdown electric field from a solid boundary in air

Here we deal with inception near an elongated dielectric body in a sub-breakdown electric field with an arbitrary distribution of initial electrons, beyond the results discussed in the previous chapter. We analyze how charge builds up at the tip of a dielectric in multi-avalanche streamer inception on the basis of the ionization integral, i.e., the Meek number. We take into account the high non-uniformity of the electric field around the tip of the dielectric, which makes it important where an electron avalanche starts and which electric field line it follows. We also study the influence of the spatial distribution of the initial electrons that start the avalanches. The initial electrons can be spread out around the tip of the dielectric when, for example, they are instantaneously produced by highly energetic cosmic particles bombarding our atmosphere.

7.1 Analysis of discharge inception based on the Meek number

7.1.1 Introduction of the Meek criterion for negative streamers in bulk gas

An electron avalanche is characterized by negligible space charge with the electric field much smaller than the external field. To start such an avalanche, one needs an external electric field above a critical (classical breakdown) field and a seed electron (or electrons).

The density of electrons n_e in an electric field \mathbf{E} is governed by the continuity equation with a source term. With the electron diffusion neglected, the equation in 1D reads

$$\frac{\partial n_e}{\partial t} - \mu_e E \frac{\partial n_e}{\partial z} = \mu_e |E| n_e \alpha_{\text{eff}}, \quad (7.1)$$

where α_{eff} is the effective ionization coefficient given by

$$\alpha_{\text{eff}} = \alpha - \eta, \quad (7.2)$$

and where α is the Townsend impact ionization coefficient, and η is the attachment coefficient. For brevity, we omit the subscript “eff” and use α meaning α_{eff} . The solution of equation (7.1) with a constant electric field E_{bg} describes the evolution of the electron density:

$$n_e(z, t) = n_e(z - v_d t, 0) e^{\alpha z}, \quad (7.3)$$

where $v_d = -\mu_e E_{\text{bg}}$ is the electron drift velocity.

We remark that equation (7.3) is valid when the number of electrons is sufficiently large and the law of large numbers holds. Alternatively, the probability distribution of the number of electrons N in an avalanche $\nu(N)$ should be used instead [126, 127]:

$$\nu(N) = \frac{1}{\bar{N}} \left[1 - \frac{1}{\bar{N}} \right]^{N-1}, \quad (7.4)$$

where $\bar{N} = \exp(\alpha d)$ and d is the length of the avalanche. This distribution is valid for non-attaching gases, where the number of positive ions is equal or one less than the number of electrons. In electronegative gases, the number of electrons and the number of positive ions differ by the number of negative ions and equation (7.4) should be corrected [127]. If an electron avalanche is launched by a single electron, a significant jitter time may be expected before the avalanche develops due to the probability distribution of the number of electrons in an avalanche and due to the position of the seed electrons.

Seed electrons in an avalanche can appear, for example, due to detachment from a negative ion, emission from a surface or due to natural ionization (cosmic rays, radioactive decay). On large length and time scales, such as in thunderclouds, free electrons can temporarily be produced due to extensive air showers [128].

Let us consider an electron in air in an external static uniform field above breakdown, then the expectation value of the number of electrons N in an avalanche on a distance of interest d can be calculated as

$$N = e^M, \quad \text{where } M = \alpha d. \quad (7.5)$$

When the Meek number M , defined as αd , reaches a threshold value M_0 , an electron avalanche is expected to transform into a (negative) streamer, as the number of produced electrons and positive ions is large enough that the electric field of their space charge is comparable to the external electric field. From that moment on, space charge effects should not be neglected.

In uniform fields far away from electrodes, the Meek criterion has been extensively studied both theoretically [12] and experimentally [129–131] and it states that a streamer discharge incepts when the Meek number M reaches M_0 in STP air:

$$M_0 = 18 \text{ to } 21 + \ln(d[\text{cm}]) - \ln N_0. \quad (7.6)$$

Here, d is the length of the electron avalanche and N_0 is the number of initial electrons starting the avalanches. The second term in equation (7.6) stems from an analysis of electron production in an avalanche taking into account electron diffusion [12]. When an avalanche starts from multiple initial electrons then the third term becomes important, because every initial electron can create an independent avalanche. This has also been experimentally observed in [132], where the streamer inception voltage was measured depending on the number of primary electrons created by laser radiation. Even though this criterion in equation (7.6) is a result of simplified calculations (for a more thorough analysis see [133]), it is widely used in electric engineering to avoid unwanted discharges.

For nonuniform electric fields $E(z)$, the electron production in an avalanche is given by

$$N(z) = N(0) \exp \left(\int_0^z \alpha(E(z)) dz \right), \quad (7.7)$$

and the ionization integral (or the Meek number) is generalized as follows

$$M(z) = \int_0^z \alpha(E(z)) dz, \quad (7.8)$$

where $E(z)$ is the absolute value of the electric field, and z is a coordinate, assuming that the avalanche started at $z = 0$.

Notably, the Meek criterion as introduced above is meant for avalanche to negative streamer transition in bulk gas. For positive streamers near a fixed boundary, this criterion has to be revisited.

7.1.2 Density description of avalanche to streamer transition

In the density description of streamer discharge we deal with electron density instead of counting individual electrons. For the density approximation to be accurate, the

law of large numbers should hold and we can define the electron density distribution in space. When we use a particle description of an electron avalanche, we talk about the probability of discrete electrons to produce more electrons due to impact ionization or to disappear due to attachment to a molecule. And in the density approximation, which we use in this chapter, we talk about continuous increase or decrease of the electron density. Avalanche to streamer transition in the density approximation takes place when the space charge density reaches the “typical” streamer density, which is about 10^{12} to 10^{14} cm^{-3} in STP air in a sufficiently large volume. In an avalanche to positive streamer transition next to a surface the space charge is positive with a surplus of positive ions. In what follows we focus on positive streamer inception.

Let us consider an instantaneous injection of free electrons of a given density everywhere in a nonuniform field, for example at the tip of a dielectric body¹. All these electrons can potentially contribute to the avalanche formation, but their contributions differ depending on their initial location with respect to the dielectric. Essentially, we talk about multiple avalanche assisted streamer inception near a fixed boundary. In the framework of the electron density, the ionization integral describes only one avalanche, although the most powerful one. It does not account for the contributions of neighboring avalanches which can be almost as powerful and it focusses on the electrons that attach to the boundary, rather than on the positive ions left behind.

7.1.3 Illustration of the multiple avalanche streamer inception in the density perspective

In what follows, electron avalanches is considered in air at 5.5 km altitude (0.5 bar and 243 K) at the tip of an ellipsoidal dielectric made of ice 6 cm long and 0.7 cm in diameter in the locally enhanced sub-breakdown background electric field of 2.7 kV/cm (or 4.5 kV/cm in STP air), as can be seen in figure 7.1. This example is used in chapter 6 for lightning inception.

In figure 7.1 we also show the Townsend impact ionization coefficient $\alpha(z)$ (including attachment) on the z axis underneath the dielectric ice particle. Here we used the BOLSIG+ solver [27] with Phelps database, retrieved on July 31, 2014. The dashed line in figure 7.1 indicates the point z where $\alpha = 0$. Beyond that point α is negative, which means that single electrons are more likely (on average) to attach to a molecule than to produce an extra electron in a collision.

In figure 7.2 we show the electron multiplication factor $\exp(\int_0^z \alpha dz)$ as a function of the position z from where electrons (as a population in the density approximation) start moving towards a dielectric boundary. Eventually, the electrons attach to the surface of the dielectric but they leave positive ions behind, which are important for positive streamers. The maximum of the multiplication factor is located at the point z where $\alpha = 0$. In the density approach, the density of electrons decreases where $\alpha < 0$. However, the electrons drift in the electric field towards the dielectric tip where the electric

¹In this section it does not matter, whether it is a dielectric or conductive body.

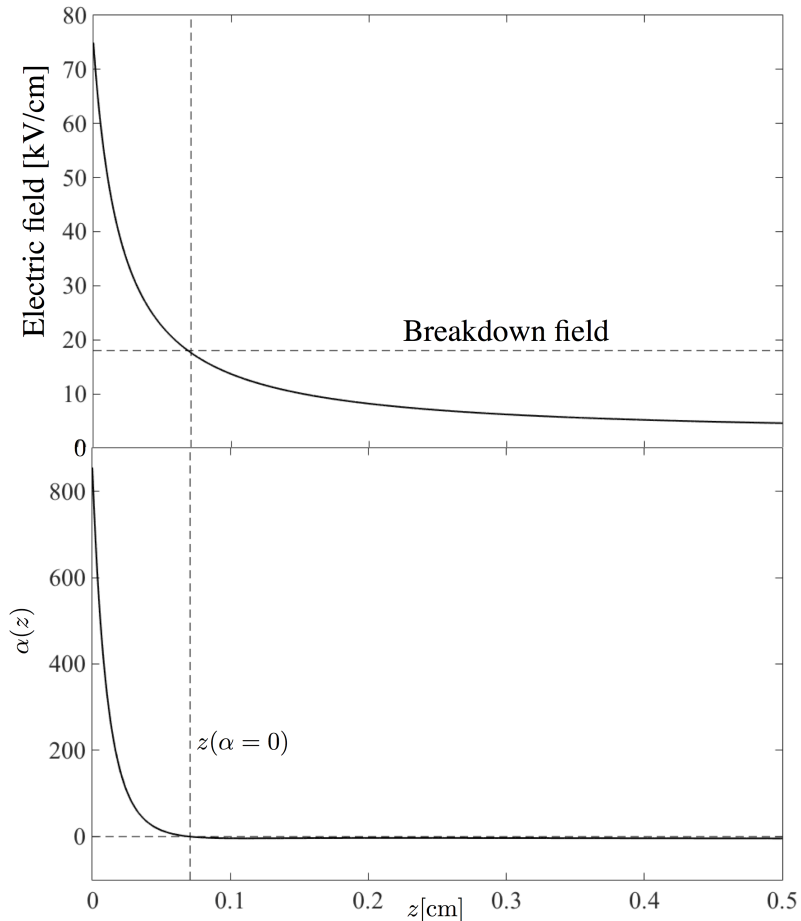


Figure 7.1: Top graph: enhanced electric field $E(z)$ on the z axis underneath a dielectric. The horizontal dashed line shows the breakdown electric field. Bottom graph: Townsend impact ionization coefficient $\alpha(z)$ (including attachment) on the z axis underneath the dielectric. The vertical dashed line indicates the point z where $\alpha = 0$. These calculations are based on the example used in chapter 6 for lightning inception. An electron avalanche is considered in air at 5.5 km altitude (0.5 bar and 243 K) at the tip of an ellipsoidal dielectric made of ice 6 cm long and 0.7 cm in diameter in the sub-breakdown background electric field of 2.7 kV/cm.

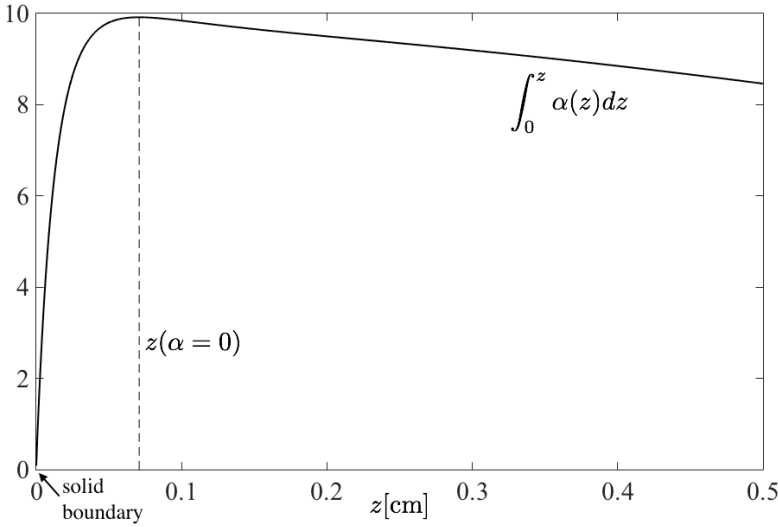


Figure 7.2: Meek number $\int_0^z \alpha dz$ as a function of the position z where electrons (in the density approximation) start moving towards the solid boundary at $z = 0$. The maximum corresponds to the point where $\alpha = 0$ (see figure 7.1).

field is above breakdown. At some point they can reach the area where $\alpha > 0$ and start an avalanche. Hence, the contribution of those electrons should also be added. On the other hand, electrons that start moving where $\alpha > 0$ have a smaller distance to drift before they attach to the surface of the dielectric. Even though their contribution is smaller than that of the electrons starting exactly at the point where $\alpha = 0$, they can still contribute to the avalanche formation.

In the density approximation, multiple avalanches are interpreted as infinitely many avalanches with different weights. In 1D, the integrated effect of the avalanches can be described with a “double” ionization integral $M_{\text{dens}}(z)$ by summing up the multiplication factors of all electron avalanches:

$$M_{\text{dens}}^{\text{1D}} = \ln \left[\int_0^\infty n_{z0}(z') \exp \left(\int_0^{z'} \alpha(E(z'')) dz'' \right) dz' \right], \quad (7.9)$$

where $M_{\text{dens}}^{\text{1D}}$ is the ionization integral at point $z = 0$ with the contributions of all electrons arriving at $z = 0$, $n_{z0}(z)$ is the linear density of initial electrons (the number of electrons per length). With all those electron avalanches taken into account, the number of electrons passing the tip of the dielectric at the point $z = 0$ is $N = e^{M_{\text{dens}}^{\text{1D}}(z=0)}$.

7.1.4 Time restriction for the charge growth at the tip of the dielectric

For some avalanches starting too far away, although potentially able to contribute to charge growth at the tip of the dielectric, it takes too long to reach it. In other words, on

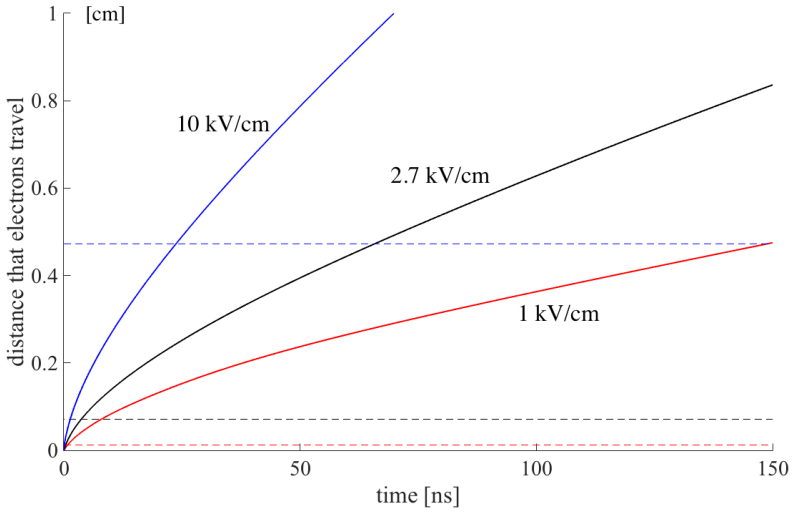


Figure 7.3: The distances that electrons travel to reach the surface of the dielectric (due to drift) within a given time in *the background electric field* 1 kV/cm (red line), 2.7 kV/cm (black line) and 10 kV/cm (blue line) *amplified by the dielectric ice particle*. The dashed lines of the same color show the position of the point z where $\alpha = 0$. The black curves (solid and dashed) correspond to the case shown in figure 7.1.

a longer time scale other processes (such as ion motion or diffusion) can hinder charge buildup at the tip of the dielectric. One of those limiting factors is ion motion. For a positive streamer to start, enough positive charge should be built up around the tip of the dielectric. On smaller time scales, it is reasonable to assume that ions do not move, but on longer time scales they drift away from the dielectric tip and thereby suspend the space charge growth.

Using the same example of the ellipsoidal dielectric made of ice as described above, we estimated the distances that electrons travel to reach the surface of the dielectric (due to drift) within a given time interval. Basically, we calculated the time as $\int_0^z dz / \mu E_z$ as a function of z , which we plotted in figure 7.3. The electron mobility μ was calculated using BOLSIG+ solver [27] with Phelps database, retrieved on July 31, 2014. The figure also demonstrates that an electron avalanche can indeed reach the tip of the dielectric from areas where the electric field is lower than the breakdown field. Some electrons would attach to oxygen molecules, but some would reach the area of high electric field and start an avalanche. In the density approximation this means that the electron density in an avalanche first decreases and then increases. For example, within 50 ns an electron avalanche can come to the dielectric tip from as far as 4 mm at 2.7 kV/cm (see figure 7.1), whereas the electric field is above breakdown only within 0.7 mm from the tip.

We also estimated how far N_2^+ ions could potentially drift from the tip of the dielectric within a given time in different background electric fields using BOLSIG+ [27] to

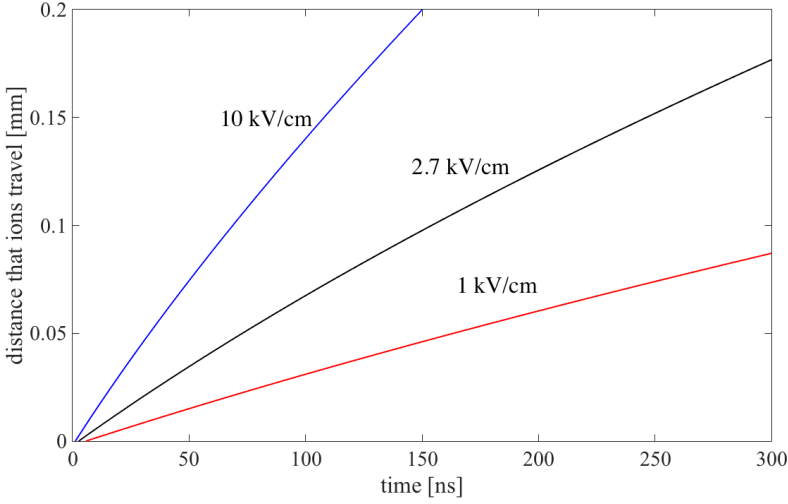


Figure 7.4: The largest distance that an N_2^+ ion can move from the surface of the dielectric within a given time in the background electric of 1 kV/cm (red line), 2.7 kV/cm (black line) and 10 kV/cm (blue line) amplified by the dielectric ice particle.

calculate the ion mobility (in N_2 [49]). The largest distance that an N_2^+ ion can move from the dielectric tip as a function of time in a background electric field (amplified by the dielectric) is shown in figure 7.4. The figure shows that on the timescale of hundreds of nanoseconds (depending on the background electric field), positive ions can drift away from the area of field enhancement and further development of the discharge is suspended.

To sum up, space charge at the tip of the dielectric cannot grow interminably, because on larger time scales other processes, such as ion motion or diffusion, start playing a role.

7.1.5 Electron avalanches developing along different field lines

An electron avalanche can start from an arbitrary point below the dielectric, not necessarily on the z axis, and develop along an electric field line that does not coincide with the z axis. We calculated the ionization integrals along different field lines $\exp(\int_0^{s(\alpha=0)} \alpha ds)$, where s is the coordinate on a field line and $s = 0$ where the field line crosses the dielectric tip. In figure 7.5 we plotted the Meek number $\int_0^{s(\alpha=0)} \alpha ds$ as a function of the distance from the z axis to the field line. The Meek number decreases smoothly in the vicinity of the axis, which suggests that electron avalanches starting off the z axis can also contribute to the charge growth at the tip of the dielectric.

The electric field lines around the tip of a dielectric converge. This eventually compresses electron avalanches and leads to a larger charge density at the tip. In general, the contributions from all avalanches should be summed up with appropriate weights

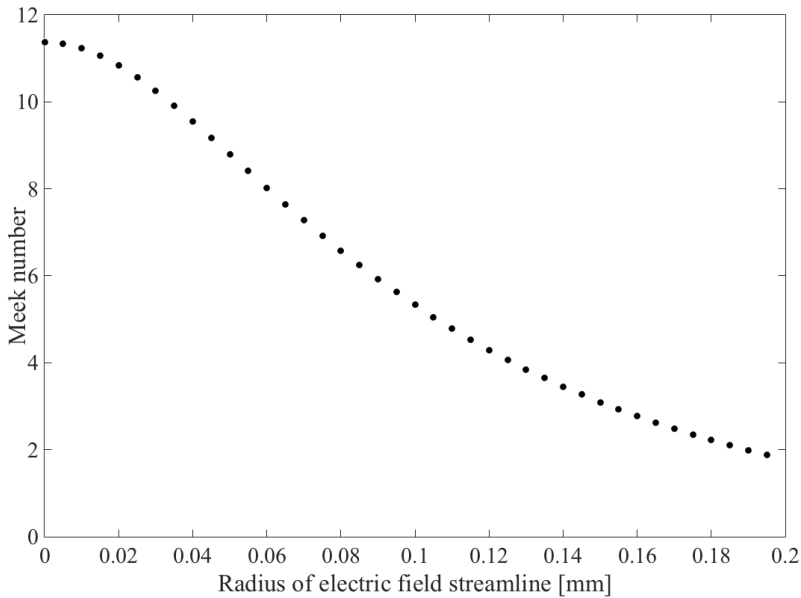


Figure 7.5: The Meek number $\int_0^{s(\alpha=0)} \alpha ds$ for different field lines as a function of their distance from the z axis to the field line (defined at $z = 0$). These calculations are based on the example used in chapter 6 for lightning inception, see figure 7.1.

and calculated along the electric field lines.

In figure 7.6 we show an example that illustrates the compression of electric field lines. In this example, the dielectric is the ellipsoidal ice particle used in chapter 6 for lightning inception (see figure 7.1). The electric field lines indicated in figure 7.6 starting at the bottom are compressed at the tip of the dielectric by about a factor of 2 within the plotted cross-section plane. As a consequence, the density of electrons arriving at the tip is 4 times larger only due to the field line convergence, because the area scales as the radius squared.

7.2 Role of photoionization in discharge inception

7.2.1 Time-dependent simulations in constant field approximation

In air (next to electron impact ionization) photoionization also contributes to the charge buildup next to the tip of the dielectric. In the example with an ice particle in chapter 6, photoionization turned out to be crucial for discharge inception.

In figure 7.7² we show the ion density at the tip of the dielectric as a function of time during the avalanche phase of the discharge as the space charge is not strong enough to

²The dots in figure 7.7 show the output points, not the actual time steps, which are much smaller.

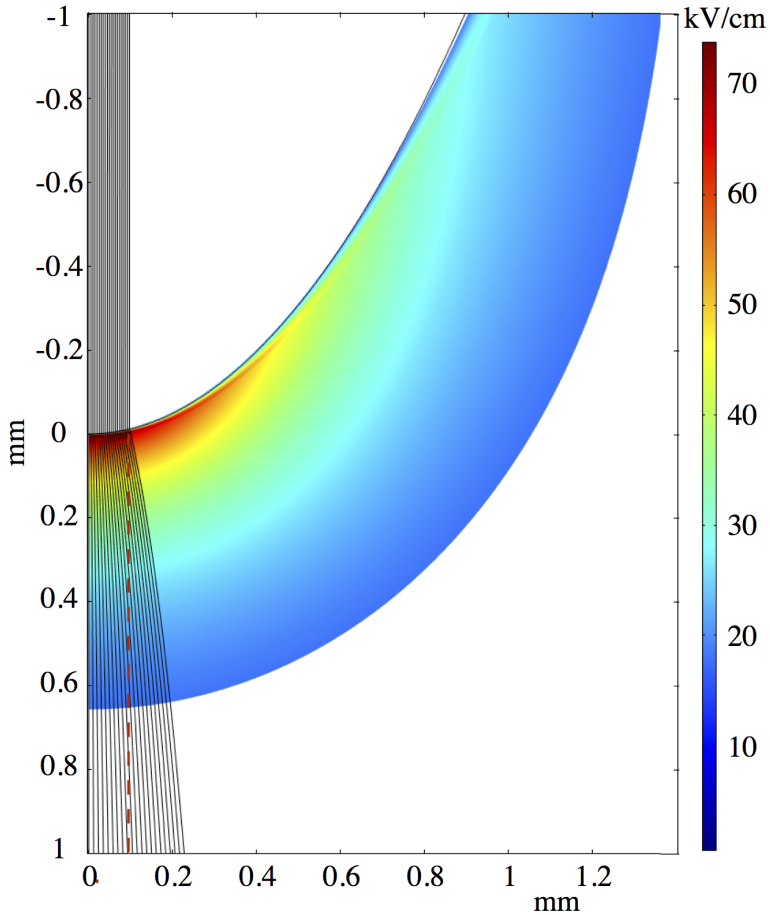


Figure 7.6: An example that illustrates the convergence of the electric field lines at the tip of the dielectric in the background electric field of 2.7 kV/cm. In this example, the dielectric is the ellipsoidal ice particle used in chapter 6 for lightning inception (see figure 7.1). The color code is given only for the electric field above breakdown where $\alpha > 0$. See also figure 7.1 for the electric field on the z axis. The dashed line is given to indicate electric field line convergence.

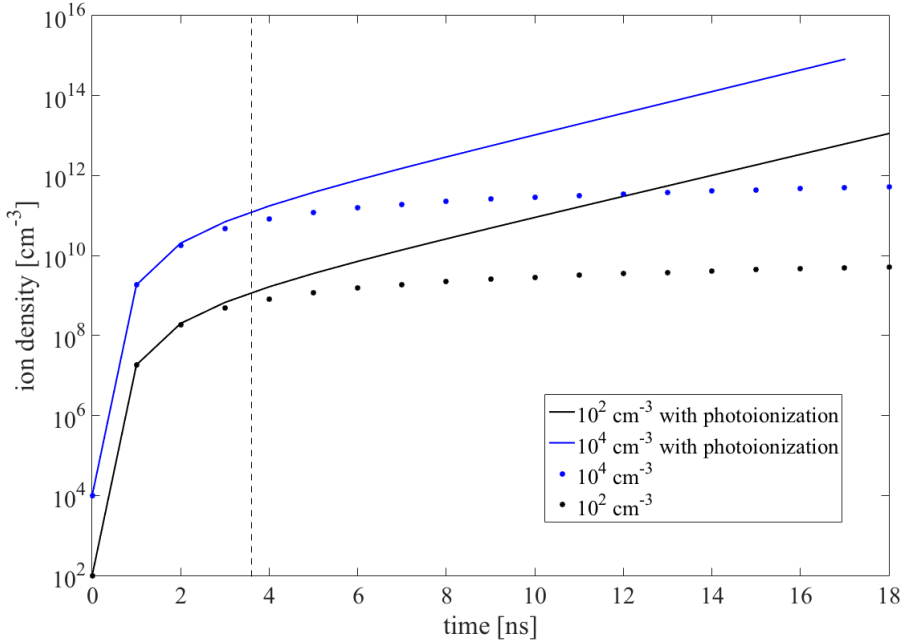


Figure 7.7: Density of positive ions at the tip of the dielectric in the avalanche phase as a function of time. These simulations were performed under the assumption that the electric field does not change in the avalanche phase of the discharge. The black and blue solid lines show the ion density when photoionization was included and the initial background ionization was 10^2 cm^{-3} and 10^4 cm^{-3} , respectively. The black and blue circles show the ion density when photoionization was switched off and the initial background ionization was 10^2 cm^{-3} and 10^4 cm^{-3} , respectively. The vertical dashed line shows the time it takes for an avalanche that starts precisely at the point $z(\alpha = 0)$ to reach the tip of the dielectric.

change the electric field. Here we considered cases with different levels of initial background ionization (of electrons and positive ions) with and without photoionization.

Without photoionization the ion density at the tip grows very fast at the beginning and then drastically slows down. The fast growth can be attributed to impact ionization that takes place in the nearest vicinity of the tip. The slow growth can be explained with electron avalanches coming from afar. After the avalanche that starts at the point where $\alpha = 0$ reaches the dielectric (see dashed line, also in figure 6.6), the charge growth slows down, because the multiplication factor decreases for avalanches coming from afar, see figure 7.2. Besides, it takes longer for those avalanches to reach the dielectric, as can be seen in figure 7.3. When photoionization is included the charge growth at the beginning is not affected, but later the charge buildup does not slow down and continues to grow exponentially.

7.3 Influence of the dielectric permittivity on streamer inception

The ionization integral as given by equation (7.8) is strongly dependent on α , which in turn depends on the electric field. In the inception phase before the avalanche to streamer transition, the background electric field is hardly disturbed by the charges in an electron avalanche. Therefore, the electric field is determined by the dielectric permittivity $\epsilon(\omega = 0)$ together with the background field. In other words, the Meek number is not sensitive to the frequency dependence of the dielectric permittivity, but it is very sensitive to the actual value of the dielectric permittivity at static fields. This is illustrated in figure 7.8 where we show the Meek number $\int \alpha dz$ on the symmetry axis for the setup described in chapter 6 (see also figure 7.1) as a function of $\epsilon'(\omega = 0)$.

Interestingly, figure 7.8 demonstrates that approximating the dielectric (made of ice with the dielectric permittivity $\epsilon = 93$) as a conductor is wrong. The Meek number for $\epsilon = 93$ is about 10, whereas for $\epsilon = 500$ it is 20 at 2.7 kV/cm and still rising.

Unlike in inception phase, in the streamer phase the dependence of the dielectric permittivity on frequency can matter a lot. The characteristic time scale of streamer discharge development is tens of nanoseconds in STP air. On such a short time scale many dielectrics respond to a changing electric field with a smaller dielectric permittivity than to a static electric field. The effect of the frequency dependent dielectric permittivity can be important, for example, for inception of streamer discharges from ice particles in thunderclouds (for illustration see chapter 6).

7.4 Conclusions

We analyzed the development of an electron avalanche before its transition to a positive streamer on the basis of the ionization integral (the Meek number). We point out that positive streamers have multi-avalanche origin when they start from a distribution of electrons, which is in accordance with the experiments [11]. Due to the multi-avalanche

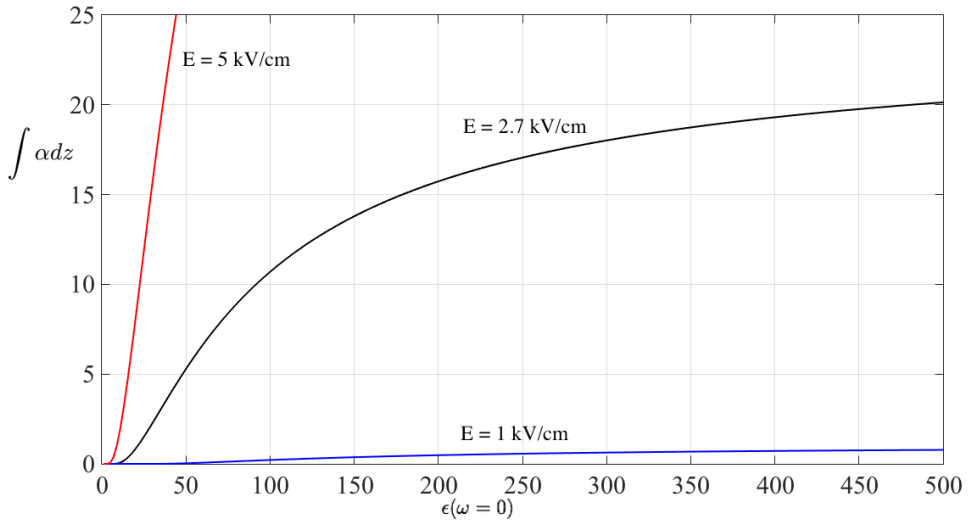


Figure 7.8: The Meek number $\int \alpha dz$, calculated on the z axis underneath a dielectric body, is plotted as a function of the dielectric constant for a constant (sub-breakdown) background electric field of 1 kV/cm, 2.7 kV/cm, and 5 kV/cm. An electron avalanche is considered under the same conditions as described in chapter 6 (see also figure 7.1).

streamer formation, the Meek number as defined by equation (7.8) can be much smaller than 18 to 20, as given by the Meek criterion for negative streamer inception, and yet enough for avalanche to positive streamer transition, as already observed (but not explained) in chapter 6.

Photoionization appears to play a decisive role in streamer inception in air at the tip of a dielectric or conductive body in sub-breakdown fields. It produces free electrons some distance away from the tip and new secondary avalanches can develop. This feedback mechanism is similar to the one proposed in [134] for a self-sustained corona discharge.

Chapter 8

Propagation of a positive streamer toward a dielectric tip in pure nitrogen and in air under voltage pulses with sub-nanosecond rise time

We study positive streamer propagation from an electrode (a plate with a pin protruding from it) towards a dielectric tip (for example, the tip of a dielectric rod). We compare streamer behavior in artificial air and in pure nitrogen at 250 mbar under a voltage pulse with a sub-nanosecond rise time. Such voltage switches are being developed nowadays [135]. During such a short rise-time, electrons of the background ionization drift towards to the anode leaving a depleted area behind, which is avoided by positive streamers in pure nitrogen, because there are no sources of free electrons (e.g., due to cosmic rays) that could fill that area. In air there is photoionization, which produces free electrons non-locally, and thus replenishes the free electrons in the depleted area. Therefore, in air a positive streamer reaches the dielectric tip, whereas in nitrogen, it does not.

8.1 Introduction

Recently, it has been suggested that plasmas produced by very short nanosecond high-voltage pulses can be very efficient, for example for air purification [136, 137]. For these applications, it is beneficial to have the voltage pulse rising as fast as possible. Nowadays, it is possible to make pulse generators with 200 picosecond rise time [138]. Within such a short time free electrons move only tens of microns, which means that the spatial distribution of electrons is hardly disturbed before the discharge. In simulations, this can be approximated by an instantaneously applied electric field. When the voltage rises slowly, electrons of the background ionization move and some reactions can take place, such as detachment [111]. Therefore, it is reasonable to expect that different mechanisms become important for setups with a voltage rising on a sub-nanosecond time scale, which we discuss in this chapter.

In this study we designed a somewhat artificial setup, which can be realized in experiments, in which a positive streamer interacts with the tip of a dielectric at a voltage that is applied instantaneously. Essentially, a positive streamer propagates in a cylindrically symmetric vessel from a pin electrode down toward a dielectric tip (the dielectric permittivity is 5) in a gas at 250 mbar and 300 K. The electrode (black areas in figures 1 and 2) and dielectric (white areas) are parametrized as spheroids, but any other shape could be chosen as well. The radii of the electrode and dielectric tip are 1.5 and 2 mm, respectively, and their length is 4 mm. The size of the simulation domain is 5 mm by 12 mm. The bottom of the domain is grounded and to the top with the pin protruding from it, a voltage of 10 kV is applied instantaneously.

8.2 Modeling

In our simulations, we use the convection-diffusion-reaction model in local field approximation [139] (see chapter 4 for an extended description of the model). The ions are assumed immobile on the timescale of interest. The electrons can drift in an external electric field, diffuse, and ionize an ambient gas due to impact ionization (and due to photoionization in air). Once an electron reaches a dielectric surface, we assume that it stays there building up a surface charge and no electron emission from the dielectric surface. The transport equations are coupled to the Poisson equation, which is solved in the whole simulation domain, including the electrode and dielectric. The Ghost Fluid Method is implemented to discretize the Poisson equation near dielectric or conductive interfaces [57]. In the radial direction, we assume Neumann boundary conditions.

In figures 8.1 and 8.2, we zoom into the area of the streamer propagation. The streamer is launched by placing an electrically neutral Gaussian plasma seed of 0.5 mm radius and $4 \cdot 10^7 \text{ cm}^{-3}$ maximal density at the tip of the electrode. For their propagation, positive streamers, unlike negative streamers, need a source of free electrons

In this configuration of the electric field, there is hardly any space charge, although some electrons can reach the dielectric tip due to diffusion.

ahead of the streamer. In pure nitrogen, this source could be, for example, leftover pre-ionization in repetitive discharges. In our simulations, the value of the initial electron and ion density is 10^4 cm^{-3} , which corresponds to a discharge repetition frequency [95] of 0.3 Hz. In air, the main source of free electrons is photoionization, whereas in 100% pure nitrogen, which we consider here, photoionization is absent. Photoionization is an intrinsically nonlocal effect continuously providing free electrons ahead of the streamer. It works as follows: an excited nitrogen molecule emits a UV photon in the 98 to 102.5 nm range, which is *elsewhere* absorbed by an oxygen molecule with emission of a free electron (see subsection 4.2.4 in chapter 4). Photoionization is implemented according to Zheleznyak's model [93] using the computational approximations of [94].

8.3 Results

In figures 8.1 and 8.2, we show the evolution of the electric field strength and the decimal logarithm of the electron density in an axial cross section. In pure nitrogen (figure 8.1), the electrons of the pre-ionization drift upwards in the external electric field depleting an area above the dielectric tip. It has the shape of the dielectric tip and it is about 2 mm thick. The area is depleted independently of the actual pre-ionization level. Positive streamers cannot penetrate into such areas. The streamer in figure 8.1, therefore, cannot reach the dielectric tip. A similar effect was observed in recent experiments [140]. There, it was shown that weak pre-ionization, which does not influence the electric field, can guide positive streamers in nitrogen in directions perpendicular to the electric field lines. In air (figure 8.2), UV photons released by excited nitrogen molecules can ionize oxygen molecules and continuously provide free electrons ahead of the streamer contributing to the background ionization. The streamer can now propagate all the way to the dielectric tip, touch it, and move around it.

8.4 Conclusions

In conclusion, we expect to observe electron-depleted regions that are avoided by positive discharges provided photoionization is negligible, surface electron emission during the voltage pulse is negligible, and voltage rises fast enough to neglect liberation of electrons in the depleted area (e.g., due to cosmic rays). With sub-nanosecond voltage being achievable, such conditions are more likely to be met in experiments.

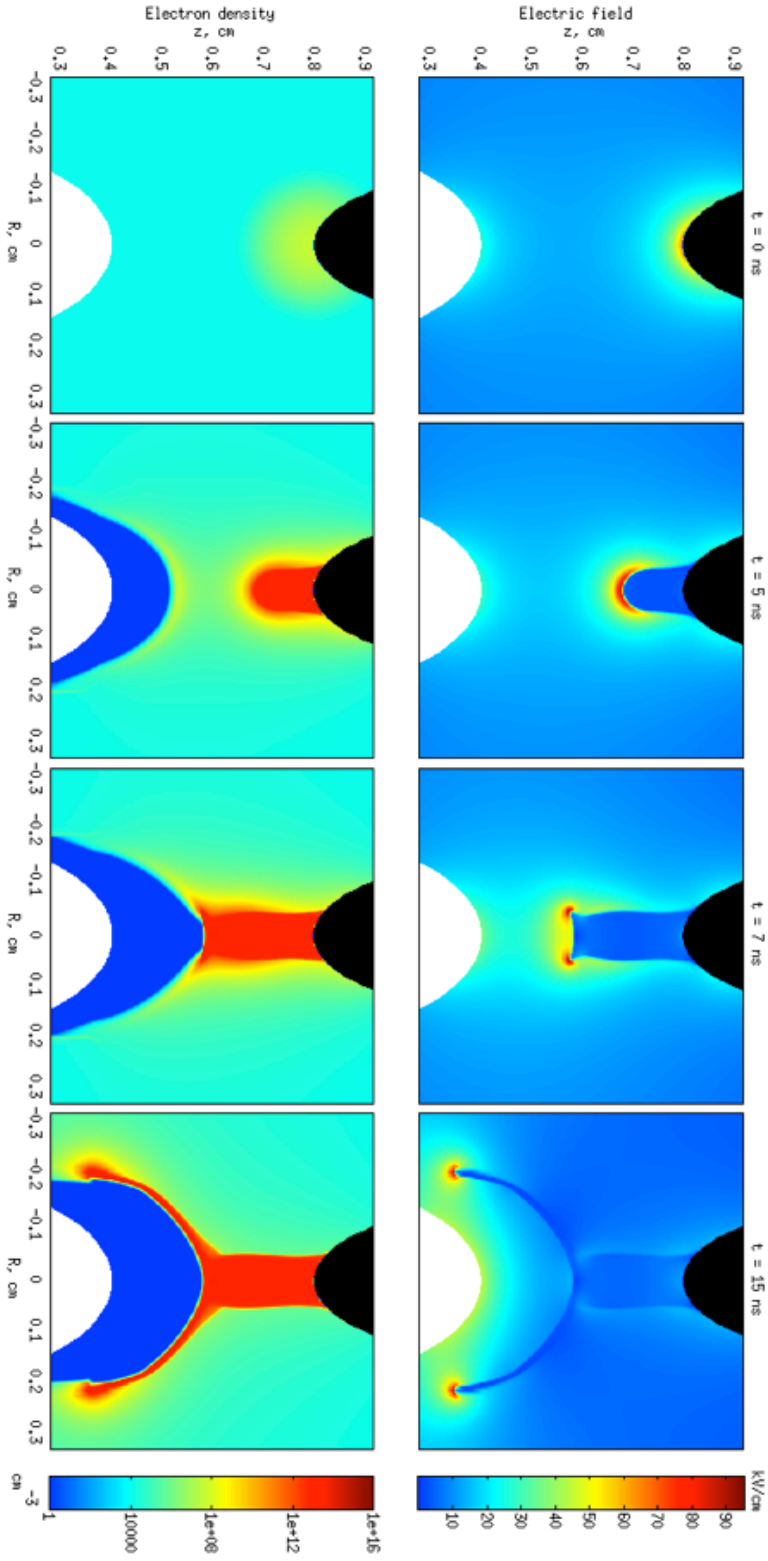


Figure 8.1: Propagation of a positive streamer in pure nitrogen from an electrode (shown in black) towards a dielectric tip (shown in white). Evolution of the electric field strength (upper panels) and of the logarithm of the electron density (lower panels). The electrons of the pre-ionization drift upwards in the external electric field depleting the area above the dielectric tip (shown in blue). Positive streamers in pure nitrogen avoid electron-free areas. The streamer does not reach the dielectric tip but surrounds the depleted area.

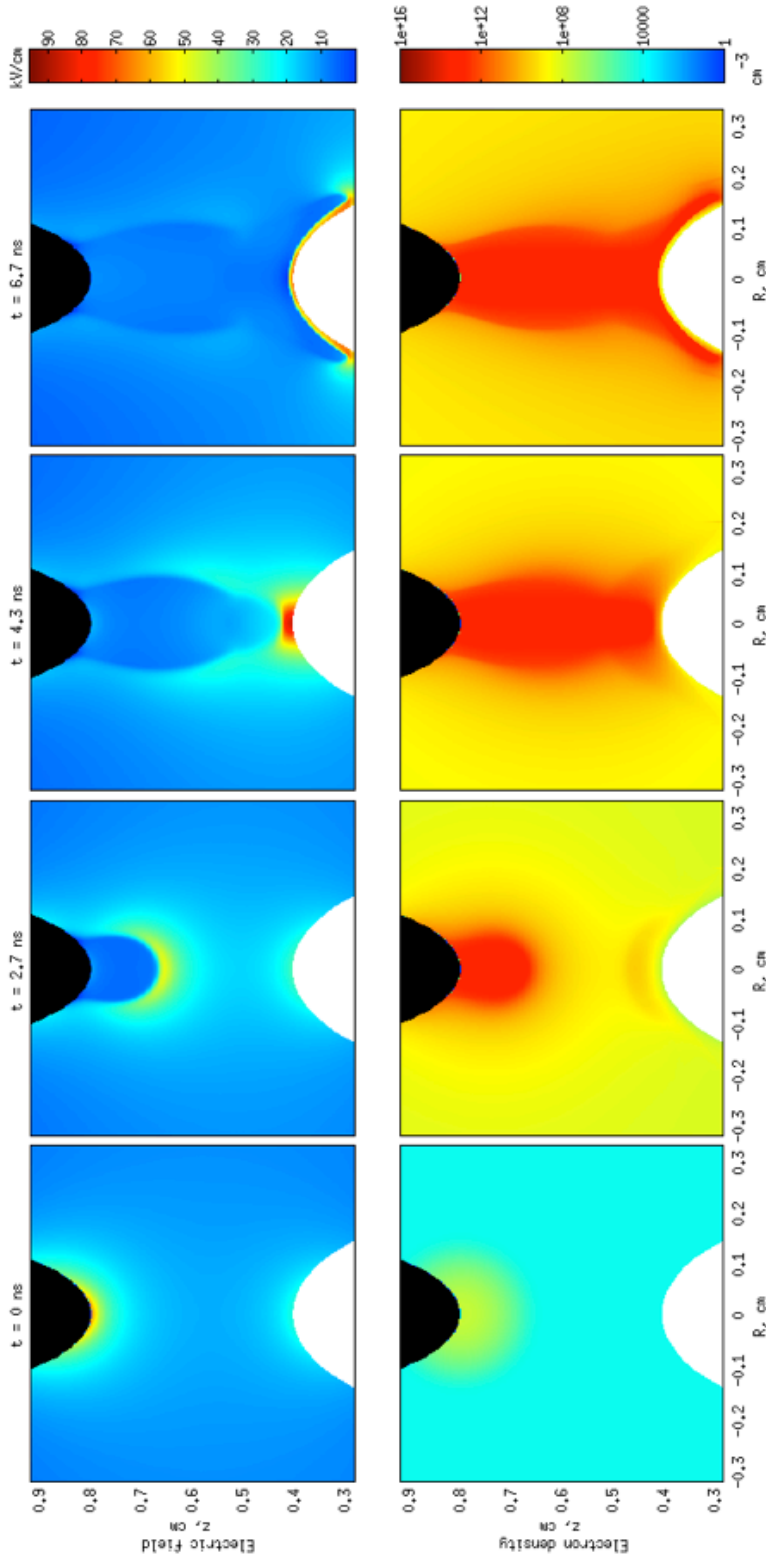


Figure 8.2: The same situation, but now in air. Due to photoionization, the discharge continuously produces free electrons in front of the streamer head. Therefore, the streamer can propagate all the way to the dielectric tip, touch it and move along it. The layer of high electric field around the tip of the dielectric after 6.7 ns forms when the space charge of the streamer head hits the top of the dielectric. In this layer, the electrons drift in the electric field leaving the positive ions with their space charge behind.

Chapter 9

An alternative approach to calculating photoionization and photoemission

We introduce an alternative approach to calculating numerically volume integrals of the type

$$G(\mathbf{r}, \lambda; g) = \int \frac{g(\mathbf{r}') \exp(-\lambda|\mathbf{r}' - \mathbf{r}|)}{4\pi|\mathbf{r} - \mathbf{r}'|^3} d^3r',$$

where λ can be interpreted as the inverse absorption length of a photon, $\exp(-\lambda|\mathbf{r}' - \mathbf{r}|)$ is an absorption function, and $g(\mathbf{r})$ is the source of photons. Integrals of that type describe, for example, photoionization in $\text{N}_2:\text{O}_2$ gas mixtures and photon flux onto a surface, but they might also be encountered in applications beyond discharge physics. Our new approach is based on the idea of considering λ as another variable. We perform differentiation with respect to λ in order to reduce the integral to a superposition of Green's functions of Helmholtz equations, which can be solved with efficient Poisson solvers. The approach also gives the flexibility to choose a numerical scheme that suits the required accuracy of the problem. Past approaches based on numerical solutions of Helmholtz equations are applicable to air, but they are questionable in nitrogen.

9.1 Introduction

Here we consider integrals of the type

$$G(\mathbf{r}, \lambda; g) = \int \frac{g(\mathbf{r}') \exp(-\lambda|\mathbf{r}' - \mathbf{r}|)}{4\pi|\mathbf{r} - \mathbf{r}'|^3} d^3r', \quad (9.1)$$

because they appear in numerical calculations of photoionization and photoemission, but possibly also in other problems in the physics of gaseous discharges. Photoionization and photoemission are often bottlenecks in streamer discharge simulations. The appearance of such integrals is discussed in section 9.3. When the source $g(\mathbf{r})$ is extended over a large volume in space, the direct integration can be costly, especially when the value of the integral has to be updated multiple times in a simulation, which is the case in streamer discharge simulations.

Approaches alternative to direct integration of photoionization in air by solving a number of Helmholtz equations have been proposed by Bourdon *et al.* (2007) [141] and Luque *et al.* (2007) [94]. Those methods use numerical fitting that works well for photoionization in air. Luque *et al.* (2007) also suggested that the fitting can be applied to other nitrogen-oxygen mixtures. However applying it to high purity nitrogen as done, for example, in [142] is beyond the range of validity. Bourdon *et al.* (2007) tested their numerical fitting only in air, but the scaling with oxygen pressure suggests that the fitting should also work for oxygen pressures different from air. In this chapter we show that using methods by Bourdon *et al.* (2007) and Luque *et al.* (2007) in highly pure nitrogen, such as nitrogen with 1 ppm oxygen, introduces a large error. We have not tested, however, how sensitive the results of streamer simulations in pure nitrogen would be to such a numerical error.

Another method of calculating photon transport based on the monochromatic radiative transfer equation is proposed in [32]. The method is more general, but it is nontrivial to apply to a given problem.

9.2 Description of the approach

9.2.1 Analytical reformulation

In equation (9.1), λ is always a non-negative parameter. Let us take the second partial derivative of $G(\mathbf{r}, \lambda; g)$ with respect to λ . We arrive at the following equation

$$w(\mathbf{r}, \lambda) = \frac{\partial^2 G(\mathbf{r}, \lambda; g)}{\partial \lambda^2} = \int_{r'} \frac{g(\mathbf{r}') \exp(-\lambda|\mathbf{r} - \mathbf{r}'|)}{4\pi|\mathbf{r} - \mathbf{r}'|} d^3r'. \quad (9.2)$$

The function $w(\mathbf{r}, \lambda)$ has the shape of a Yukawa (or screened Poisson) potential, which exactly satisfies the Helmholtz equation [143] with the solution equal to zero on infinitely far boundaries:

$$\Delta w - \lambda^2 w = -g(\mathbf{r}), \quad (9.3)$$

$$w(\mathbf{r}) = 0, \text{ for } |\mathbf{r}| \rightarrow \infty, \quad (9.4)$$

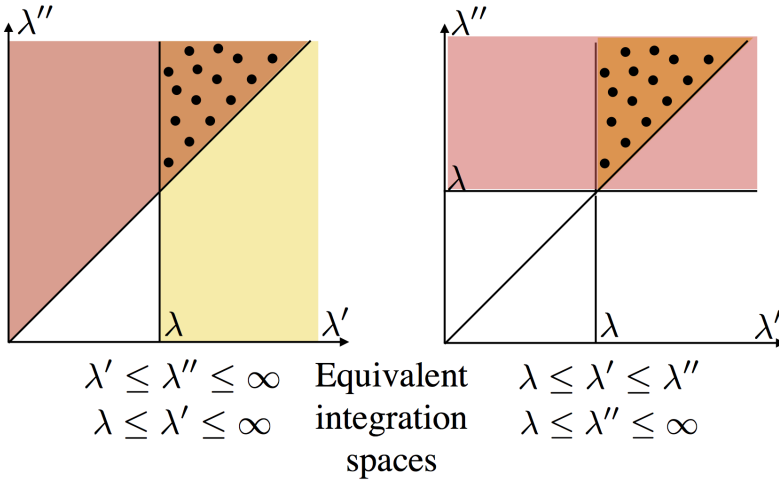


Figure 9.1: Equivalent integration spaces for equation (9.5), which shows the possibility to reduce the double integral to a single integral in equation (9.6) by replacing the limits of integration.

and assuming that $g(\mathbf{r})$ is localized or decays sufficiently rapidly.

To retrieve the function $G(\mathbf{r}, \lambda; g)$, we need to perform the integration with respect to λ

$$G(\mathbf{r}, \lambda; g) = \int_{\lambda}^{\infty} d\lambda' \int_{\lambda'}^{\infty} d\lambda'' w(\mathbf{r}, \lambda''), \quad (9.5)$$

which can be reduced to a single integral as follows

$$\begin{aligned} G(\mathbf{r}, \lambda; g) &= \int_{\lambda}^{\infty} d\lambda' \int_{\lambda'}^{\infty} d\lambda'' w(\mathbf{r}, \lambda'') = \int_{\lambda}^{\infty} \int_{\lambda}^{\infty} \Theta(\lambda'' - \lambda') w(\mathbf{r}, \lambda'') d\lambda' d\lambda'' \\ &= \int_{\lambda}^{\infty} (\lambda'' - \lambda) w(\mathbf{r}, \lambda'') d\lambda'', \end{aligned} \quad (9.6)$$

where Θ is the Heaviside step function. This can be also seen from figure 9.1 where we show the equivalent integration spaces.

9.2.2 Remarks on numerical implementation

In principle, one needs to solve the Helmholtz equation (9.3) for an infinite range of λ in order to calculate the precise value of $G(\mathbf{r}, \lambda; g)$. However, we will demonstrate that a reasonable accuracy can be achieved with solving only a few Helmholtz equations for a number of reference values of λ by applying a numerical quadrature rule, such as the trapezoidal or Simpson's rule.

The virtual absorption function $\exp(-\lambda|\mathbf{r}' - \mathbf{r}|)$ (for given \mathbf{r}' and \mathbf{r}) adds only an exponential decay to the function in the integral in equation (9.1). Let us perform an

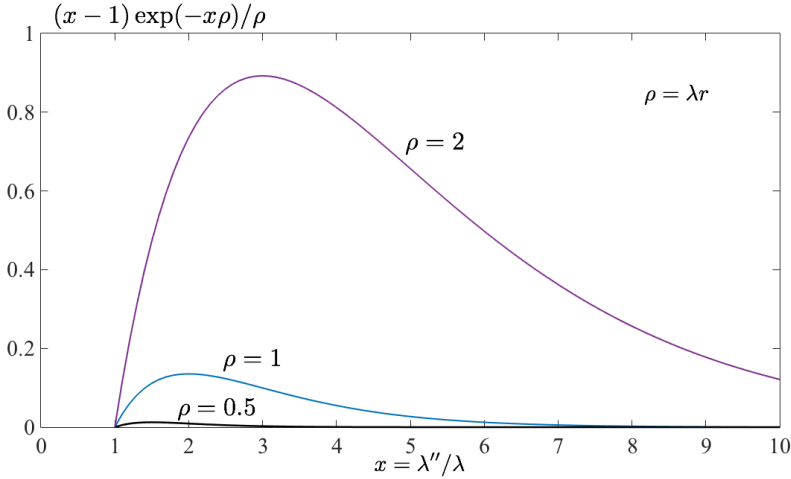


Figure 9.2: The function $4\pi\lambda^2(\lambda'' - \lambda)w(\lambda'') \equiv (x - 1) \exp(-x\rho)/\rho$ as a function of $x = \lambda''/\lambda$ when $g(\mathbf{r}') = \delta(\mathbf{r}')$. The position of the maximum is at $x = (1 + \rho)/\rho$, and the value of the maximum is $\exp(-1 - \rho)/\rho^2$. Here, $\rho = \lambda r$.

asymptotic analysis of the function in the integral in equation (9.6). For λ'' close to λ , the function $(\lambda'' - \lambda)w(\lambda'')$ (as a function of λ'') linearly approaches 0. For very large values of λ'' , the function is exponentially small. The function $(\lambda'' - \lambda)w(\lambda'')$ has one maximum, and its position and width depend on the length scales in a given problem.

For the simple case $g(\mathbf{r}) = \delta(\mathbf{r})$ we have $w(\lambda'') = \exp(-\lambda''r)/4\pi r$, as it is the Green's function of the screened Poisson equation. For this case, we introduce the dimensionless units: $x = \lambda''/\lambda$ and $\rho = \lambda r$ and we plot the function $4\pi\lambda^2(\lambda'' - \lambda)w(\lambda'') \equiv (x - 1) \exp(-x\rho)/\rho$ in figure (9.2) for some values of ρ for $g(\mathbf{r}) = \delta(\mathbf{r})$. That function has a smooth shape with a single maximum and therefore it can be numerically integrated with only a few integration terms.

Essentially, to compute $G(\mathbf{r}, \lambda)$, we use equation 9.6. There, the integration over the interval $[\lambda, \infty)$ will be replaced by a numerical quadrature rule for which $w(\mathbf{r}, \lambda)$ is to be computed for a (modest) number of different λ'' values.

The optimal integration scheme and the number of Helmholtz equations needed to be solved in order to achieve a given accuracy depends on the characteristic length scales in a problem of interest and on the required accuracy. Up to now, we have not simplified the problem and we leave the choice of a numerical scheme open, which essentially offers accuracy control.

We would like to point out that Helmholtz equations can be solved completely in parallel, which can boost the performance. The method also scales better with the increasing number of grid points than the direct integration. For example, for a photon flux onto a surface in full 3D, direct integration would scale as N^5 and for photoionization it would scale as N^6 , whereas our method would scale as roughly N^3 (scaling of the Helmholtz solver in 3D).

There are also multiple tools to solve Helmholtz equations. In streamer discharge modeling the calculation of photoionization and photon fluxes onto a surface is accompanied with calculations of the electrical potential with a Poisson solver. A lot of effort is usually dedicated into developing an efficient Poisson solver and if there is one available, it can also be used for calculating photoionization and photon flux onto a surface.

9.3 Appearance of $G(\mathbf{r}, \lambda; g)$ in discharge physics

9.3.1 Example 1: Photoionization in $\text{N}_2:\text{O}_2$ gas mixtures

The volume absorption of photons $S_{\text{ph}}(\mathbf{r})$ is characterized by an absorption function $f(|\mathbf{r} - \mathbf{r}'|)$, where \mathbf{r} is the location of the photon absorption and \mathbf{r}' is the location of the photon source, and it is given by

$$S_{\text{ph}}(\mathbf{r}) = \int \frac{g(\mathbf{r}')f(|\mathbf{r}' - \mathbf{r}|)}{4\pi|\mathbf{r} - \mathbf{r}'|^2} d^3r', \quad (9.7)$$

where $g(\mathbf{r}')$ is the photon source [93]. Photoionization in air and other $\text{N}_2:\text{O}_2$ mixtures is a special case of radiation with the specific absorption function $f(r)$:

$$f(r) = \frac{\exp(-\lambda_0 r) - \exp(-\lambda_1 r)}{r \ln(\lambda_1/\lambda_0)}, \quad (9.8)$$

where $\lambda_0 = 0.035p_{\text{O}_2} \text{ cm}^{-1}$ and $\lambda_1 = 2p_{\text{O}_2} \text{ cm}^{-1}$, and p_{O_2} is the partial pressure of molecular oxygen, which is 150 Torr in air at STP. Such an absorption function is chosen to approximate the absorption spectrum in air, with the photon wavelengths uniformly distributed between 98 nm and 102.5 nm.

For this absorption function, Zheleznyak's integral of photoionization [93] reads

$$S_{\text{ph}}(\mathbf{r}) = \frac{1}{\ln(\lambda_1/\lambda_0)} \int \frac{I(\mathbf{r}')(\exp(-\lambda_0|\mathbf{r} - \mathbf{r}'|) - \exp(-\lambda_1|\mathbf{r} - \mathbf{r}'|))}{4\pi|\mathbf{r} - \mathbf{r}'|^3} d^3r', \quad (9.9)$$

where $I(\mathbf{r}')$ is the photon source. This integral can be expressed as a sum of two integrals given by equation (9.1):

$$S_{\text{ph}}(\mathbf{r}) = \frac{G(\mathbf{r}, \lambda_0; I) - G(\mathbf{r}, \lambda_1; I)}{\ln(\lambda_1/\lambda_0)}. \quad (9.10)$$

9.3.2 Example 2: Photon flux onto a surface

Now let us consider a monochromatic photon flux onto a surface with a normal vector $\mathbf{n}(\mathbf{r})$. We assume that the photons move isotropically with infinite velocity and get absorbed in a gas with an absorption length $1/\lambda_{\text{abs}}$ ($\lambda_{\text{abs}} = 0$ in case of no absorption). Then the flux is given by

$$S_{\text{pe}}(\mathbf{r}) = \int \frac{I(\mathbf{r}') \exp(-\lambda_{\text{abs}}|\mathbf{r}' - \mathbf{r}|)}{4\pi|\mathbf{r} - \mathbf{r}'|^2} \frac{\mathbf{n} \cdot (\mathbf{r} - \mathbf{r}')}{|\mathbf{r} - \mathbf{r}'|} d^3r', \quad (9.11)$$

where the factor $\mathbf{n} \cdot (\mathbf{r} - \mathbf{r}')/|\mathbf{r} - \mathbf{r}'|$ in the integral accounts for the cosine of the incidence angle with respect to the normal vector \mathbf{n} at the surface point \mathbf{r} .

Equation (9.11) can be rewritten in a more explicit way. Let us choose, for example, Cartesian coordinates:

$$S_{\text{pe}}(\mathbf{r}) = \mathbf{n} \cdot \mathbf{r} \int \frac{I(\mathbf{r}') \exp(\lambda_{\text{abs}}|\mathbf{r} - \mathbf{r}'|)}{4\pi|\mathbf{r} - \mathbf{r}'|^3} d^3r' - \sum_{i=1}^3 n_i(\mathbf{r}) \int \frac{I(\mathbf{r}')r'_i \exp(-\lambda_{\text{abs}}|\mathbf{r} - \mathbf{r}'|)}{4\pi|\mathbf{r} - \mathbf{r}'|^3} d^3r', \quad (9.12)$$

where $\mathbf{r} = (r_1, r_2, r_3)$ and $\mathbf{n} = (n_1(\mathbf{r}), n_2(\mathbf{r}), n_3(\mathbf{r}))$. In terms of integrals of the type (9.1), equation (9.12) reads

$$S_{\text{pe}}(\mathbf{r}) = \mathbf{n} \cdot \mathbf{r} G(\mathbf{r}, \lambda_{\text{abs}}; I) - \sum_{i=1}^3 n_i(\mathbf{r}) G(\mathbf{r}, \lambda_{\text{abs}}; I(\mathbf{r}')r'_i), \quad (9.13)$$

It is clear that if we have an efficient approach to calculate the integral given by equation (9.1), we can efficiently calculate photoionization and photon flux onto a surface. The latter is relevant for calculating photoemission.

9.4 Comparison with other models for calculating photoionization in air and pure nitrogen

Now let us compare our approach with the methods by Luque et al (2007) [94] and Bourdon et al (2007) [141] for calculating photoionization in air and in nitrogen with 1 ppm admixture of oxygen as given by equation (9.9).

9.4.1 Analytical solution for a point photon source

Let us assume that $g(\mathbf{r}') = \delta(\mathbf{r}')$ in equation (9.9). Then, the photoionization source is given by

$$S_{\text{ph}}^{\text{zh}}(\mathbf{r}) = \frac{1}{\ln(\lambda_1/\lambda_0)} \frac{\exp(-\lambda_0 r) - \exp(-\lambda_1 r)}{4\pi r^3}. \quad (9.14)$$

If correctly numerically implemented, our approach will reproduce this result.

9.4.2 Approximation by Bourdon et al (2007) for a point photon source

Bourdon et al (2007) suggested using the following three-term approximation

$$\frac{1}{\ln(\lambda_1/\lambda_0)} \frac{\exp(-\lambda_0 R) - \exp(-\lambda_1 R)}{p_{\text{O}_2}^2 R^2} \simeq \sum_{j=1}^3 A_j \exp(-\lambda_j p_{\text{O}_2} R), \quad (9.15)$$

where $R = |\mathbf{r} - \mathbf{r}'|$, $A_1 = 1.986 \times 10^{-4} \text{ Torr}^{-2}\text{cm}^{-2}$, $A_2 = 0.0051 \text{ Torr}^{-2}\text{cm}^{-2}$, $A_3 = 0.4886 \text{ Torr}^{-2}\text{cm}^{-2}$. And, respectively, $\lambda_1 = 0.0553 \text{ Torr}^{-1}\text{cm}^{-1}$, $\lambda_2 = 0.146 \text{ Torr}^{-1}\text{cm}^{-1}$, $\lambda_3 = 0.89 \text{ Torr}^{-1}\text{cm}^{-1}$.

In case $g(\mathbf{r}') = \delta(\mathbf{r}')$, the photoionization source in equation (9.9) calculated with the approximation equation (9.15) is given by

$$S_{\text{ph}}^{\text{b}}(\mathbf{r}) = \frac{p_{\text{O}_2}^2}{4\pi r} \sum_{j=1}^3 A_j \exp(-\lambda_j p_{\text{O}_2} r). \quad (9.16)$$

9.4.3 Approximation by Luque et al (2007) for a point photon source

A similar two-term approximation was proposed by Luque et al (2007). It reads

$$\frac{1}{\ln(\lambda_1/\lambda_0)} \frac{\exp(-\lambda_0 R) - \exp(-\lambda_1 R)}{R^2} \quad (9.17)$$

$$\simeq A_1 \exp(-\lambda_1 p[\text{O}_2]R) + A_2 \exp(-\lambda_2 p[\text{O}_2]R),$$

where p is pressure in Torr, $[\text{O}_2]$ is the oxygen content, $A_1 = 6 \cdot 10^{-5} \text{ Torr}^{-2}\text{cm}^{-2}$, $A_2 = 3.55 \cdot 10^{-6} \text{ Torr}^{-2}\text{cm}^{-2}$. And, respectively, $\lambda_1 = 0.059 \text{ Torr}^{-1}\text{cm}^{-1}$, $\lambda_2 = 0.01 \text{ Torr}^{-1}\text{cm}^{-1}$. And the photoionization source in equation (9.9) when $g(\mathbf{r}') = \delta(\mathbf{r}')$ is given by

$$S_{\text{ph}}^{\text{l}}(\mathbf{r}) = \frac{p_{\text{O}_2}^2}{r} (A_1 \exp(-\lambda_1 p[\text{O}_2]r) + A_2 \exp(-\lambda_2 p[\text{O}_2]r)). \quad (9.18)$$

The approximation in equation (9.17) gives a wrong algebraic decay, which can be tolerated for $\lambda r \gg 1$. For small distances electron impact ionization is stronger than photoionization. Therefore, the approximation is acceptable in air.

9.4.4 Numerical implementation of our approach in air

Applying our approach to equation (9.9), we get

$$S_{\text{ph}}^{\text{our}}(\mathbf{r}) = \frac{1}{\ln(\lambda_1/\lambda_0)} \left[\int_{\lambda_0}^{\infty} (\lambda - \lambda_0) w(\lambda) d\lambda - \int_{\lambda_1}^{\infty} (\lambda - \lambda_1) w(\lambda) d\lambda \right], \quad (9.19)$$

where $w(\mathbf{r}, \lambda)$ is the solution of the Helmholtz equation for a point source

$$\Delta w - \lambda^2 w = -\delta(\mathbf{r}). \quad (9.20)$$

The solution of equation (9.20) is its Greens's function:

$$w(\mathbf{r}, \lambda) = \frac{\exp(-\lambda r)}{4\pi r}. \quad (9.21)$$

There are a few typos in [94], but here the correct values are used (see section 4.2.4 in chapter 4).

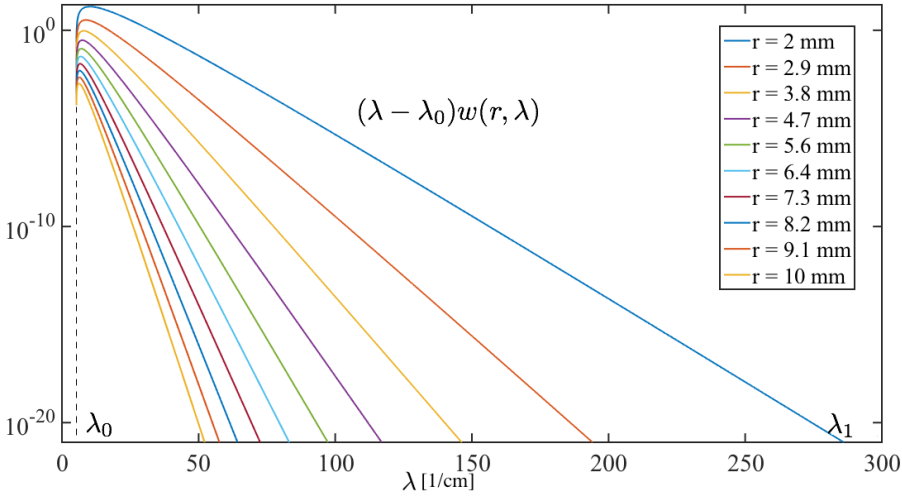


Figure 9.3: The function $(\lambda'' - \lambda_0)w(\lambda'', r)/4\pi$ in air when $g(\mathbf{r}') = \delta(\mathbf{r}')$.

Substituting $w(\mathbf{r}, \lambda)$ into equation (9.19), we arrive at the solution for $S_{\text{ph}}^{\text{our}}(\mathbf{r})$.

Now we ask ourselves the following question. Assuming that we can calculate $w(\mathbf{r}, \lambda)$ exactly for an arbitrary λ , which λ 's do we need to take in order to estimate the integrals in equation (9.19)?

In STP air, $\lambda_0 = 5.25 \text{ cm}^{-1}$ and $\lambda_1 = 300 \text{ cm}^{-1}$ [93] and it can be estimated that the second integral in equation (9.19) is always much smaller than the first integral if the interval of interest is $1 \text{ mm} \leq r \leq 10 \text{ mm}$ (the typical length of interest for streamer simulations in atmospheric air). See figure 9.3:

$$\int_{\lambda_0}^{\infty} (\lambda - \lambda_0)w d\lambda \gg \int_{\lambda_1}^{\infty} (\lambda - \lambda_0)w d\lambda > \int_{\lambda_1}^{\infty} (\lambda - \lambda_1)w d\lambda. \quad (9.22)$$

Since w as a function of λ has an exponential tail, the numerical integration can be truncated for some λ_{cutoff} :

$$S_{\text{ph}}^{\text{our}}(\mathbf{r}) \simeq \frac{1}{\ln(\lambda_1/\lambda_0)} \int_{\lambda_0}^{\lambda_{\text{cutoff}}} (\lambda - \lambda_0)w_0(\lambda) d\lambda. \quad (9.23)$$

From figure 9.3 it is clear that at $\lambda'' = 30/\text{cm}$, the function $(\lambda'' - \lambda_0)w(\lambda'')$ is about ten times smaller than it is at its maximum. Therefore, it is reasonable to take $\lambda_{\text{cutoff}} = 30/\text{cm}$.

Assuming that we know the solution $w(\mathbf{r}, \lambda)$ as given by equation (9.21) with machine precision, let us calculate the integrals in equation (9.23) using the composite Simpson's quadrature rule [144] with N integration terms. For comparison we take $N = 3$ and $N = 11$ terms of $w(\mathbf{r}, \lambda)$.

In STP air, all the considered approaches give results that agree reasonably well with the analytical solution as shown in figure 9.4.

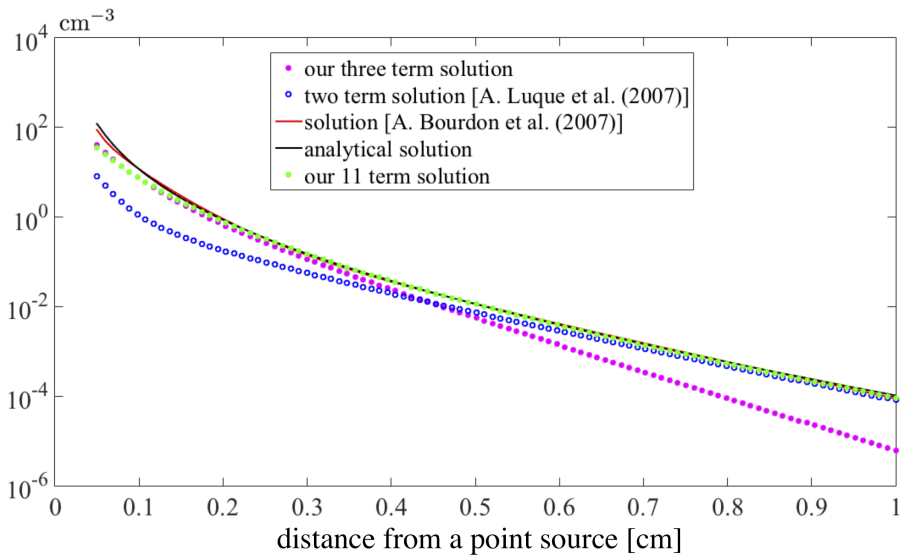


Figure 9.4: The photoionization $S_{\text{ph}}(\mathbf{r})$ in equation (9.9) for a point source $g(\mathbf{r}') = \delta(\mathbf{r}')$ calculated directly and numerically in air at STP. The black solid curve is given by the analytical solution in equation (9.14). The red solid curve (hardly distinguishable from the black solid line) shows the solution given by equation (9.16) (three term approximation). The blue circles show the solution given by equation (9.18) (two term approximation). Our solution with three term approximation is shown with magenta circles, and our solution with 11 term approximation is shown with green circles.

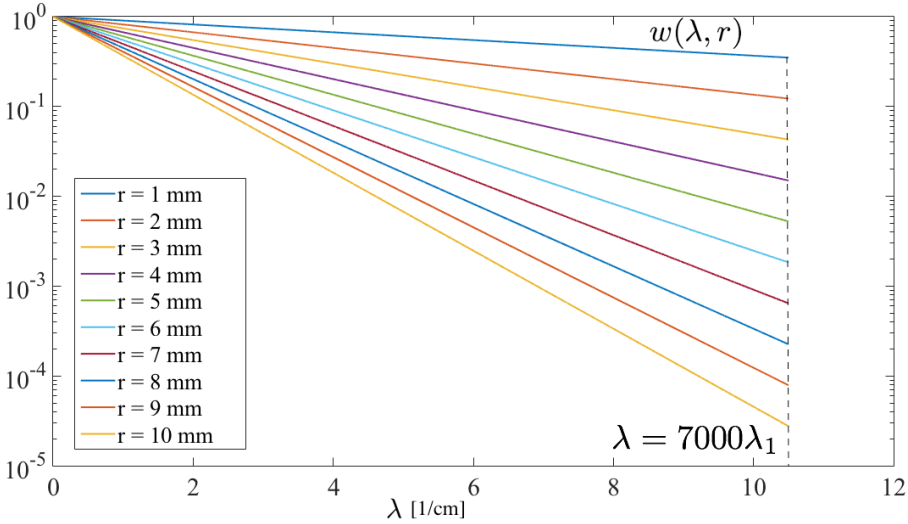


Figure 9.5: The function $w(\lambda'', r)/4\pi$ in nitrogen with 1 ppm oxygen when $g(\mathbf{r}') = \delta(\mathbf{r}')$.

9.4.5 Numerical implementation of our approach in high purity nitrogen (with 1 ppm oxygen).

In pure nitrogen with 1 ppm oxygen, $\lambda_0 = 5.6 \cdot 10^{-5} \text{ cm}^{-1}$ and $\lambda_1 = 0.0015 \text{ cm}^{-1}$. As can be seen in figure 9.2, the maximum of $(\lambda - \lambda_0)w(\mathbf{r}, \lambda)$ is located at $(1 + \lambda_0 r)/r \simeq 1/r \gg \lambda_1$ when $1 \text{ mm} \leq r \leq 10 \text{ mm}$. Therefore, the following approximation takes place

$$\int_{\lambda_0}^{\lambda_1} (\lambda - \lambda_0)w d\lambda \ll \int_{\lambda_1}^{\infty} (\lambda - \lambda_0)w d\lambda, \quad (9.24)$$

and hence

$$S_{\text{ph}}^{\text{our}}(\mathbf{r}) \simeq \int_{\lambda_1}^{\infty} (\lambda - \lambda_0)w d\lambda - \int_{\lambda_1}^{\infty} (\lambda - \lambda_1)w d\lambda \simeq \lambda_1 \int_{\lambda_1}^{\lambda_{\text{cutoff}}} w d\lambda. \quad (9.25)$$

Since $\lambda_1 = 0.0015/\text{cm}$, on the interval $1 \text{ mm} \leq r \leq 10 \text{ mm}$, the value of $w(\lambda, r)$ decreases slowly, and only at $\lambda \simeq 7000\lambda_1$ it decreases by an order of magnitude, as can be seen in figure (9.5).

Again, assuming that we know the solution $w(\mathbf{r}, \lambda)$ as given by equation (9.21) with machine precision, let us calculate the integrals in equation (9.23) using the composite Simpson's quadrature rule [144] with N integration terms. For comparison we take $N = 3$ of $w(\mathbf{r}, \lambda)$.

In pure nitrogen with 1 ppm oxygen, only our approach gives a result that agrees well with the analytical solution as shown in figure 9.6, while the other solutions have a wrong algebraic decay.

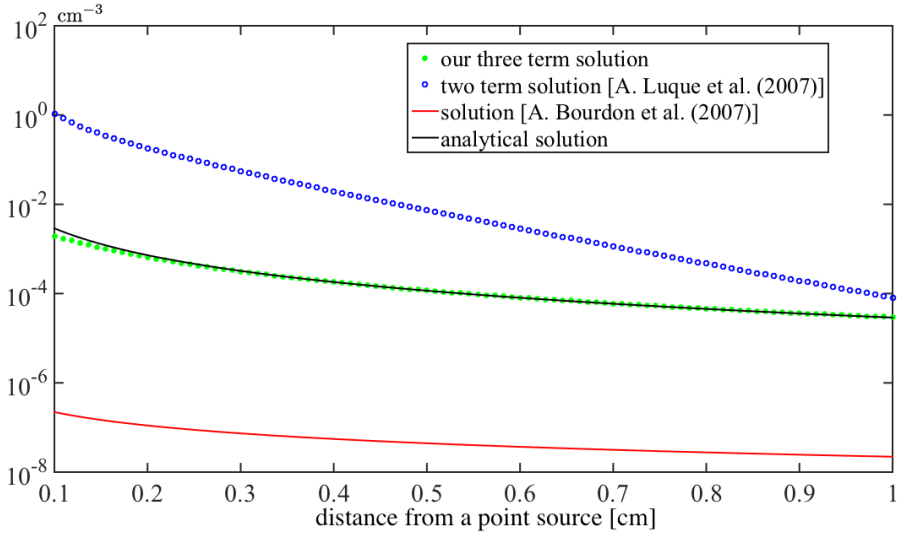


Figure 9.6: The photoionization $S_{\text{ph}}(\mathbf{r})$ in equation (9.9) for a point source $g(\mathbf{r}') = \delta(\mathbf{r}')$ calculated directly and numerically in pure nitrogen with 1 ppm oxygen at STP. The black solid curve is given by the analytical solution equation (9.14). The red solid curve shows the solution given by equation (9.16) (three term approximation). The blue circles show the solution given by equation (9.18) (two term approximation). Our solution with three term approximation is shown with green circles.

9.5 A photon flux from a point source onto a flat surface

Let us demonstrate how our approach works for calculating the photon flux from a point source onto a flat surface. This example can be described in a cylindrical geometry (ρ, z) . We assume that a point photon source $\delta(\rho)\delta(z - z_1)/2\pi\rho$ is placed over an infinite flat surface at $z = z_0$ and we also assume no absorption $\lambda_{\text{abs}} = 0$ (for simplicity).

In this case, equation (9.12) defining the photon flux onto a surface can be simplified as follows

$$G(\rho, z_0) = \int \frac{g(\mathbf{r}')}{4\pi|\mathbf{r} - \mathbf{r}'|^3} d\mathbf{r}', \quad (9.26)$$

where $g = (z_0 - z_1)\delta(z' - z_1)\delta(\rho')/2\pi\rho'$. We took into account that the normal vector of the plane $z = z_0$ is a unit vector \mathbf{e}_z along the z axis.

The flux G onto every point of the surface ρ can be calculated analytically, and it reads

$$G(\tilde{\rho}, z_0) = \frac{1}{4\pi d^2(\tilde{\rho}^2 + 1)^{3/2}}. \quad (9.27)$$

where we use the notation: $d = z_1 - z_0$ and $\tilde{\rho} = \rho/d$.

Let us introduce a virtual absorption function as follows

$$G(\rho, z_0, \lambda = 0) = \int \frac{g(\mathbf{r}') \exp(-\lambda|\mathbf{r} - \mathbf{r}'|)}{4\pi|\mathbf{r} - \mathbf{r}'|^3} d\mathbf{r}', \quad (9.28)$$

and make use of the integration with respect to λ , as in equation (9.6):

$$G(\rho, z_0) = \int_0^\infty \lambda w(\rho, z_0, \lambda) d\lambda, \quad (9.29)$$

where

$$\Delta w - \lambda^2 w = -I_1. \quad (9.30)$$

The solution of equation (9.30) for the points on the surface $z = z_0$ is its Green's function, which reads

$$w(\tilde{\rho}, z_0, \lambda) = \frac{\exp(-\lambda\sqrt{\tilde{\rho}^2 + 1})}{4\pi d\sqrt{\tilde{\rho}^2 + 1}}. \quad (9.31)$$

Now let us take, for example, Simpson's quadrature rule and its convergence in the interval $0 \leq \tilde{\rho} \leq 1$ (with respect to the analytical solution in equation (9.27)) depends on how many integration points in equation (9.29) we take. The maximal value of $\lambda w(\rho, z_0, \lambda)$ is $1/d\sqrt{\tilde{\rho}^2 + 1}$ (see figure 9.2), from which point on $\lambda w(\rho, z_0, \lambda)$ exponentially decreases. As in the example with photoionization, for $\lambda \geq 7/d$, the function $\lambda w(\rho, z_0, \lambda)$ drops by an order of magnitude, and therefore we can take $\lambda_{\text{cutoff}} = 7/d$.

The comparison of the result obtained with our method for 5, 11, 21, and 101 terms in the Simpson's integration scheme with the analytical solution in equation (9.27) is shown in figure 9.7. Starting from 11 terms, the convergence is reasonably good, and all the terms can be calculated in parallel. A more rigorous analysis is required to estimate the actual convergence rate with increasing number of terms, as that may depend on the choice on the truncation point, which in our case was $\lambda = 7/d$.

9.6 Conclusions

We designed a new approach to numerically calculate integrals of the type that is encountered in discharge physics in the context of photoionization or photoemission. It includes differentiating the integrals with respect to a parameter, which can be interpreted as an absorption coefficient. The approach recasts the problem of calculating an integral to solving a few Helmholtz equations with an efficient Poisson solver.

The method does not include any preliminary fitting. Its convergence depends on the knowledge about the length scales of the problem of interest. The method also allows error control and essentially works for an arbitrary geometry.

In atmospheric air, the approach proves to work well for calculating photoionization for a point source and its accuracy is comparable to other methods developed for that purpose. In pure nitrogen, only our new approach performs well.

The next step in this study could be to investigate the optimal numerical approximation in equation (9.6) for a given source $g(\mathbf{r})$ and other geometries.

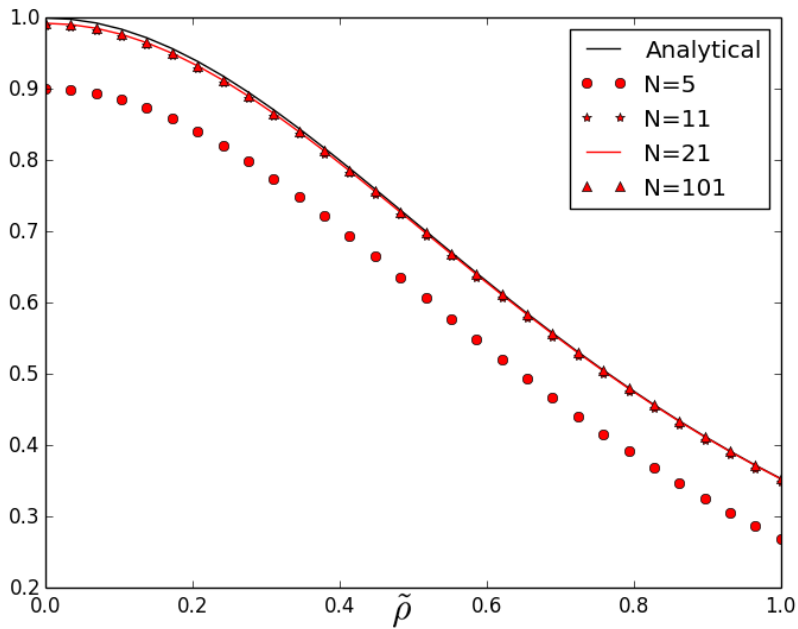


Figure 9.7: Flux $4\pi d^2 F(\tilde{\rho}, z_0)$ calculated analytically and numerically. Black line: analytically calculated flux given by equation (9.27). Red circles: flux calculated numerically with Simpson's quadrature rule for the number of integration terms $N = 5$, and respectively, red asterisks: $N = 11$, straight red line $N = 21$, red triangles: $N = 101$.

Chapter 10

Conclusions and outlook

10.1 Conclusions

Here we summarize the results on streamers near dielectrics obtained by our models. As a general conclusion we would like to point out that the physics behind streamer interaction with dielectrics is very complex, and that the numerical tools to study it are scarce and challenging to develop.

In this thesis a lot of effort was put into implementing dielectric interfaces into a simulation domain. One of the bottlenecks was to design a Poisson solver that can capture discontinuous boundary conditions on dielectric boundaries, in particular when they do not follow the mesh. For handling this problem we chose the Ghost Fluid Method, which we describe in chapter 3. It allows to incorporate dielectric and conductive interfaces of an arbitrary shape into the discretization matrix for the Poisson equation in an accurate way. This approach proved to be flexible and efficient on nonuniform static meshes in our 2D cylindrical streamer simulations. Even though the Ghost Fluid Method can be translated to 3D, its efficiency and the complexity of its implementation may not be optimal for 3D streamer simulations, where adaptive meshes are almost unavoidable.

Another numerical tool that was developed in the thesis allows to include photoemission from a dielectric surface. Photoemission, akin to photoionization in bulk gas, is a non-local source of free electrons. Therefore it is particularly important for positive streamers that grow through absorption of electron avalanches. In some geometries, for example with dielectric cylinders as used in chapters 4 and 5, shading effects can be encountered. Basically, one side of a dielectric can block photons from reaching the other side of the dielectric, and thus the photon flux is partly suppressed. We calculate the correction to the photon flux onto a dielectric cylinder due to the shading effect.

In chapter 4 we used a 2D cylindrically symmetric fluid streamer model to study pulsed positive streamer interaction with a dielectric rod in air and in nitrogen in cylindrical pin-to-plate geometry. That geometry was designed to compare simulations with dedicated experiments carried out by D. Trienekens. To ensure the cylindrical geome-

try both in simulations and experiments we made our streamer diameter larger than the diameter of the dielectric rod by reducing the pressure to 75-150 mbar. A number of interesting observations has been made in that study:

- In air positive discharges do not propagate along a dielectric rod, but move away from it, as long as they have cylindrical symmetry. This unexpected observation was made both in simulations and experiments. The dielectric rod appeared to be a mere obstacle for the discharge and the properties of the dielectric did not play a role. This behavior can be explained with the abundance of photoionization in air that allows the discharge to move along the electric field lines. Besides, in cylindrical geometry, a ring-like discharge experiences both attraction to the dielectric rod and electrostatic self-repulsion. In our parameter regime with thin and long dielectric rods, small gaps, and moderate dielectric permittivity, the self-repulsion dominates over the attraction to the dielectric rod. Even changing the photoemission yield from 0 to an unrealistically large value of 1 did not make the discharge follow the surface. Our estimations based on field calculations predict surface discharges only for (unrealistically) high permittivities of the rod and for much wider rods.
- When the cylindrical symmetry of the discharge is broken, in other words, when the inception cloud destabilizes into filaments, the electrostatic self-repulsion of the discharge disappears and the discharge can move over the rod. This is observed in experiments performed by D. Trienekens.
- In pure nitrogen, photoionization is suppressed, and the role of free electrons produced by the dielectric surface becomes more significant. Therefore, in pure nitrogen surface streamers are more likely than in air. This observation was made both in experiments and in simulations. Although our 2D streamer model predicts cylindrically symmetric surface streamers in pure nitrogen, this result should be interpreted as a proof of concept, because surface streamers observed in the experiments do not have cylindrical symmetry.
- When the repetition frequency of a discharge increases, the remaining background ionization increases too, because the charge carriers of the previous discharges do not have enough time to recombine. This volume “leftover” ionization can be a source of free electrons competing with photoemission in pure nitrogen. As a consequence, surface discharges disappear at sufficiently high repetition frequency of pulses, as the discharge does not have to deviate from the field lines to feed itself with free electrons.

In chapter 5 we elaborated on the competition of the attraction of a cylindrical discharge to a dielectric rod and its electrostatic self-repulsion in air. We modified the geometry slightly so that in the new setup the electrode is embedded into a dielectric rod. That eliminated the unnecessary numerical complications related to the electrode.

In that study we found that there exists a threshold dielectric permittivity ϵ_{th} . For dielectric permittivities larger than ϵ_{th} , the maximum of the electric field of the discharge is on the surface, which suggests the appearance of a surface discharge. We observed that photoemission can lower the value of ϵ_{th} , meaning that a discharge has a surface component already at lower values of the dielectric permittivity. We also confirmed the result obtained with field calculations that wider rods are more likely to create cylindrically symmetric surface discharges.

In chapter 6 we describe the progress we made in understanding lightning inception from ice particles that are present in thunderclouds. Big and sharp enough ice particles are able to enhance the sub-breakdown electric field in thunderclouds locally such that it becomes larger than the breakdown field at that altitude. Using the ionization integral we estimated how big and sharp ice particles have to be to increase the electric field sufficiently. In that study we also addressed another problem. On average, in the humid air of thunderclouds there are essentially no free electrons. However, free electrons can be temporarily produced by extensive air showers launched by highly energetic cosmic particles. These free electrons can trigger a discharge at the tip of an ice particle if the field is large enough there and extended over a large enough area. Both these ingredients (ice particles and extensive air showers) are necessary for lightning inception and they have to coincide in time and space. We took an electric field in accordance with balloon measurements. For that electric field we found an ice particle which can start a self-sustained streamer discharge. With our 2D fluid streamer model we simulated the time evolution of streamer inception from that ice particle in cylindrical geometry. With a Monte-Carlo based model we simulated which electron density will be produced by an extensive air shower and with which rate. We also estimated the probability of lightning inception in space and time for that example.

In chapter 7 we delved in more detail into the physics underlying positive streamer discharge inception from an elongated dielectric in a sub-breakdown electric field, based on the simulations performed for the lightning inception problem. We discovered that the Meek criterion widely used in electrical engineering to avoid discharges has to be revisited, as it gives only a rough estimation. When the initial electrons are distributed in space, a streamer can be formed with multiple electron avalanches that arrive at the dielectric at different moments in time. Besides, when the primary electron avalanches reach the dielectric, secondary avalanches can be initiated due to photoionization. And finally, around the tip of the dielectric the electric field lines converge, which means that the electron avalanches will converge too. That results in the increase of the charge density at the tip of the dielectric. For the lightning inception problem that implies that smaller ice particles can initiate a discharge than those predicted by the original Meek criterion. For the high-voltage technology this analysis based on the Meek number can offer a more accurate way to avoid undesired discharges.

In chapter 8 we discuss the results obtained in our study of streamer propagation in a small gap between a positive pin anode and a dielectric tip under a voltage pulse with a sub-nanosecond rise time. Interestingly, in air the streamer reaches the tip, whereas in nitrogen, it does not, creating an electron-free area avoided by a positive streamer. In

air, due to the abundant photoionization that area is filled with electrons continuously.

In the final chapter 9 we describe an alternative approach to calculate the photoionization and photoemission integrals. The approach is based on treating the absorption coefficient as a separate variable. By differentiating the integral with respect to the absorption coefficient we can reduce it to the Green function of a Helmholtz equation. Efficient solvers for Helmholtz equations are typically available in streamer discharge models, because they are used as a Poisson solver for the streamer electric field. Besides, since numerical implementation is not part of our approach, any appropriate numerical scheme can be chosen depending on the accuracy required in a given problem. The accuracy and efficiency of our approach for photoionization in air is comparable to the accuracy and efficiency of the other dedicated methods. In pure nitrogen, our approach gives more accurate results than the other methods. We also demonstrate how our approach can be implemented for photoemission from a flat surface.

10.2 Outlook

Streamer simulations near dielectrics and conductors in full 3D are still to be developed. A large progress has been made by J. Teunissen, who designed the AFIVO framework for adaptive finite volume simulations [145]. On the basis of that framework 3D streamer discharge simulations can be set up, but implementing curved dielectric and conductive interfaces with the underlying physics still remains to be done. 3D streamer simulations certainly make it easier to interpret the results and compare them with experiments, but they come with a cost. Besides verification and validation of any 3D streamer model, which are already a challenge, there are also the problems of computing memory and time and of visualization.

Another point that should be further studied in the context of surface streamer discharges is the dielectric function, in particular at a nanosecond time scale, i.e. at GHz frequencies. Streamers in atmospheric air typically develop within tens of nanoseconds and their space charge field changes with the streamer development. As was demonstrated in the thesis, a dielectric may react significantly different to such fast changes of the streamer electric field than it reacts to a static field. Surprisingly, there is not much experimental data on dielectric permittivities of various materials in the GHz regime.

The problem of lightning inception that was addressed in this thesis is still far from being solved. In our study we simulated only the first self-propagating phase of the lightning discharge. It will certainly be interesting to know how long lightning in its streamer phase can propagate and whether it can turn into a leader. Propagation of lightning between multiple ice particles is also an interesting problem, as ice particles are considered capable of facilitating lightning advancement. It is also known that ice particles are charged, although the measured data is scarce. This factor may also help lightning inception. Finally, a more extensive analysis can be done on which ice particles are capable of starting a lightning discharge. That includes their shape, charge and the dielectric properties. A nice selection tool would be an elaborated Meek

criterion, which takes into account the distribution of the initial electrons, electric field line convergence and photoionization. This criterion would also help advance high voltage technology.

In the last chapter of the thesis, we described an alternative method of calculating integrals for photoionization and photoemission that are encountered in discharge physics. The integrals addressed are of a rather general type and the method can potentially be applied to other problems unrelated to the physics of discharges, for example to radiation absorption. It would be also interesting to extend the method to radiation with a given spectrum.

Bibliography

- [1] L. Grabowski, E. van Veldhuizen, A. Pemen, and W. Rutgers, "Corona above water reactor for systematic study of aqueous phenol degradation," *Plasma Chemistry and Plasma Processing*, vol. 26, no. 1, pp. 3–17, 2006.
- [2] J. S. Clements, A. Mizuno, W. C. Finney, and R. H. Davis, "Combined removal of SO₂, NO_x, and fly ash from simulated flue gas using pulsed streamer corona," *Industry Applications, IEEE Transactions on*, vol. 25, no. 1, pp. 62–69, 1989.
- [3] G. Winands, K. Yan, A. Pemen, S. Nair, Z. Liu, and E. Van Heesch, "An industrial streamer corona plasma system for gas cleaning," *IEEE transactions on plasma science*, vol. 34, no. 5, p. 2426, 2006.
- [4] G. Fridman, G. Friedman, A. Gutsol, A. B. Shekhter, V. N. Vasilets, and A. Fridman, "Applied plasma medicine," *Plasma Processes and Polymers*, vol. 5, no. 6, pp. 503–533, 2008.
- [5] N. Y. Babaeva and M. J. Kushner, "Dynamics of dielectric barrier discharges over wounded skin," *IEEE Transactions on Plasma Science*, vol. 39, no. 11, p. 2964, 2011.
- [6] E. van Veldhuizen, "*Electrical Discharges for Environmental Purposes: Fundamentals and Applications*," Nova Science Publishers, New York, 2000.
- [7] E. Moreau, "Airflow control by non-thermal plasma actuators," *Journal of Physics D: Applied Physics*, vol. 40, no. 3, p. 605, 2007.
- [8] A. Starikovskiy and N. Aleksandrov, "Plasma-assisted ignition and combustion," *Progress in Energy and Combustion Science*, vol. 39, no. 1, pp. 61–110, 2013.
- [9] Wikisource, "A midsummer night's dream — wikisource," 2015. [Online; accessed 2-May-2016].
- [10] A. Sobota, E. van Veldhuizen, and W. W. Stoffels, "Discharge ignition near a dielectric," *IEEE Transactions on Plasma Science*, vol. 36, no. 4, p. 912, 2008.

- [11] M. Laan and P. Paris, "The multi-avalanche nature of streamer formation in inhomogeneous fields," *Journal of Physics D: Applied Physics*, vol. 27, no. 5, p. 970, 1994.
- [12] J. Meek, "A theory of spark discharge," *Physical Review*, vol. 57, no. 8, p. 722, 1940.
- [13] J. Townsend, "Motion of electrons in gases," *Proceedings of the Royal Society of London. Series A, Containing Papers of a Mathematical and Physical Character*, vol. 120, no. 786, pp. 511–523, 1928.
- [14] U. Ebert, S. Nijdam, C. Li, A. Luque, T. Briels, and E. van Veldhuizen, "Review of recent results on streamer discharges and discussion of their relevance for sprites and lightning," *Journal of Geophysical Research: Space Physics*, vol. 115, no. A7, 2010.
- [15] A. Rocco, U. Ebert, and W. Hundsdorfer, "Branching of negative streamers in free flight," *Physical Review E*, vol. 66, no. 3, p. 035102, 2002.
- [16] T. Briels, J. Kos, G. Winands, E. van Veldhuizen, and U. Ebert, "Positive and negative streamers in ambient air: measuring diameter, velocity and dissipated energy," *Journal of Physics D: Applied Physics*, vol. 41, no. 23, p. 234004, 2008.
- [17] A. Luque, V. Ratushnaya, and U. Ebert, "Positive and negative streamers in ambient air: modelling evolution and velocities," *Journal of Physics D: Applied Physics*, vol. 41, no. 23, p. 234005, 2008.
- [18] S. Pancheshnyi, "Role of electronegative gas admixtures in streamer start, propagation and branching phenomena," *Plasma Sources Science and Technology*, vol. 14, no. 4, p. 645, 2005.
- [19] I. G. Usoskin and G. A. Kovaltsov, "Cosmic ray induced ionization in the atmosphere: Full modeling and practical applications," *Journal of Geophysical Research: Atmospheres*, vol. 111, no. D21, 2006.
- [20] A. Sun, J. Teunissen, and U. Ebert, "The inception of pulsed discharges in air: simulations in background fields above and below breakdown," *Journal of Physics D: Applied Physics*, vol. 47, no. 44, p. 445205, 2014.
- [21] A. Sobota, A. Lebouvier, N. Kramer, E. van Veldhuizen, W. Stoffels, F. Manders, and M. Haverlag, "Speed of streamers in argon over a flat surface of a dielectric," *Journal of Physics D: Applied Physics*, vol. 42, no. 1, p. 015211, 2009.
- [22] D. J. Trienekens, S. Nijdam, and U. Ebert, "Stroboscopic images of streamers through air and over dielectric surfaces," *IEEE Transactions on Plasma Science*, vol. 42, no. 10, pp. 2400–2401, 2014.

- [23] M. Akyuz, L. Gao, V. Cooray, T. Gustavsson, S. Gubanski, and A. Larsson, "Positive streamer discharges along insulating surfaces," *Dielectrics and Electrical Insulation, IEEE Transactions on*, vol. 8, no. 6, pp. 902–910, 2001.
- [24] G. Laity, A. Neuber, A. Fierro, J. Dickens, and L. Hatfield, "Phenomenology of streamer propagation during pulsed dielectric surface flashover," *Dielectrics and Electrical Insulation, IEEE Transactions on*, vol. 18, no. 4, pp. 946–953, 2011.
- [25] A. Jehl, T. Farges, and E. Blanc, "Color pictures of sprites from non-dedicated observation on board the international space station," *Journal of Geophysical Research: Space Physics*, vol. 118, no. 1, pp. 454–461, 2013.
- [26] S. Pancheshnyi, M. Nudnova, and A. Starikovskii, "Development of a cathode-directed streamer discharge in air at different pressures: experiment and comparison with direct numerical simulation," *Physical Review E*, vol. 71, no. 1, p. 016407, 2005.
- [27] "BOLSIG+ the Boltzmann equation solver." <http://www.bolsig.laplace.univ-tlse.fr>.
- [28] S. Pancheshnyi, S. Starikovskaia, and A. Y. Starikovskii, "Collisional deactivation of N_2 ($C^3\Pi_u$, $\nu = 0, 1, 2, 3$) states by N_2 , O_2 , H_2 and H_2O molecules," *Chemical Physics*, vol. 262, no. 2, pp. 349–357, 2000.
- [29] R. E. Jorgenson, L. K. Warne, A. A. Neuber, J. Krile, J. Dickens, and H. G. Krompholz, "Effect of dielectric photoemission on surface breakdown: An LDRD report," *Sandia Report SAND2000-3044*, 2003.
- [30] N. Y. Babaeva, A. N. Bhoj, and M. J. Kushner, "Streamer dynamics in gases containing dust particles," *Plasma Sources Science and Technology*, vol. 15, no. 4, p. 591, 2006.
- [31] J. Jánský, F. Tholin, Z. Bonaventura, and A. Bourdon, "Simulation of the discharge propagation in a capillary tube in air at atmospheric pressure," *Journal of Physics D: Applied Physics*, vol. 43, no. 39, p. 395201, 2010.
- [32] J. Capeillere, P. Ségur, A. Bourdon, S. Célestin, and S. Pancheshnyi, "The finite volume method solution of the radiative transfer equation for photon transport in non-thermal gas discharges: application to the calculation of photoionization in streamer discharges," *Journal of Physics D: Applied Physics*, vol. 41, no. 23, p. 234018, 2008.
- [33] M. J. Kushner, "Modelling of microdischarge devices: plasma and gas dynamics," *Journal of Physics D: Applied Physics*, vol. 38, no. 11, p. 1633, 2005.
- [34] A. N. Bhoj and M. J. Kushner, "Avalanche process in an idealized lamp: II. modelling of breakdown in Ar/Xe electric discharges," *Journal of Physics D: Applied Physics*, vol. 37, no. 18, p. 2510, 2004.

- [35] A. Phelps and Z. L. Petrovic, "Cold-cathode discharges and breakdown in argon: surface and gas phase production of secondary electrons," *Plasma Sources Science and Technology*, vol. 8, no. 3, p. R21, 1999.
- [36] P. Bokhan and D. E. Zakrevsky, "Noble-gas resonant radiation effects on electron emission in plasma devices," *Physical Review E*, vol. 88, no. 1, p. 013105, 2013.
- [37] A. Jaksts and J. Cross, "The influence of a solid dielectric spacer on electron avalanches in nitrogen at atmospheric pressure," *Electrical Engineering Journal, Canadian*, vol. 6, no. 2, pp. 14–18, 1981.
- [38] O. Griffith, D. Holmbo, D. Habliston, and K. Nadakavukaren, "Contrast effects in photoelectron microscopy: UV dose-dependent quantum yields of biological surface components," *Ultramicroscopy*, vol. 6, no. 1, pp. 149–156, 1981.
- [39] R. J. Dam, C. A. Burke, and O. H. Griffith, "Photoelectron quantum yields of the amino acids," *Biophysical journal*, vol. 14, no. 6, pp. 467–472, 1974.
- [40] M. Fujihira, T. Hirooka, and H. Inokuchi, "Photoemission from compounds containing benzene, naphthalene and anthracene ring systems," *Chemical Physics Letters*, vol. 19, no. 4, pp. 584–587, 1973.
- [41] A. Buzulutskov, A. Breskin, and R. Chechik, "Photoemission through thin dielectric coating films," *Journal of Applied Physics*, vol. 81, no. 1, pp. 466–479, 1997.
- [42] H. Verhaart, J. Tom, A. Verhage, and C. Vos, "Avalanches near solid insulators," in *Proceeding of the 5th International Symposium on HV Engineering*, Braunschweig, 1987.
- [43] W. A. Houle, H. M. Brown, and O. H. Griffith, "Photoelectric properties and detection of the aromatic carcinogens benza [a] pyrene and dimethylbenzanthracene," *Proceedings of the National Academy of Sciences*, vol. 76, no. 9, pp. 4180–4184, 1979.
- [44] G. A. Mesyats, "Electron emission from ferroelectric plasma cathodes," *Physics-Uspekhi*, vol. 51, no. 1, p. 79, 2008.
- [45] J. Tom, H. Verhaart, A. Verhage, and C. Vos, "Photo-emission of charged insulators in insulating gases," in *Proceedings of the 2nd International Conference on Conduction and Breakdown in Solid Dielectrics*, Erlangen, pp. 301–307, 1986.
- [46] A. Guzhov and Y. A. Shuba, "The photoemission of some massive insulators in the vacuum ultraviolet," *Optical Technology*, vol. 38, no. 4, pp. 198–199, 1971.
- [47] I. Abroyan, M. Ereemeev, and N. Petrov, "Excitation of electrons in solids by relatively slow atomic particles," *Physics-Uspekhi*, vol. 10, no. 3, pp. 332–367, 1967.

- [48] F. Pechereau, J. Jánský, and A. Bourdon, "Simulation of the reignition of a discharge behind a dielectric layer in air at atmospheric pressure," *Plasma Sources Science and Technology*, vol. 21, no. 5, p. 055011, 2012.
- [49] A. Phelps, "Cross sections and swarm coefficients for nitrogen ions and neutrals in N₂ and argon ions and neutrals in Ar for energies from 0.1 eV to 10 keV," *Journal of Physical and Chemical Reference Data*, vol. 20, no. 3, pp. 557–573, 1991.
- [50] G. J. M. Hagelaar and L. C. Pitchford, "Solving the Boltzmann equation to obtain electron transport coefficients and rate coefficients for fluid models," *Plasma Sources Science and Technology*, vol. 14, no. 4, p. 722, 2005.
- [51] L. Niemeyer, "A generalized approach to partial discharge modeling," *Dielectrics and Electrical Insulation, IEEE Transactions on*, vol. 2, no. 4, pp. 510–528, 1995.
- [52] J. Dutton, "Spark breakdown in uniform fields," *Electrical Breakdown of Gases*, pp. 209–318, 1978.
- [53] P. Paris, M. Aints, F. Valk, T. Plank, A. Haljaste, K. Kozlov, and H. Wagner, "Reply to comments on "Intensity ratio of spectral bands of nitrogen as a measure of electric field strength in plasmas","" *Journal of Physics D: Applied Physics*, vol. 39, no. 12, p. 2636, 2006.
- [54] Y. V. Krasnyak, S. Y. Petrin, and O. Sinkevich, "Tunneling mechanism for the formation of negative ions near the electrode," *Soviet Journal of Experimental and Theoretical Physics Letters*, vol. 48, p. 416, 1988.
- [55] M. Kiziroglou, X. Li, A. Zhukov, P. De Groot, and C. De Groot, "Thermionic field emission at electrodeposited Ni–Si schottky barriers," *Solid-State Electronics*, vol. 52, no. 7, pp. 1032–1038, 2008.
- [56] X.-D. Liu, R. P. Fedkiw, and M. Kang, "A boundary condition capturing method for Poisson's equation on irregular domains," *Journal of Computational Physics*, vol. 160, no. 1, pp. 151–178, 2000.
- [57] S. Celestin, Z. Bonaventura, B. Zeghondy, A. Bourdon, and P. Ségur, "The use of the ghost fluid method for Poisson's equation to simulate streamer propagation in point-to-plane and point-to-point geometries," *Journal of Physics D: Applied Physics*, vol. 42, no. 6, p. 065203, 2009.
- [58] J. Teunissen and U. Ebert, "Controlling the weights of simulation particles: adaptive particle management using k-d trees," *Journal of Computational Physics*, vol. 259, pp. 318–330, 2014.

- [59] S. Dujko, A. Markosyan, R. White, and U. Ebert, “High-order fluid model for streamer discharges: I. derivation of model and transport data,” *Journal of Physics D: Applied Physics*, vol. 46, no. 47, p. 475202, 2013.
- [60] A. Markosyan, S. Dujko, and U. Ebert, “High-order fluid model for streamer discharges: II. numerical solution and investigation of planar fronts,” *Journal of Physics D: Applied Physics*, vol. 46, no. 47, p. 475203, 2013.
- [61] C. Li, U. Ebert, and W. Hundsdorfer, “Spatially hybrid computations for streamer discharges: Ii. fully 3d simulations,” *Journal of Computational Physics*, vol. 231, no. 3, pp. 1020–1050, 2012.
- [62] C. Li, U. Ebert, and W. Hundsdorfer, “3D hybrid computations for streamer discharges and production of runaway electrons,” *Journal of Physics D: Applied Physics*, vol. 42, no. 20, p. 202003, 2009.
- [63] L. Niemeyer, L. Pietronero, and H. Wiesmann, “Fractal dimension of dielectric breakdown,” *Physical Review Letters*, vol. 52, no. 12, p. 1033, 1984.
- [64] A. Luque and U. Ebert, “Growing discharge trees with self-consistent charge transport: the collective dynamics of streamers,” *New Journal of Physics*, vol. 16, no. 1, p. 013039, 2014.
- [65] “MUMPS parallel sparse direct solver.” <http://mumps.enseeiht.fr>.
- [66] Y. Saad and M. H. Schultz, “GMRES: A generalized minimal residual algorithm for solving nonsymmetric linear systems,” *SIAM Journal on Scientific and Statistical Computing*, vol. 7, no. 3, pp. 856–869, 1986.
- [67] C. Montijn, W. Hundsdorfer, and U. Ebert, “An adaptive grid refinement strategy for the simulation of negative streamers,” *Journal of Computational Physics*, vol. 219, no. 2, pp. 801–835, 2006.
- [68] R. P. Fedkiw, T. Aslam, and S. Xu, “The ghost fluid method for deflagration and detonation discontinuities,” *Journal of Computational Physics*, vol. 154, no. 2, pp. 393–427, 1999.
- [69] C. S. Peskin, “Numerical analysis of blood flow in the heart,” *Journal of Computational Physics*, vol. 25, no. 3, pp. 220–252, 1977.
- [70] C. Min, F. Gibou, and H. Cenicerros, “A supra-convergent finite difference scheme for the variable coefficient Poisson equation on fully adaptive grids,” *Journal of Computational Physics*, vol. 202, pp. 577–601, 2006.
- [71] V. I. Gibalov and G. J. Pietsch, “The development of dielectric barrier discharges in gas gaps and on surfaces,” *Journal of Physics D: Applied Physics*, vol. 33, no. 20, p. 2618, 2000.

- [72] V. I. Gibalov and G. J. Pietsch, "Dynamics of dielectric barrier discharges in different arrangements," *Plasma Sources Science and Technology*, vol. 21, no. 2, p. 024010, 2012.
- [73] V. Yordanov, A. Blagoev, I. Ivanova-Stanik, E. Van Veldhuizen, S. Nijdam, J. Van Dijk, and J. Van Der Mullen, "Surface ionization wave in a plasma focus-like model device," *Journal of Physics D: Applied Physics*, vol. 41, no. 21, p. 215208, 2008.
- [74] T. Christen, H. Böhme, A. Pedersen, and A. Blaszczyk, "Streamer line modeling," in *Scientific Computing in Electrical Engineering SCEE 2010*, pp. 173–181, Springer, 2012.
- [75] F. Mauseth, J. Jørstad, and A. Pedersen, "Streamer inception and propagation for air insulated rod-plane gaps with barriers," in *Electrical Insulation and Dielectric Phenomena (CEIDP), 2012 Annual Report Conference on*, pp. 739–732, IEEE, 2012.
- [76] N. Allen and P. Mikropoulos, "Streamer propagation along insulating surfaces," *Dielectrics and Electrical Insulation, IEEE Transactions on*, vol. 6, no. 3, pp. 357–362, 1999.
- [77] X. Meng, H. Mei, C. Chen, L. Wang, Z. Guan, and J. Zhou, "Characteristics of streamer propagation along the insulation surface: influence of dielectric material," *Dielectrics and Electrical Insulation, IEEE Transactions on*, vol. 22, no. 2, pp. 1193–1203, 2015.
- [78] K. P. Morales, J. T. Krile, A. A. Neuber, and H. G. Krompholz, "Pulsed dielectric surface flashover in nitrogen at atmospheric conditions," *Dielectrics and Electrical Insulation, IEEE Transactions on*, vol. 13, no. 4, pp. 803–809, 2006.
- [79] K. Morales, J. Krile, A. Neuber, and H. Krompholz, "Dielectric surface flashover at atmospheric conditions with unipolar pulsed voltage excitation," *IEEE Transactions on Dielectrics and Electrical Insulation*, vol. 14, no. 4, p. 774, 2007.
- [80] J. Krile, G. Edmiston, K. Morales, A. Neuber, H. Krompholz, and M. Kristiansen, "Similarities of dielectric surface flashover under atmospheric conditions for pulsed unipolar and RF excitation," *Laser Physics*, vol. 16, pp. 194–201, jan 2006.
- [81] S. Voeten, *Matching high voltage pulsed power technologies*. PhD thesis, Technische Universiteit Eindhoven, 2013.
- [82] A. Dubinova, D. Trienekens, U. Ebert, and S. Nijdam, "Affinity of pulsed positive discharges to dielectrics in $N_2:O_2$ mixtures," in *Proceedings of International Conference on Phenomena in Ionized Gases 2015 (ICPIG 32)*, 2015.

- [83] T. M. P. Briels, E. M. van Veldhuizen, and U. Ebert, "Positive streamers in air and nitrogen of varying density: experiments on similarity laws," *J. Phys. D: Appl. Phys.*, vol. 41, p. 234008, 2008.
- [84] S. Chen, L. C. J. Heijmans, R. Zeng, S. Nijdam, and U. Ebert, "Nanosecond repetitively pulsed discharges in N_2 - O_2 mixtures: inception cloud and streamer emergence," *Journal of Physics D: Applied Physics*, vol. 48, p. 175201, May 2015.
- [85] G. Naidis, "Positive and negative streamers in air: velocity-diameter relation," *Physical Review E*, vol. 79, no. 5, p. 057401, 2009.
- [86] G. Georghiou, R. Morrow, and A. Metaxas, "The effect of photoemission on the streamer development and propagation in short uniform gaps," *Journal of Physics D: Applied Physics*, vol. 34, no. 2, p. 200, 2001.
- [87] M. Fujihira and H. Inokuchi, "Photoemission from polyethylene," *Chemical Physics Letters*, vol. 17, no. 4, pp. 554–556, 1972.
- [88] A. Hallac, G. Georghiou, and A. Metaxas, "Secondary emission effects on streamer branching in transient non-uniform short-gap discharges," *Journal of Physics D: Applied Physics*, vol. 36, no. 20, p. 2498, 2003.
- [89] A. Luque and U. Ebert, "Density models for streamer discharges: beyond cylindrical symmetry and homogeneous media," *Journal of Computational Physics*, vol. 231, no. 3, pp. 904–918, 2012.
- [90] F. X. Bronold and H. Fehske, "Absorption of an electron by a dielectric wall," *Physical Review Letters*, vol. 115, no. 22, p. 225001, 2015.
- [91] B. Koren, *A robust upwind discretization method for advection, diffusion and source terms*. Centrum voor Wiskunde en Informatica Amsterdam, 1993.
- [92] P. Vitello, B. Penetrante, and J. Bardsley, "Simulation of negative-streamer dynamics in nitrogen," *Physical Review E*, vol. 49, no. 6, p. 5574, 1994.
- [93] M. Zheleznyak, A. K. Mnatsakanian, and S. Sizykh, "Photoionization of mixtures of nitrogen and oxygen by gas discharge radiation," *Teplofiz. Vys. Temp.*, vol. 20, pp. 423–8, 1982.
- [94] A. Luque, U. Ebert, C. Montijn, and W. Hundsdorfer, "Photoionization in negative streamers: Fast computations and two propagation modes," *Applied Physics Letters*, vol. 90, no. 8, p. 081501, 2007.
- [95] S. Nijdam, G. Wormeester, E. van Veldhuizen, and U. Ebert, "Probing background ionization: positive streamers with varying pulse repetition rate and with a radioactive admixture," *Journal of Physics D: Applied Physics*, vol. 44, no. 45, p. 455201, 2011.

- [96] S. Pancheshnyi, B. Eismann, G. Hagelaar, and L. Pitchford, "Computer code ZDPlasKin, University of Toulouse, LAPLACE," tech. rep., CNRS–UPS–INP, Toulouse, France, 2008, <http://www.zdplaskin.laplace.univ-tlse.fr>, 2008.
- [97] Y. V. Shcherbakov and R. S. Sigmond, "Subnanosecond spectral diagnostics of streamer discharges: I. Basic experimental results," *Journal of Physics D: Applied Physics*, vol. 40, no. 2, pp. 460–473, 2007.
- [98] P. P. M. Blom, C. Smit, R. H. P. Lemmens, and E. J. M. van Heesch, "Combined Optical and Electrical Measurements on Pulsed Corona Discharges," *Gaseous Dielectrics VII*, vol. 7, pp. 609–615, 1994.
- [99] D. J. M. Trienekens, S. Nijdam, and U. Ebert, "Stroboscopic Images of Streamers Through Air and Over Dielectric Surfaces," *IEEE Transactions on Plasma Science*, vol. 42, pp. 2400–2401, Oct. 2014.
- [100] G. Dilecce, P. F. Ambrico, and S. De Benedictis, "On the collision quenching of $N_2(B^2\Sigma_u^+, \nu=0)$ by N_2 and O_2 and its influence on the measurement of E/N by intensity ratio of nitrogen spectral bands," *Journal of Physics D: Applied Physics*, vol. 43, no. 19, p. 195201, 2010.
- [101] Y. V. Shcherbakov and R. S. Sigmond, "Subnanosecond spectral diagnostics of streamer discharges: II. Theoretical background," *Journal of Physics D: Applied Physics*, vol. 40, no. 2, pp. 474–487, 2007.
- [102] J. van Dijk, K. Peerenboom, M. Jimenez, D. Mihailova, and J. van der Mullen, "The plasma modelling toolkit plasimo," *Journal of Physics D: Applied Physics*, vol. 42, no. 19, p. 194012, 2009.
- [103] G. Wormeester, S. Pancheshnyi, A. Luque, S. Nijdam, and U. Ebert, "Probing photo-ionization: simulations of positive streamers in varying $N_2:O_2$ -mixtures," *Journal of Physics D: Applied Physics*, vol. 43, no. 50, p. 505201, 2010.
- [104] M. Stolzenburg and T. C. Marshall, "Electric field and charge structure in lightning-producing clouds," in *Lightning: Principles, Instruments and Applications*, pp. 57–82, Springer, 2009.
- [105] J. R. Dwyer and M. A. Uman, "The physics of lightning," *Physics Reports*, vol. 534, no. 4, pp. 147–241, 2014.
- [106] L. Coleman and J. Dwyer, "Propagation speed of runaway electron avalanches," *Geophysical Research Letters*, vol. 33, no. 11, 2006.
- [107] J. A. Crabb and J. Latham, "Corona from colliding drops as a possible mechanism for the triggering of lightning," *Quarterly Journal of the Royal Meteorological Society*, vol. 100, no. 424, pp. 191–202, 1974.

- [108] D. Petersen, M. Bailey, J. Hallett, and W. H. Beasley, "Laboratory investigation of positive streamer discharges from simulated ice hydrometeors," *Quarterly Journal of the Royal Meteorological Society*, vol. 132, no. 615, pp. 263–273, 2006.
- [109] D. A. Petersen, M. Bailey, J. Hallett, and W. Beasley, "Laboratory investigation of corona initiation by ice crystals and its importance to lightning," *Quarterly Journal of the Royal Meteorological Society*, 2014.
- [110] N. Liu, B. Kosar, S. Sadighi, J. R. Dwyer, and H. K. Rassoul, "Formation of streamer discharges from an isolated ionization column at subbreakdown conditions," *Physical Review Letters*, vol. 109, no. 2, p. 025002, 2012.
- [111] A. Sun, J. Teunissen, and U. Ebert, "Why isolated streamer discharges hardly exist above the breakdown field in atmospheric air," *Geophysical Research Letters*, vol. 40, no. 10, pp. 2417–2422, 2013.
- [112] J. Teunissen, A. Sun, and U. Ebert, "A time scale for electrical screening in pulsed gas discharges," *Journal of Physics D: Applied Physics*, vol. 47, no. 36, p. 365203, 2014.
- [113] M. Huertas, J. Fontan, and J. Gonzalez, "Evolution times of tropospheric negative ions," *Atmospheric Environment (1967)*, vol. 12, no. 12, pp. 2351–2362, 1978.
- [114] I. Gallimberti, "The mechanism of the long spark formation," *Journal de Physique Colloques*, vol. 40, no. C7, 1979.
- [115] A. Gurevich and A. Karashtin, "Runaway breakdown and hydrometeors in lightning initiation," *Physical Review Letters*, vol. 110, no. 18, p. 185005, 2013.
- [116] K. Olive, P. D. Group, *et al.*, "Review of particle physics," *Chinese Physics C*, vol. 38, no. 9, p. 090001, 2014.
- [117] E. Williams, "Charge structure and geographical variation of thunderclouds, in "The Lightning Flash", edited by V. Cooray," pp. 1–15, 2008.
- [118] L. Landau and E. Lifshitz, *Electrodynamics of continuous media*, vol. 8. Pergamon Press, 1960.
- [119] D. Lamb and J. Verlinde, *Physics and chemistry of clouds*. Cambridge University Press, 2011.
- [120] V. Artemov and A. Volkov, "Water and ice dielectric spectra scaling at 0°C," *Ferroelectrics*, vol. 466, no. 1, pp. 158–165, 2014.

- [121] S. Fujita, T. Matsuoka, T. Ishida, K. Matsuoka, and S. Mae, “A summary of the complex dielectric permittivity of ice in the megahertz range and its applications for radar sounding of polar ice sheets,” *Physics of Ice Core Records*, pp. 185–212, 2000.
- [122] J. R. Dwyer and L. P. Babich, “Low-energy electron production by relativistic runaway electron avalanches in air,” *Journal of Geophysical Research: Space Physics (1978–2012)*, vol. 116, no. A9, 2011.
- [123] D. Heck, J. Knapp, J. Capdevielle, G. Schatz, T. Thouw, *et al.*, *CORSIKA: A Monte Carlo code to simulate extensive air showers*, vol. 6019. FZKA, 1998.
- [124] M. J. Berger, J. Coursey, M. Zucker, and J. Chang, “NIST physics laboratory, stopping power electrons.” Retrieved on Jan 2015 from www.nist.gov/pml/data/star/.
- [125] B. Mason, “On the generation of charge associated with graupel formation in thunderstorms,” *Quarterly Journal of the Royal Meteorological Society*, vol. 79, no. 342, pp. 501–509, 1953.
- [126] R. Wijsman, “Breakdown Probability of a Low Pressure Gas Discharge,” *Physical Review*, vol. 75, no. 5, pp. 833–838, 1949.
- [127] R. V. Hodges, R. N. Varney, and J. F. Riley, “Probability of electrical breakdown: Evidence for a transition between the Townsend and streamer breakdown mechanisms,” *Physical Review A*, vol. 31, no. 4, p. 2610, 1985.
- [128] A. Dubinova, C. Rutjes, U. Ebert, S. Buitink, O. Scholten, and G. T. N. Trinh, “Prediction of lightning inception by large ice particles and extensive air showers,” *Physical Review Letters*, vol. 115, no. 1, p. 015002, 2015.
- [129] H. Raether, “Die Entwicklung der Elektronenlawine in den Funkenkanal,” *Zeitschrift fuer Physik*, vol. 112, no. 7-8, pp. 464–489, 1939.
- [130] L. B. Loeb and J. M. Meek, “The mechanism of spark discharge in air at atmospheric pressure. I,” *Journal of Applied Physics*, vol. 11, no. 6, pp. 438–447, 1940.
- [131] L. B. Loeb and J. M. Meek, “The mechanism of spark discharge in air at atmospheric pressure. II,” *Journal of Applied Physics*, vol. 11, no. 7, pp. 459–474, 1940.
- [132] M. Laan and P. Paris, “The multi-avalanche nature of streamer formation in inhomogeneous fields,” *Journal of Physics D: Applied Physics*, vol. 27, no. 5, pp. 970–978, 1999.

- [133] C. Montijn and U. Ebert, “Diffusion correction to the raether–mEEK criterion for the avalanche-to-streamer transition,” *Journal of Physics D: Applied Physics*, vol. 39, no. 14, p. 2979, 2006.
- [134] G. V. Naidis, “Conditions for inception of positive corona discharges in air,” *Journal of Physics D: Applied Physics*, vol. 38, no. 13, p. 2211, 2005.
- [135] T. Huiskamp, “Nanosecond pulsed power technology for transient plasma generation,” 2015.
- [136] T. Matsumoto, D. Wang, T. Namihira, and H. Akiyama, “Energy efficiency improvement of nitric oxide treatment using nanosecond pulsed discharge,” *IEEE Transactions on Plasma Science*, vol. 38, no. 10, pp. 2639–2643, 2010.
- [137] H.-H. Kim, “Nonthermal plasma processing for air-pollution control: a historical review, current issues, and future prospects,” *Plasma Processes and Polymers*, vol. 1, no. 2, pp. 91–110, 2004.
- [138] T. Huiskamp, F. Beckers, E. van Heesch, and A. Pemen, “First implementation of a subnanosecond rise time, variable pulse duration, variable amplitude, repetitive, high-voltage pulse source,” *IEEE Transactions on Plasma Science*, vol. 42, no. 3, pp. 859–867, 2014.
- [139] U. Ebert, C. Montijn, T. M. P. Briels, W. Hundsdorfer, B. Meulenbroek, A. Rocco, and E. M. van Veldhuizen, “The multiscale nature of streamers,” *Plasma Sources Science and Technology*, vol. 15, no. 2, 2006.
- [140] S. Nijdam, E. Takahashi, J. Teunissen, and U. Ebert, “Streamer discharges can move perpendicularly to the electric field,” *New Journal of Physics*, vol. 16, no. 10, p. 103038, 2014.
- [141] A. Bourdon, V. Pasko, N. Liu, S. Célestin, P. Ségur, and E. Marode, “Efficient models for photoionization produced by non-thermal gas discharges in air based on radiative transfer and the Helmholtz equations,” *Plasma Sources Science and Technology*, vol. 16, no. 3, p. 656, 2007.
- [142] G. Wormeester, S. Pancheshnyi, A. Luque, S. Nijdam, and U. Ebert, “Probing photo-ionization: simulations of positive streamers in varying N₂ : O₂ -mixtures,” *Journal of Physics D: Applied Physics*, vol. 43, no. 50, p. 505201, 2010.
- [143] Wikipedia, “Screened Poisson equation — wikipedia, the free encyclopedia,” 2016. [Online; accessed 4-March-2016].
- [144] Wikipedia, “Simpson’s rule — wikipedia, the free encyclopedia,” 2016. [Online; accessed 5-March-2016].

- [145] J. Teunissen, *3D Simulations and Analysis of Pulsed Discharges*. PhD thesis, Technische Universiteit Eindhoven, <http://repository.tue.nl/801516>, Nov 2015.

Acknowledgements

My deepest gratitude goes to my supervisor Ute Ebert. Thank you so much, Ute, for giving me this chance to learn and to do research in your group! It has been a long and wonderful journey and I feel like I have grown a lot both professionally and personally. Thanks a lot for being so generous with your resources.

I am very grateful to Sander Nijdam for actually putting me in contact with Ute Ebert when I was looking for a PhD position in the Netherlands. And I am also very happy to get to work with Sander. His advice, always practical and to the point, helped me a lot throughout these four years.

I really enjoyed the time I got to spend at ABB Corporate Research. I very much appreciate the time and expertise that Thomas Christen and Sergey Pancheshnyi shared there with me. For a month, Baden felt like home to me. Thanks again for your hospitality!

I very much appreciate Jannis Teunissen's help to get me off the ground with my PhD research and his help with other practical matters. Jannis is an extraordinary person, and almost every conversation gave me a new fresh perspective on old things.

A big part of my PhD research was done in close collaboration with Dirk Trienekens. It was a truly awesome experience to work with an experimentalist, besides Dirk being a very cool guy.

It has been a great pleasure to work with Casper Rutjes. I had such good luck to share an office with him. I am truly amazed at Casper's critical and down-to-earth approach to every problem on earth and outside the Earth.

I also acknowledge Willem Hundsdorfer, Guus Pemen, Anna Chvyreva, and many others colleagues for sharing their knowledge and ideas with me. Special thanks to our super-friendly and super-helpful secretary Nada Mitrovic.

Big thanks to my parents and grandparents for their unconditional support. I believe it is my father's biggest dream to see me as a Doctor of Philosophy.

I would never have been able to finish my thesis without my beloved boyfriend Willis. His care is my bare necessity and the ultimate luxury. And thanks for keeping champagne in our fridge ready for emergencies.

Curriculum Vitae

Anna Dubinova was born in Frunze, Kyrgyzstan on December 12, 1988. In 1992, her parents moved to Sarov, Russia, where she grew up. From 1996 to 2006 she attended Lyceum 15 and completed her secondary education with honors. In 2006 she was enrolled in the Nizhny Novgorod State University. There she received her Bachelor and Master degrees in physics. She carried out her graduation project on collimation of astrophysical jets in the Institute of Applied Physics in Nizhny Novgorod under supervision of professor V. V. Kocharovsky. In the summers of 2008-2011, she did four internships in the Eindhoven University of Technology, where she studied the theory of plasmas, including dusty and laser produced plasmas.

From 2012 to 2016 she was doing her PhD research on streamer discharge interaction with dielectrics in the Centrum Wiskunde & Informatica (CWI) supervised by professor U. Ebert. Her research was part of the STW project “Creeping Sparks” sponsored by ABB Corporate Research, where she spent a month doing an internship. In 2015-2016 she was member of the work council of the CWI and was involved in the transition of the Netherlands Organisation for Scientific Research (NWO).

Summary

A streamer is a type of electrical discharge that appears as an ionized channel in a gas or on a surface of an insulator. They grow very rapidly and can develop into other discharges. For example, they can be a precursor to lightning or to a surface flashover. In our studies of the physics of streamers in the vicinity of dielectrics, such as ice particles in thunderclouds or insulators in high voltage technology, we are inspired by the scientific curiosity to understand the origin of lightning and motivated to help high voltage technology to make better design rules.

In this thesis we study streamer discharge interaction with dielectrics using numerical models and simulations. A lot of effort was dedicated to developing an efficient solver for the electric field. In our time-dependent simulations, in which the electric field in a complex setup is updated every time step, it is crucial to calculate it accurately and fast. For handling this problem we chose the Ghost Fluid Method, which allowed us to incorporate dielectric and conductive bodies of arbitrary shape into the electric field solver.

Another numerical tool that was developed made it possible to include photoemission from a dielectric surface. Photoemission is particularly important for positive streamers because it provides additional free electrons. In some setups, for example with dielectric cylinders, shading effects can be encountered, when one side of a dielectric blocks photons from reaching its other side. We calculate the correction to the photon flux onto a dielectric cylinder due to the shading effect.

A large part of this research was dedicated to studying pulsed positive streamer interaction with a dielectric rod in air and in nitrogen in a cylindrical pin-to-plate geometry. That geometry was designed to compare simulations with the experiments carried out by D. Trienekens. For that purpose a 2D cylindrically symmetric fluid streamer model was developed.

As a result of that study, we learnt that in air, positive discharges do not propagate along a dielectric rod, but move away from it, as long as they have cylindrical symmetry. This unexpected observation was made both in simulations and experiments. The dielectric rod appeared to be a mere obstacle for the discharge and the properties of the dielectric did not play a role. In pure nitrogen, the role of free electrons produced by the dielectric surface becomes more significant and surface streamers are more likely than in air, which was confirmed in experiments and simulations.

When the repetition frequency of a discharge increases, the remaining ionization

increases too. This volume “leftover” ionization can be a source of free electrons competing with photoemission in pure nitrogen. As a consequence, surface discharges disappear at sufficiently high repetition frequency of pulses.

?Intrigued by the repulsion of a cylindrical discharge from a dielectric rod, we studied that effect further in a slightly modified setup. We found that in air there exists a competition of the attraction of a cylindrical discharge to a dielectric rod and its electrostatic self-repulsion. The outcome of that competition is determined by the threshold dielectric permittivity ϵ_{th} . For dielectric permittivities larger than ϵ_{th} , a surface discharge appears. We also observed that with photoemission included and for wider rods, a discharge has a surface component already at lower values of the dielectric permittivity.

The model that we developed for studying streamer interaction with dielectric rods also enabled us to describe lightning inception from ice particles in thunderclouds. We found that big and sharp enough ice particles are able to enhance the sub-breakdown electric field in thunderclouds locally such that it becomes larger than the breakdown field at that altitude. We estimated how big and sharp ice particles have to be to increase the electric field sufficiently. In that study we also addressed another problem. On average, in humid air of thunderclouds there are essentially no free electrons. However, free electrons can be temporarily produced by extensive air showers launched by highly energetic cosmic particles. Both these ingredients are necessary for lightning inception and they have to coincide in time and space.

Furthermore, we delved into the physics underlying positive streamer discharge inception from a dielectric body in a sub-breakdown background electric field, based on the simulations performed for the lightning inception problem. We discovered that the Meek criterion widely used in electrical engineering to predict and avoid discharges has to be revisited, as it gives only a rough estimation. We described the effects that have to be accounted for to construct a more accurate criterion. They include spatial distribution of initial electrons, convergence of the electric field lines and photoionization. We also demonstrated how important the dependence of the dielectric permittivity on frequency can be for streamer propagation.

A small study in the thesis is dedicated to streamer propagation in a short gap between a positive pin anode and a dielectric tip under a voltage pulse with a sub-nanosecond rise time. Interestingly, in air the streamer reaches the tip, whereas in nitrogen, it does not, creating an electron-free area avoided by a positive streamer. In air, due to the abundant photoionization that area is filled with electrons continuously.

Finally, we describe an alternative method to calculate the photoionization and photoemission integrals. The method is based on treating the absorption coefficient as a separate variable and reducing the task to solving a number of Helmholtz equations. Efficient solvers for Helmholtz equations are typically available in streamer discharge models and therefore can be used for photoionization and photoemission. The method proved to work for photoionization in air as well as other dedicated methods. In pure nitrogen, our method works much better than the other methods.